

THREE-DIMENSIONAL MICRO FABRICATION OF ACTIVE MICRO DEVICES
USING SOFT FUNCTIONAL MATERIALS

BY

HO WON LEE

DISSERTATION

Submitted in partial fulfillment of the requirements
for the degree of Doctor of Philosophy in Mechanical Science and Engineering
in Graduate College of the
University of Illinois at Urbana-Champaign, 2011

Urbana, Illinois

Doctoral Committee:

Assistant Professor Nicholas X. Fang, Director of Research
Professor John A. Rogers
Professor Narayana R. Aluru
Assistant Professor Rohit Bhargava

ABSTRACT

Active materials that can adapt to dynamic environment have attracted growing attention in various fields of science and engineering because they hold great potential in development of autonomous and multifunctional devices and systems. Hydrogels, which swell and contract in response to a wide range of external stimuli, have been studied extensively as one of the most promising functional materials. Unique properties and advantages of these materials, however, have not been fully explored and successfully implemented at device level primarily because manufacturing and material process of this new class of materials still rely on conventional fabrication methods.

This study presents development and application of a novel three-dimensional digital microfabrication technology, projection micro-stereolithography (PμSL), to engineer soft functional materials into reconfigurable active micro devices. Generation of complex motion is demonstrated by appropriate design of embedded microvascular network for direct solvent delivery in the polymeric device. Bio-inspired design principles of harnessing mechanical instability have been applied to improve actuation speed of soft devices and to create spontaneous structural pattern transformation. Fundamental mechanics on solvent diffusion kinetics and associated mechanical behavior of polymer is also investigated.

To my family

ACKNOWLEDGEMENTS

First and foremost, I would like to acknowledge my family and their support. Their unconditional love grew me up, gave me strength to strive to excel, and has been a warm shelter where I can always find rest.

I would also like to express my deep gratitude to my advisor, Professor Nicholas Fang. Undoubtedly, this thesis work would never be made possible without his advice and support. He has given me opportunities to explore many interesting interdisciplinary research projects, has always encouraged me to aim high, and has never lost confidence in me.

Also, I truly thank Dr. Chunguang Xia, a former graduate student in my research group, who contributed tremendously to my thesis work by developing the projection micro-stereolithography system. I am very grateful to my collaborators in Arizona State University, Professor Hanqing Jiang and Jiaping Zhang, for providing theoretical background and numerical simulation in mechanics study. I also wish to express my gratitude to my doctoral examination committee members, Professor Rogers, Professor Aluru, and Professor Rohit Bhargava, for their invaluable advice and comments. I would like to thank all members in my research group for their kind help, discussions, and inspirations. Finally, I gratefully acknowledge Korean Student Association in MechSE. I have never been alone in this lonely journey because of their friendship.

TABLE OF CONTENTS

| | |
|---|-----|
| CHAPTER 1: INTRODUCTION | 1 |
| CHAPTER 2: PROJECTION MICRO-STEREOLITHOGRAPHY FOR THREE- DIMENSIONAL MICROFABRICATION..... | 10 |
| CHAPTER 3: THREE-DIMENSIONAL SWELLING ACTUATION | 30 |
| CHAPTER 4: ACTUATION SPEED ENHANCEMENT BY SNAP-BUCKLING INSTABILITY | 62 |
| CHAPTER 5: PATTERN TRANSFORMATION USING SWELLING-INDUCED BUCKLING INSTABILITY | 84 |
| CHAPTER 6: NON-FICKIAN SOLVENT DIFFUSION COUPLED WITH LARGE DEFORMATION OF SWELLING GELS | 103 |
| CHAPTER 7: SUMMARY AND FUTURE WORK..... | 134 |
| APPENDICES | 142 |
| AUTHOR’S BIOGRAPHY | 154 |

1. INTRODUCTION

1.1 BACKGROUND AND MOTIVATION

Microfabrication refers to manufacturing of miniature structures and devices with dimensions spanning in the micro meter range or smaller. Microfabrication processes and technologies have been developed exclusively for mass production of electronic circuits (IC) and their high density integration through miniaturization. Focused topics of this field include optical lithography, material process for silicon and metals, and precision engineering. Miniaturization had gained speed as microfabrication engineering matured since 1960's, and the smallest possible manufacturing feature size has continuously decreased following Moore's law. Gordon Moore, an inventor of the IC, observed in 1965 that the surface area of a single transistor reduced by 50 percent every two year [1, 2]. There has been enormous advent in the field of IC industry thereafter, which has been continuously changing the world with innumerable electronic devices all around our daily lives. Now semiconductor chips with feature size of a few tens of nanometers are commercially available. Miniaturization is still an ongoing topic in the mainstream IC industry which scientists and engineers put more effort forth to.

There has been another direction of research and engineering which stems from the IC microfabrication, called microelectromechanical system (MEMS). Researchers have found that microfabrication technologies originally developed for ICs can fabricate not only electronic circuits in planar substrate, but also structural elements and devices with

moving parts in micro scale. MEMS technologies contributed to rapid propagation and wide dissemination of various sensors and actuators because miniaturization and mass production significantly reduced physical volume and weight and cost of the products. For instance, gyroscope used to be so bulky and expensive that they could only be used in limited fields such as aerospace engineering, but now MEMS based motion sensors are widely used in hand-held devices and in automobile airbags. Besides replacing existing devices, MEMS technologies have led to invention of new class of devices and applications as well, taking advantage of different physical properties in micro scale. For example, electrostatic force can be a dominant driving force for mechanical components against inertia in micro scale, as opposed to in macro scale where it is often negligible compared to gravity. This has been extensively exploited in the development of latest sensors and actuators such as digital micromirror devices (DMDTM, Texas Instrument).

Although microfabrication technologies have made substantial innovations in many fields, they have inherent limitations. Since the manufacturing processes have branched out from fabrication methods for electronic circuits, features being made are limited in two dimensional space. Efforts have made to extend the fabrication capability into three dimensional space, but intrinsically two dimensional manufacturing processes have only been able to realize limited three dimensional fabrication. In addition, materials being processed are mostly hard and brittle inorganic materials such as semiconductors and metals. Current MEMS approach still has its own implications and applications and holds great potential in various fields. However, extending choices of materials and geometries is also very important issue to address. To be more specific, three dimensional

microfabrication of soft materials will create new opportunities to develop and improve devices and applications with new functionalities that have not been explored and realized with existing technologies to date. For example, nature provides full of inspirations as to how advanced functionalities can be achieved through three dimensional arrangement of soft materials. To name a few, robust and reversible adhesion property of Gecko foot comes from highly three dimensional hierarchical arrangement of their soft fibrils on the skin [3, 4]. Octopus is able to freely change shape, color, and texture of its body to hide itself from predators [5]. Venus flytrap is able to catch and engulf flying insects by triggering snap-buckling instability of their specially designed leaves [6]. Construction and control of soft elastic matter in three dimensional space is indispensable to implement such novel functionalities.

The term soft active material describes materials that can change its properties depending on thermal, chemical, mechanical, or other environmental conditions and spontaneously produce meaningful output including, but not limited to, mechanical deformation, optical property change, or electrochemical response. Soft active materials have been attracting growing attention in various fields of science and engineering because of their potential for adaptive, autonomous, and multifunctional devices and systems. Hydrogels have been intensively studied for the last few decades in this context as one of the most promising soft active materials [7-13].

Hydrogels are a network of polymer chains that undergoes volumetric change upon solvent absorption. Since the first demonstration of reversible expansion and contraction of hydrogels [7], this unique phenomenon has been intensively studied

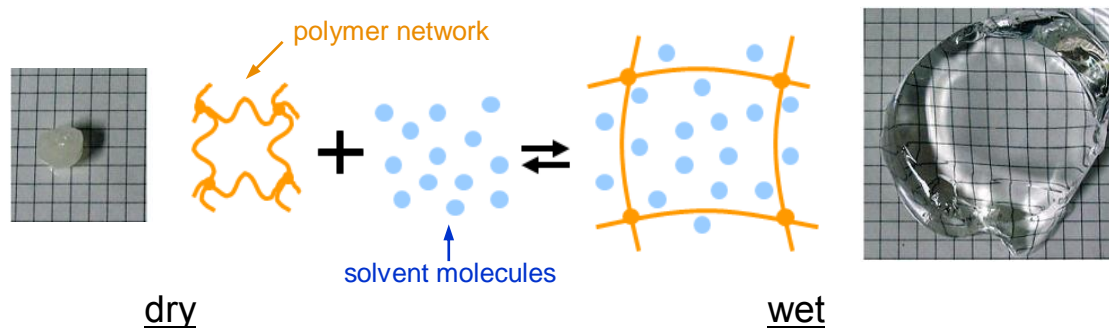


Figure 1.1 Schematic of hydrogel swelling. Photographs are from [14].

experimentally [7-13] and theoretically [15, 16]. In contrast to inorganic materials which can exhibit small deformation within a few percent, Hydrogels can accommodate large deformation and often swell up to more than ten times of its original volume. Also, hydrogel resembles biological matter such as cells and tissues in a sense that it provides not only structural integrity but also material pathway by allowing small molecules to diffuse through. More recently, many hydrogels have been found responsive to a variety of environmental stimuli such as temperature, pH, light, electric field and many others [7-13]. Along with the direct conversion of chemical energy to mechanical work, the responsive properties of hydrogels make it possible to integrate multiple functions including sensing and actuation in a single device, which leads to diverse applications in microfluidics [8], optics [9], and drug delivery [17]. Although many hydrogel micro devices have been reported [18-20], they are in simple geometry such as sphere and strip and fine control of motion and its time scale remain challenging. Furthermore, in many cases the device should be made of several different polymers or completely immersed in solvent for actuation [20, 21]. Therefore, there is high demand for three dimensional

microfabrication to integrate hydrogels into appropriate architectures in order to further extend and fully exploit the unique properties of hydrogels.

This study encompasses development of three dimensional microfabrication technology for soft materials, implementation of bio-inspired design principles in active micro devices, and characterization and quantification of dynamic behavior of soft active materials and devices.

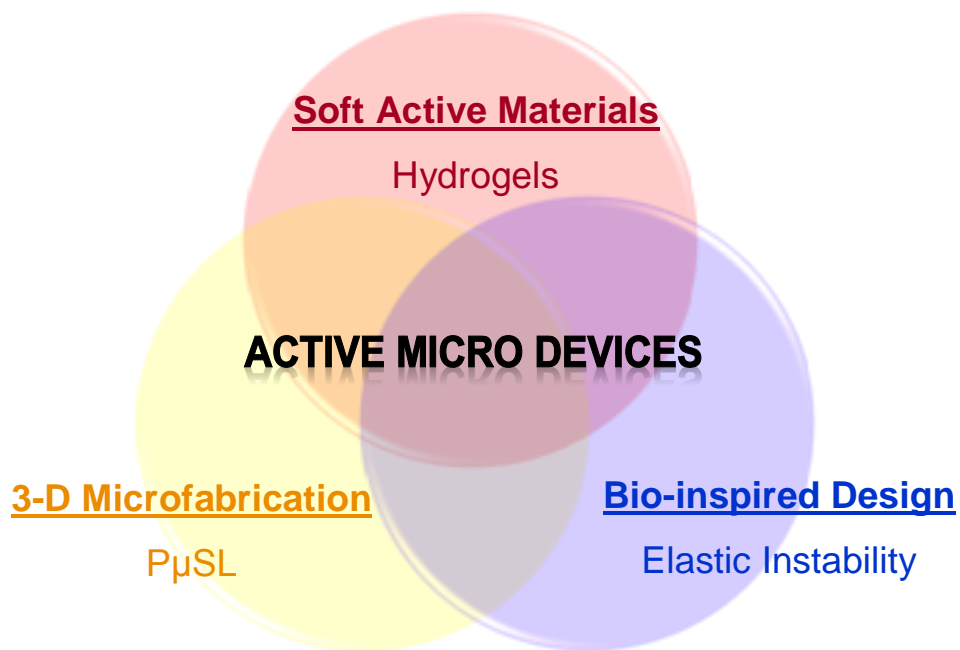


Figure 1.2 Research Schematic

1.2 DISSERTATION ORGANIZATION

The main theme of this thesis is implementation of bio-inspired design principles into active micro devices using three dimensional microfabrication technology and soft active materials. The dissertation consists of 7 chapters, each of which contains comprehensive research efforts on specialized topic.

Chapter 1 provides a background about micromanufacturing and soft materials and motivation for this study.

Chapter 2 introduces the three dimensional microfabrication system, projection micro-stereolithography (P μ SL), developed and used for the rest of the study. Characterization of optical system and photopolymerization process is presented. Next generation P μ SL developed for heterogeneous multi-material fabrication is also introduced.

Chapter 3 presents how to control hydrogel swelling using fabrication parameters and how to create three dimensional motion in hydrogel microgel structure. Novel approaches for local swelling control of hydrogel is implemented and this mechanism is demonstrated in several devices. Also, time scale limit of swelling actuation is identified and strategy to break this limit is discussed.

Chapter 4 is dedicated to demonstration of design principle to enhance actuation speed beyond the limit by incorporating elastic instability. Rapid movement of polymer device is demonstrated using snap-buckling. Fast actuation speed is used to make the device jump and energy released during the snap-buckling actuation is estimated from the jumping trajectory.

Chapter 5 presents a use of swelling-induced mechanical instability in different aspects. Well-controlled pattern transformation of tubular-shaped microgels is demonstrated using swelling-induced circumferential buckling. Mechanism behind the pattern formation is explained by simple energy analysis.

Chapter 6 focuses on development of mathematical model to capture dynamic behavior of swelling polymer associated with solvent migration to understand underlying actuation principle of the hydrogel devices presented in previous chapters. A rigorous mechanics model for coupled diffusion and large deformation of polymer and experimental techniques to quantify the non-Fickian diffusion of solvent in the swelling polymer are presented.

Finally, Chapter 7 summarizes the work presented in the dissertation and provides an outlook with potential applications for future study.

1.3 REFERENCES

1. Moore, G.E., *Interview*, in *Scientific American*. 1997.
2. Madou, M.J., *Fundamentals of Microfabrication; The science of miniaturization*. 2nd ed. 2002, New York: CRC Press.
3. Autumn, K., et al., *Adhesive force of a single gecko foot-hair*. *Nature*, 2000. **405**(6787): p. 681-685.
4. Tian, Y., et al., *Adhesion and friction in gecko toe attachment and detachment*. *Proceedings of the National Academy of Sciences*, 2006. **103**(51): p. 19320-19325.
5. Hanlon, R.T., J.W. Forsythe, and D.E. Joneschild, *Crypsis, conspicuousness, mimicry and polyphenism as antipredator defences of foraging octopuses on Indo-Pacific coral reefs, with a method of quantifying crypsis from video tapes*. *Biological Journal of the Linnean Society*, 1999. **66**(1): p. 1-22.

6. Forterre, Y., et al., *How the Venus flytrap snaps*. Nature, 2005. **433**(7024): p. 421-425.
7. Kuhn, W., et al., *Reversible Dilation and Contraction by Changing the State of Ionization of High-Polymer Acid Networks*. Nature, 1950. **165**: p. 514-516.
8. Beebe, D.J., et al., *Functional hydrogel structures for autonomous flow control inside microfluidic channels*. Nature, 2000. **404**(6778): p. 588-590.
9. Dong, L., et al., *Adaptive liquid microlenses activated by stimuli-responsive hydrogels*. Nature, 2006. **442**(7102): p. 551-554.
10. Sidorenko, A., et al., *Reversible Switching of Hydrogel-Actuated Nanostructures into Complex Micropatterns*. Science, 2007. **315**(5811): p. 487-490.
11. Lendlein, A., et al., *Light-induced shape-memory polymers*. Nature, 2005. **434**(7035): p. 879-882.
12. Tanaka, T., et al., *Collapse of Gels in an Electric Field*. Science, 1982. **218**: p. 467-469.
13. Miyata, T., N. Asami, and T. Urugami, *A reversibly antigen-responsive hydrogel*. Nature, 1999. **399**(6738): p. 766-769.
14. Ono, T., et al., *Lipophilic polyelectrolyte gels as super-absorbent polymers for nonpolar organic solvents*. Nat Mater, 2007. **6**(6): p. 429-433.
15. Tanaka, T. and D.J. Fillmore, *Kinetics of Swelling of Gels*. Journal of Chemical Physics, 1979. **70**(3): p. 1214-1218.

16. Hong, W., et al., *A theory of coupled diffusion and large deformation in polymeric gels*. Journal of the Mechanics and Physics of Solids, 2008. **56**(5): p. 1779-1793.
17. Cao, X., S. Lai, and L. James Lee, *Design of a Self-Regulated Drug Delivery Device*. Biomedical Microdevices, 2001. **3**(2): p. 109-118.
18. Gerlach, G., et al., *Chemical and pH sensors based on the swelling behavior of hydrogels*. Sensors and Actuators B: Chemical, 2005. **111-112**: p. 555-561.
19. Kim, D. and D.J. Beebe, *Hydrogel-based reconfigurable components for microfluidic devices*. Lab on a Chip, 2007. **7**(2): p. 193.
20. Guan, J., et al., *Self-Folding of Three-Dimensional Hydrogel Microstructures*. The Journal of Physical Chemistry B, 2005. **109**(49): p. 23134-23137.
21. Leong, T.G., et al., *Tetherless thermobiochemically actuated microgrippers*. Proceedings of the National Academy of Sciences, 2009.

2. PROJECTION MICRO-STEREOLITHOGRAPHY FOR THREE-DIMENSIONAL MICROFABRICATION

2.1 INTRODUCTION

Projection micro-stereolithography (P μ SL) offers unique opportunities to engineer and develop various functional materials systems into micro structures and micro devices in a wide variety of complex geometries and dimensions. Granted with the freedom of manufacturing three-dimensional architectures at micron scale, P μ SL makes it possible to explore and investigate many design principles and inspirations which would not be realized otherwise [1-4]. This chapter introduces brief overview of fabrication process of the current P μ SL systems.

2.2 PROJECTION MICRO-STEREOLITHOGRAPHY (P μ SL)

P μ SL is a digital freeform 3D microfabrication technique which is capable of making highly complex 3D micro structures in an additive, layer-by-layer fashion with micro scale resolution. P μ SL utilizes the most advanced digital micro display technology, a digital micromirror device (DMD) [5] or a liquid crystal on silicon (LCoS) chip [6], as a dynamic mask generator, which works as a virtual photomask with digitally and dynamically configured patterns.

2.2.1 PROCESS OVERVIEW

Figure 2.1 is a schematic of P μ SL. 3D CAD drawing is digitally sliced into a set of layers. The cross sectional image of each layer works as digital photomask to fabricate corresponding layers. When the first image (the image from the lowest layer) is sent to the dynamic mask generator, a flood of light from the UV source (mercury lamp G-line, 436nm) is reflected off the dynamic mask generator. Then the beam containing the image is optically routed and focused on the surface of the monomer resin, solidifying the illuminated area. The projection lens in the light path reduces the image to smaller size to achieve high resolution. Once the layer is polymerized, the substrate on which the sample rests drops by the thickness of the next layer under the monomer surface (Figure 2.1b).

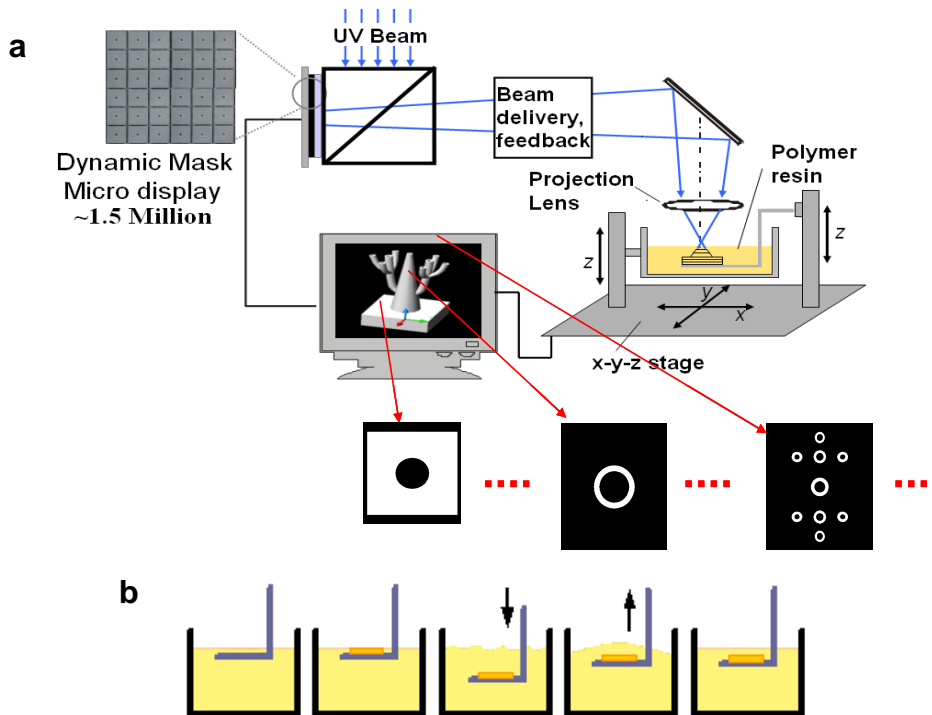


Figure 2.1 (a) Schematic of P μ SL system and fabrication process (b) sample substrate movement during fabrication [7].

Fresh monomer solution covers the polymerized layer, and the next image is in turn projected to polymerize the next layer on top of the preceding layer, without the need for additional alignment. This process proceeds iteratively until all the layers are complete.

2.2.1.1 Resolution

While offering 3D fabrication capability, P μ SL also allows high resolution microfabrication because it is a lithography technique. Ideally, in-plane resolution is limited by optical wavelength of the illuminating light, which is called a diffraction limit. However, practical resolution is determined by the pixel size of a digital dynamic mask generator and the optical system. In current system, physical size of each pixel is about 10 μ m by 10 μ m. This native resolution of the dynamic mask generator can be further improved by optical system. With 10 times projection lens in current system, resolution is reduced by 10 times down to 1 μ m. In practice, the transfer function of the optical system renders some degree of blurriness to the input image, resulting in degraded resolution at the fabrication plane. This effect is further quantified by optical characterization of the system in the next section. Vertical resolution, on the other hand, is determined by the resolution of the vertical translational stage because thickness of a layer is determined by the vertical displacement of the substrate where the sample is placed. The current system can faithfully practice in-plane resolution of 2 μ m and vertical resolution of 1 μ m.

2.2.1.2 Fabrication cost and speed

P μ SL is a parallel fabrication technology for highly complex 3D microstructures. Conventional microfabrication technologies rely on sacrificial layer approach to build up 3D features. Therefore, layers which will be eventually removed from the final structure

also have to be fabricated, which consumes much time and resources. Also, each layer with different patterns requires respective physical photomask. Not only is this responsible for the extremely high the fabrication cost, but it also requires time consuming mask alignment process for every single layer. However, the nature of parallel fabrication makes P μ SL fast with low cost. Dynamically configurable digital mask generator eliminates the need for expensive physical photomask. Computer generated digital images replaces physical masks, so hundreds of masks with varying patterns necessary for highly complex architectures can be generated with no cost. In addition, by virtue of layer-by-layer process, no additional alignment process from layer to layer is required. Furthermore, unlike existing rapid prototyping apparatus where a layer is polymerized by scanning a laser beam spot throughout the entire layer, P μ SL is a projection lithography which solidifies the whole layer at once with a single flash of light. This parallel nature of the process makes the fabrication orders of magnitude faster compared to serial processes such as conventional rapid prototype technology and direct writing. Fabrication speed of P μ SL depends on the curing thickness and corresponding exposure time of each layer, but in general P μ SL can fabricate more than hundred layers per hour, which corresponds to building up 1mm per hour.

2.2.1.3 Scalability

P μ SL can achieve large area fabrication while maintaining high resolution. A dynamic mask generator in current system consists of 1400 by 1080 pixels. Each pixel is 10 μ m by 10 μ m is size, covering 14 \times 10.8 mm² exposure area. After 10 times reduction lens, resolution is improved to 1 μ m, but the exposure area is also reduced to 100 times

smaller area of $1.4 \times 1.08 \text{ mm}^2$. However, larger fabrication area is covered by integrating stepper system. The sample substrate is controlled laterally in x-y plane, so that solidified sample is shifted to expose on the adjacent area next to it. In this manner, fabrication area is extended to larger area without compromising resolution.

2.2.2 OPTICAL SYSTEM CHARACTERIZATION

2.2.2.1 Gray scale digital mask for pixel level intensity control

P μ SL utilizes a digitally configurable dynamic mask generator to modulate light. In addition to be able to turn each pixel on and off independently to flexibly change light pattern, each single pixel can be independently controlled to adjust the level of light intensity by making use of gray scale of the digital image. Light intensity of illumination determines crosslinking density of the polymer, which is in turn translated to different material properties including elastic modulus, viscosity, permeability, and swelling ratio, in case of hydrogel. Therefore, such material properties can be anisotropically distributed in the structure. Gray scale of the digital mask has also been utilized to control etching rate of the polymer with respect to etchant to selectively remove sacrificial polymer to realize full 3D microstructure [6]. Figure 2.2 shows quantitative result of light intensity control using gray scale image. Light intensity was measured at the fabrication plane as the gray scale was varied from 0 to 255. Range of gray scale from 50 to 200 showed fairly linear response of light intensity. This implies that exposure dosage can be independently varied with micro scale resolution without controlling exposure time.

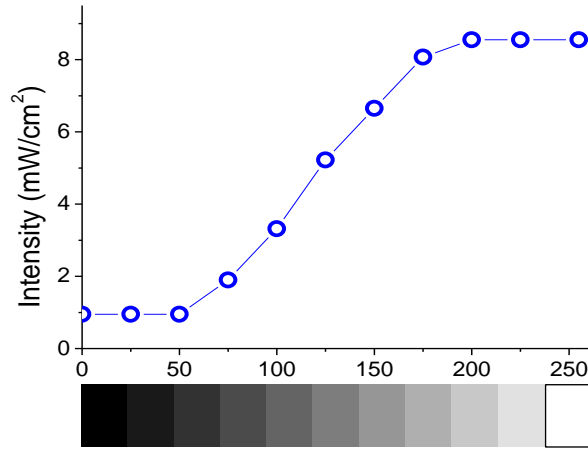


Figure 2.2 Gray scale of the mask image and light intensity at the fabrication plane. Color bar shows brightness of images corresponding to each gray scale level.

2.2.2.2 Point spread function identification

Native resolution of PuSL comes from 10 μm by 10 μm size pixel on the dynamic mask generator. After 10 time reduction lens, resolution should be 1 μm by 1 μm .

However, this simple algebra does not hold in real fabrication system because patterned light loses sharpness as it passes through the optical parts on the light path. Because of mutual interference, dark regions in the image never reach complete darkness and the white regions in the image never maintain the maximum brightness [8]. This is characterized by modulation transfer function (MTF) and point spread function (PSF) of the optical system. MTF is a transfer function of the optical system in frequency domain, thus

$$O[f_x, f_y] = M[f_x, f_y] \cdot I[f_x, f_y] \quad (2.1)$$

where $M[f_x, f_y]$ denotes MTF and $I[f_x, f_y]$ and $O[f_x, f_y]$ are two dimensional spatial Fourier transform of input and output image, respectively. PSF $p(x, y)$ is the counterpart of the modulation transfer function in spatial domain, therefore

$$M[f_x, f_y] = \mathbf{F}[p(x, y)] \quad (2.2)$$

where \mathbf{F} denotes two dimensional spatial Fourier transform.

In ideal system that delivers all optical information from input to output, $M[f_x, f_y] = 1$ at all frequency and $p(x, y) = \delta(x, y)$ where δ denotes Dirac delta function, which means that an image with any pattern should be transferred to the identical image

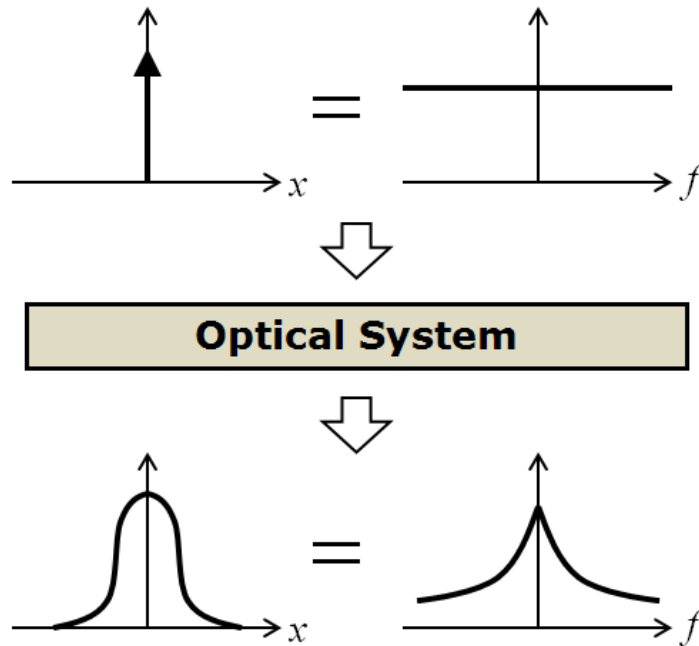


Figure 2.3 Schematic of point spread function and modulation transfer function. Spatial impulse function (a point of intensity) (top left) delivers uniform energy spanning all frequency range (top right). As the light passes the optical system, high frequency energy is depressed (low right) resulting in blurry Gaussian profile of spatial light intensity distribution (low left). The response of the optical system to impulse function is called point spread function.

with the same pattern and the same brightness. In physical optical system, however, $M[f_x, f_y] < 1$ and decreases with spatial frequency. This corresponds to $p(x, y)$ of Gaussian profile, instead of impulse function, as illustrated in Figure 2.3. Therefore, not only does intensity decrease as light passes through each optical component, but the sharpness of the input image degrades resulting in blurry images.

MTF and PSF characterize the optical system. Therefore, once $M[f]$ and $p(x, y)$ is known for the optical system, output image can be estimated for given input image,

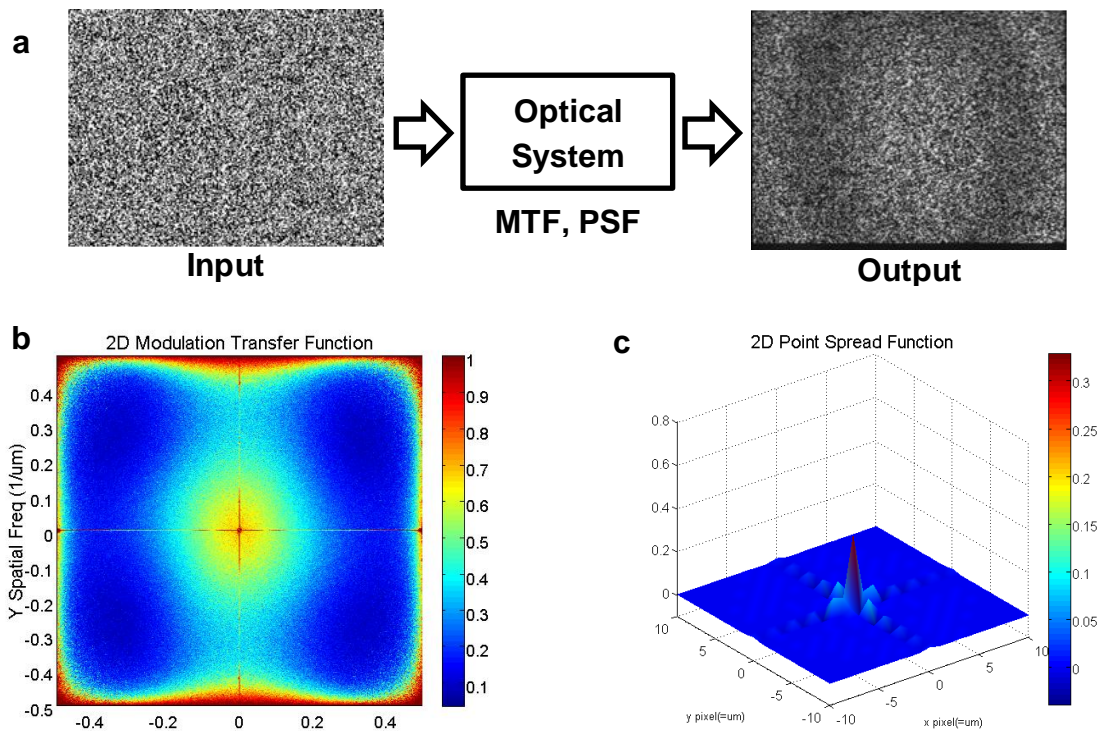


Figure 2.4 Experimental method to identify point spread function of the P μ SL. (a) 2D random noise image input was projected through the P μ SL and image output was captured by a CCD camera at the projection plane. (b) The ratio of 2D Fourier transform of the output to the input gives modulation transfer function. (c) Point spread function is obtained by taking 2D inverse Fourier transform of the modulation transfer function. Side lobes spanning many pixels are responsible for the blurred output image.

which is mathematically expressed as (1.1) in frequency domain or

$$o(x, y) = p(x, y) * i(x, y) \quad (2.3)$$

in spatial domain, where * denotes two dimensional convolution.

To obtain MTF of the P μ SL system, input image was projected through the P μ SL and output image was captured by CCD camera. To excite all frequency range, 2D random noise image was used as an input as shown in Figure 2.4a. 2D Fourier transform was conducted with the input image and the output image, which gives MTF by (2.1). This was repeated 20 times with different random noise images, and collected MFTs were averaged to avoid possible bias. PSF was obtained by doing inverse 2D Fourier transform on the MTF. The MTF and the PSF of P μ SL obtained in this way are presented in Figure 2.4b and Figure 2.4c, respectively. Frequency response of MTF decreases with frequency and PSF has side lobes spanning more than 10 pixels, which is responsible for rendering blurriness to the output image.

An input image of 2D periodic squares (Figure 2.5a) was tested to validate the PSF obtained above. An estimated output signal was constructed by doing 2D convolution operation on the input image and PSF. On the other side, the input image was projected through P μ SL to obtain real output image. Estimated and measured intensity profile along x and y direction on the output image were plotted in Figure 2.5c. Comparison shows good agreement in both x and y directions, validating the PSF of the P μ SL system. This proves that the projected output intensity can be faithfully estimated and simulated by obtaining PSF.

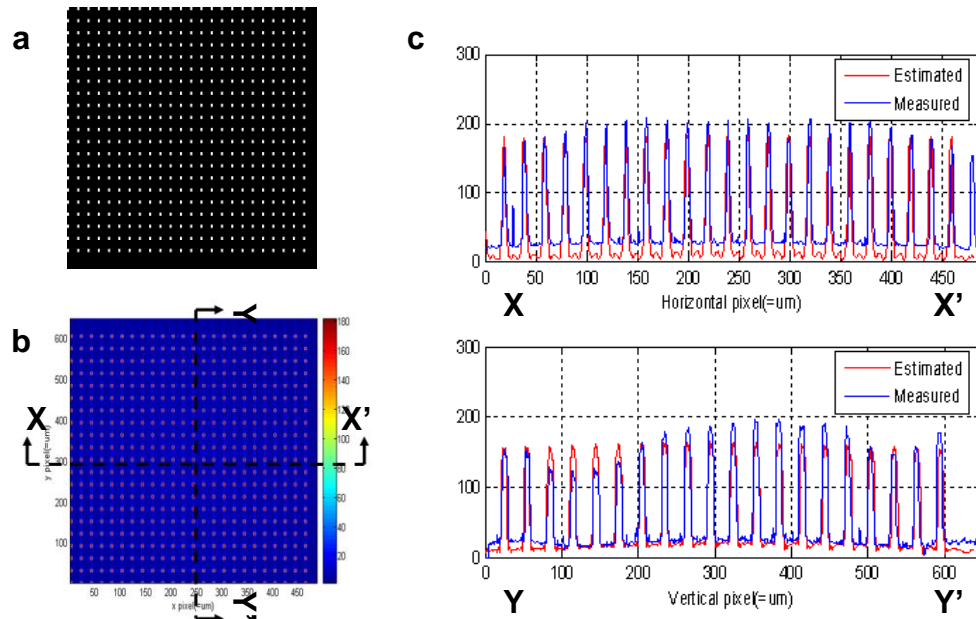


Figure 2.5 Validation of point spread function. Periodic square array image (a) was projected through P μ SL and measured output intensity distribution (b) is compared with the prediction (c) obtained by convolution of point spread function and input image.

PSF can be used as a useful mean to set an exposure strategy to improve features in fabrication. As PSF provides information as to how much light intensity “leaks out” from a given point, exposure sequence can be planned to prevent unwanted polymerization at locations susceptible to leaked light form adjacent area. Figure 2.6a shows a bridge structure as an example. By dividing the cross sectional image into two images for base part and bridge part, crosstalk on the connecting area is reduced as simulated using PSF in Figure 2.6b and Figure 2.6c, resulting in a fabricated structure with finer feature on the corner.

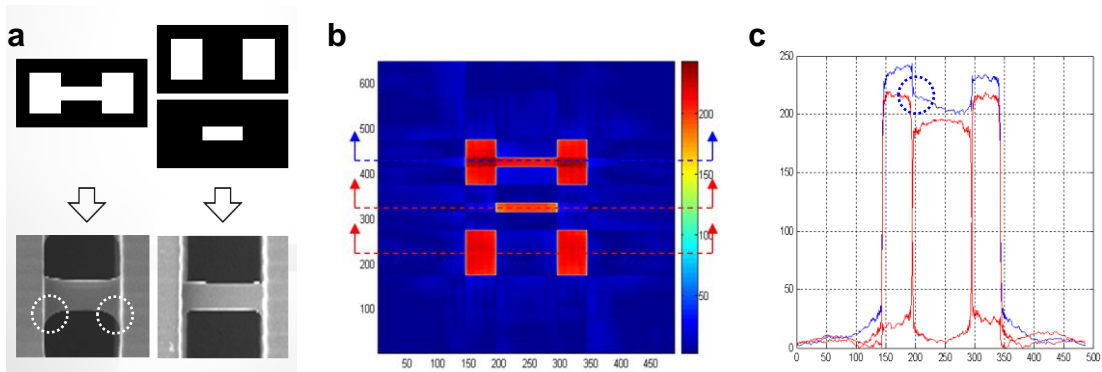


Figure 2.6 Prediction of light intensity distribution using point spread function. (a) Comparison of fabrication results between one exposure and separate two exposures (b) Intensity prediction obtained from point spread function. (c) Intensity profile comparison. Intensity leakage is more significant for the single exposure case (blue), which is responsible for unwanted crosslinking on the connecting part in (a).

2.2.3 POLYMERIZATION DEPTH STUDY

Lithography utilizes photochemical effect to convert liquid monomer into solid polymer. Therefore, polymerization process involves chemical factors such as concentration of photoinitiator and photoabsorber, diffusivity of photoinitiator, and quantum yield. In contrast to the in-plane resolution which depends on optical characteristics of the system, vertical resolution, especially for overhung structures without supporting layer below, is determined by light penetration depth to the monomer solution and sensitivity of photochemical reaction. Much effort has been put to develop theoretical model for photopolymerization process [6, 9, 10]. Here experimental study to correlate fabrication process conditions with photocuring depth is presented. The result of this study provides empirical working curves to be used to determine appropriate light intensity and exposure time in P μ SL process for desired structure.

Poly(ethylene glycol) diacrylate (PEGDA) of two molecular weight (PEGDA250 and PEGDA575) was used. A series of overhang bridges were fabricated as shown in Figure 2.7a. Exposure time was gradually increased from bottom to top. As bridge specimens are not supported by underlying structure, apparent thickness of each bridge is a direct result of varying exposure time. The experiment was repeated with different light intensities as well. Thickness of each bridge from different samples was measured by taking scanning electron microscope (SEM) image and the result for PEGDA250 and PEGDA 575 is plotted in Figure 2.7b and Figure 2.7c, respectively. Note that the horizontal axis is logarithmic scale of exposure and exposure is obtained by multiplying light intensity and exposure time ($E = I \times t$). The result is fitted to gain the following empirical working curve equations for respective material.

$$d_c = (27.6 \pm 1.1) \ln\left(\frac{E}{2.43 \pm 0.23}\right) \quad \text{for PEGDA250} \quad (2.4)$$

$$d_c = (19.4 \pm 0.71) \ln\left(\frac{E}{2.94 \pm 0.21}\right) \quad \text{for PEGDA575} \quad (2.5)$$

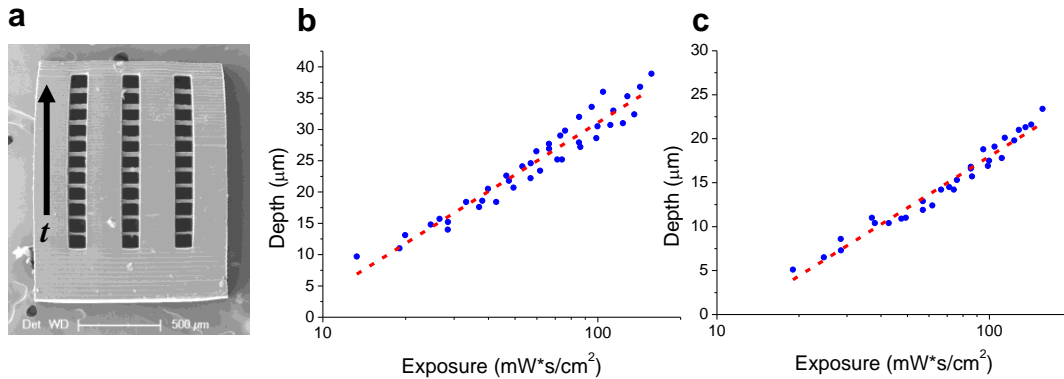


Figure 2.7 (a) SEM image of the sample for curing depth study. Experimental data from (b) PEGDA250 and (c) PEGDA575 and fitted working curves

2.2.4 THREE-DIMENSIONAL MICROSTRUCTURES

Figure 2.8 presents highly 3D microstructures fabricated by P μ SL. Figure 2.8a shows tree-like overhanging branches with interconnected channels. Figure 2.8b shows densely packed and vertically aligned microfluidic channels. Figure 2.8c shows highly curved polymeric shell structure with embedded open-surface microfluidic channel. Figure 2.8d demonstrates capability of fabrication for spherical shell with complex circular pores on the surface.

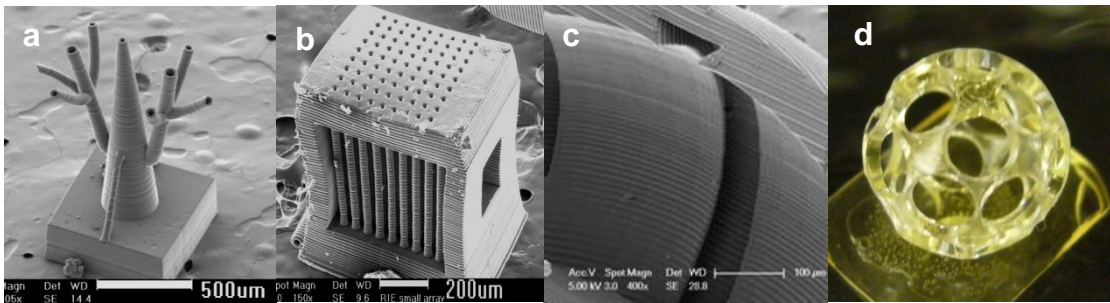


Figure 2.8 (a) microvascular tree [4] (b) densely packed capillary array [4] (c) highly curved shell with embedded channels (d) sphere with patterned pores on the surface

2.3 MEMBRANE-PUMP PROJECTION MICRO-STEREOLITHOGRAPHY (MP-P μ SL)

Material systems which exhibit novel functional properties have been proposed by designing microstructural unit cells [11-17]. The building blocks in these systems are in general highly 3D and often require heterogeneous integration of multiple materials in a controlled manner. In consequence, such material systems have remained at design stage and have not been realized in practice. P μ SL offers a unique opportunity to rapidly

fabricate highly complex 3D micro structures and therefore made it possible to explore many previously unachievable functional microstructures [1-4]. Although material properties can be anisotropically distributed within the structure, only one material can be fabricated for each fabrication cycle because switching material from one to another is not feasible owing to the free surface of the monomer resin. To address this issue, membrane-pump system has been integrated with P μ SL. Membrane-pump P μ SL (MP-P μ SL) has a fabrication chamber enclosed by transparent elastic membrane on the top, which allows for quick material switch during fabrication process by eliminating the free surface in P μ SL.

2.3.1 PROCESS OVERVIEW

Figure 2.9 is a schematic of MP-P μ SL. This system has been invented by the former graduate student, Dr. Chunguang Xia. Basic operation is the same as that of P μ SL. 3D CAD drawing is digitally sliced into a set of layers and sent to the dynamic mask generator. UV light emitting diode (LED, 405nm) and 1.2 times reduction projection lens are used in this system. The optical resolution at the fabrication plane is 8.5 μ m. The beam containing the image is now projected through the transparent polydimethylsiloxane (PDMS) membrane and focused on the sample substrate which sits on the syringe plunger. PDMS offers not only transparent deformable enclosure through which light can be transmitted, but it also prevents stiction of the polymerized layer by creating a virtual polymerization inhibition layer on the surface by allowing oxygen to permeate through [10, 18, 19]. Once the layer is polymerized, the syringe plunger where the substrate rests

drops, deforming elastic membrane downwards which develops negative pressure inside the sealed fabrication chamber. Then one of the inlet valves attached to respective material opens to supply fresh monomer solution into the fabrication chamber. Number of valves attached to the inlet of the chamber is not limited, therefore it is possible to fabricate a microstructure integrated with as many different material as necessary. Which valve to open is determined by what material to use for the next layer. To promote material switch, diaphragm pump is connected to the chamber, flushing out the existing material and filling the chamber with the new material to cover the previously polymerized layer. When material switch is complete, the next image is in turn projected to polymerize the next layer on top of the preceding layer. This process proceeds iteratively until all the layers are complete.

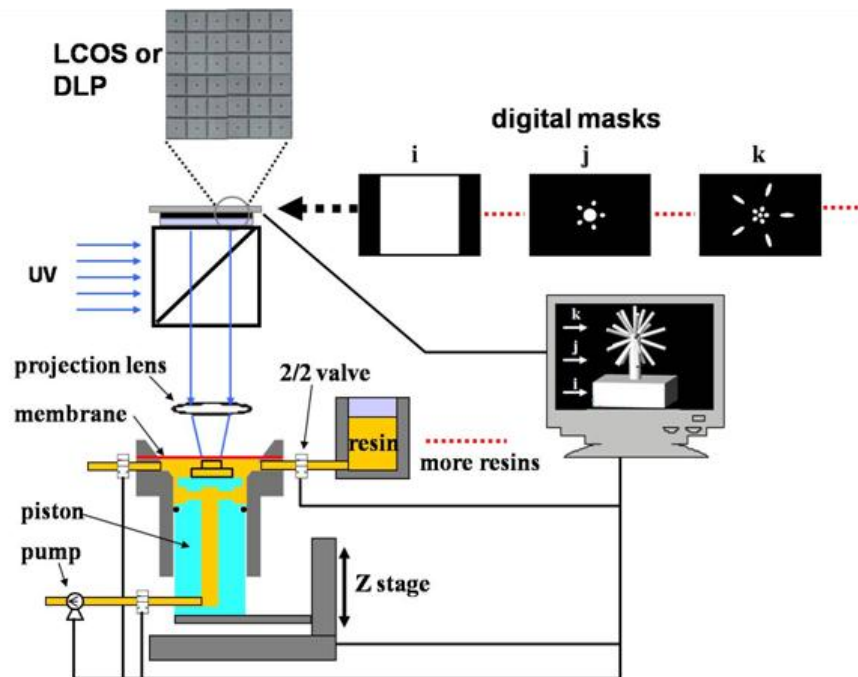


Figure 2.9 Schematic of membrane-pump PμSL (Credit: Chunguang Xia)

2.3.2 MULTI-MATERIAL 3D MICROSTRUCTURES

Figure 2.10 presents some examples of highly 3D microstructures with multi-material integration fabricated by MP-P μ SL. Figure 2.10a shows microstructures made of two materials heterogeneously integrated. Left is Taiji symbols and coaxial cylinders. Red part is PEG258 with rhodamine B dye and blue part is PEG258 with DiOC₂(3) dye. Right is structural demonstration of low thermal expansion material proposed by Steeves [13]. Honeycomb base is made of hexanediol diacrylate (HDDA) and pyramid struts are PEG258 with rhodamine B dye. Figure 2.10b shows a highly curved helix structure with a base material of HDDA. Two helices contain alumina particles and Si particles,

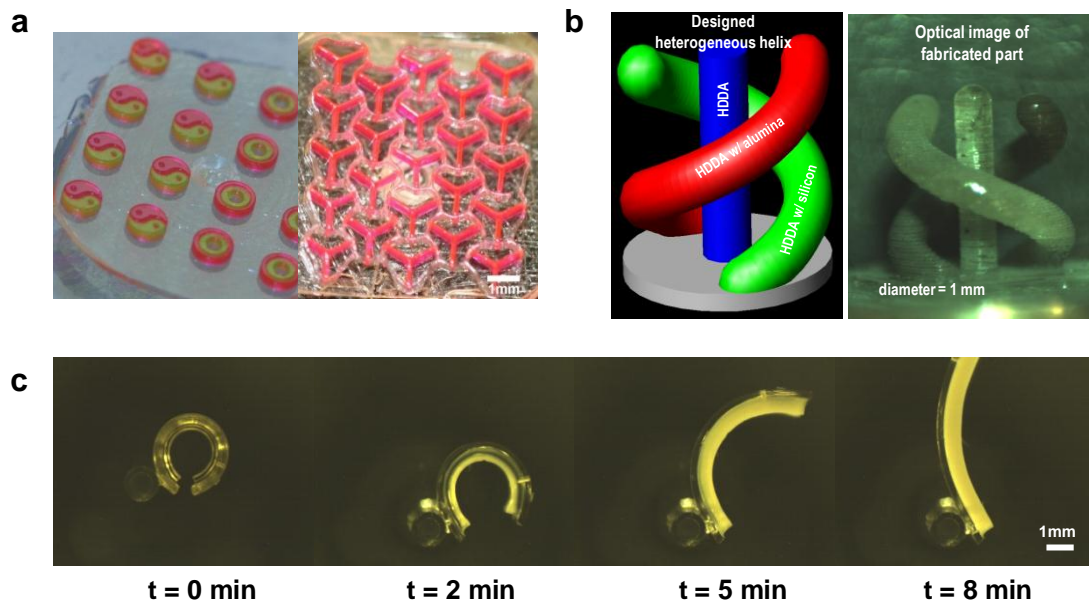


Figure 2.10 (a) Microstructures made of two materials (credit: Chunguang Xia) (b) Highly curved helix with embedded inorganic particles (credit: Chunguang Xia) (c) Integration of two hydrogels with different swelling ratio for large bending actuation.

respectively. This demonstrates that inorganic particles suspended in monomer solution have been successfully solidified into 3D architecture. Figure 2.10c shows integration of two hydrogels with different swelling ratio. When immersed in water, high contrast of swelling ratio between two materials gives rise to substantial bimorph effect, resulting in high degree of bending actuation.

2.4 SUMMARY

P μ SL has been developed for rapid, low cost, and scalable manufacturing of complex 3D microstructures. Optical characterization was carried out to quantify light intensity modulation with gray scale digital mask and to identify point spread function of the optical system. Polymerization depth depending on the light illumination intensity and exposure time has been studied and empirical working curve was obtained for PEGDA250 and PEGDA575. Membrane-pump system has been integrated to P μ SL to facilitate easy and fast material switch during fabrication. MP-P μ SL allows for heterogeneous three-dimensional integration of multiple materials as well as encapsulation of foreign particles in the structures. Demonstration of the fabrication capabilities of P μ SL and MP-P μ SL has been presented. This novel 3D microfabrication technology has made it possible to implement various design principles and inspirations and provided essential manufacturing solution to engineer soft functional materials into active micro devices in later chapters.

2.5 REFERENCES

1. Lee, H., C. Xia, and N. Fang. *Biomimetic Microactuator Powered by Polymer Swelling*. in *ASME International Mechanical Engineering Congress and Exposition*. 2008. Boston.
2. Lee, H., C. Xia, and N.X. Fang, *First jump of microgel; actuation speed enhancement by elastic instability*. *Soft Matter*, 2010. **6**(18): p. 4342.
3. Xia, C., H. Lee, and N. Fang, *Solvent-driven polymeric micro beam device*. *Journal of Micromechanics and Microengineering*, 2010. **20**(8): p. 085030.
4. Xia, C. and N.X. Fang, *3D microfabricated bioreactor with capillaries*. *Biomedical Microdevices*, 2009. **11**(6): p. 1309-1315.
5. Sun, C., et al., *Projection micro-stereolithography using digital micro-mirror dynamic mask*. *Sensors and Actuators A: Physical*, 2005. **121**(1): p. 113-120.
6. Xia, C. and N. Fang, *Fully three-dimensional microfabrication with a grayscale polymeric self-sacrificial structure*. *Journal of Micromechanics and Microengineering*, 2009. **19**(11): p. 115029.
7. Xia, C., *Three-Dimensional Polymeric Capillary Network: Fabrication and Applications*, in *Mechanical Science and Engineering*. 2009, University of Illinois at Urbana-Champaign: Urbana. p. 117.
8. Madou, M.J., *Fundamentals of Microfabrication; The science of miniaturization*. 2nd ed. 2002, New York: CRC Press.
9. Fang, N., *Engineering Subwavelength Photonic Meta Structures and Devices*. 2004, Univeristy of California at Los Angeles: Los Angeles.

10. Dendukuri, D., et al., *Modeling of Oxygen-Inhibited Free Radical Photopolymerization in a PDMS Microfluidic Device*. *Macromolecules*, 2008. **41**(22): p. 8547-8556.
11. Zhou, S., W. Li, and Q. Li, *Design of 3-D Periodic Metamaterials for Electromagnetic Properties*, in *IEEE TRANSACTIONS ON MICROWAVE THEORY AND TECHNIQUES*. 2010. p. 910-916.
12. Maldovan, M. and E.L. Thomas, *Diamond-structured photonic crystals*. *Nat Mater*, 2004. **3**(9): p. 593-600.
13. Steeves, C.A., et al., *Concepts for structurally robust materials that combine low thermal expansion with high stiffness*. *Journal of the Mechanics and Physics of Solids*, 2007. **55**(9): p. 1803-1822.
14. Torquato, S., S. Hyun, and A. Donev, *Multifunctional Composites: Optimizing Microstructures for Simultaneous Transport of Heat and Electricity*. *Physical Review Letters*, 2002. **89**(26).
15. Sigmund, O. and S. Torquato, *Design of smart composite materials using topology optimization*. *Journal of Smart Materials and Structures*, 1999. **8**: p. 365–379.
16. Erentok, A. and O. Sigmund, *Topology Optimization of Sub-Wavelength Antennas*, in *IEEE TRANSACTIONS ON ANTENNAS AND PROPAGATION*. 2011. p. 58-69.
17. Andreasen, C.S., A.R. Gersborg, and O. Sigmund, *Topology optimization of microfluidic mixers*. *International Journal for Numerical Methods in Fluids*, 2009. **61**(5): p. 498-513.

18. Dendukuri, D., et al., *Continuous-flow lithography for high-throughput microparticle synthesis*. Nature Materials, 2006. **5**(5): p. 365-369.
19. Dendukuri, D., et al., *Stop-flow lithography in a microfluidic device*. Lab on a Chip, 2007. **7**(7): p. 818.

3. THREE-DIMENSIONAL SWELLING ACTUATION

3.1 INTRODUCTION

Recent advances in micro fabrication techniques have made it possible to design and fabricate a wide variety of micro-devices such as IC circuits and Micro-electro-mechanical system (MEMS)-based sensors and actuators [1]. However, it is still not easy to make actively moving devices in micro scale as in macro scale because different physics such as viscosity and friction dominates in micro scale and below. There have been many studies to seek for novel design of microactuators, especially inspired by plant motion where the movement is created without any mechanical components or muscle. One of well-known moving plants is *Mimosa pudica*, also known as Sensitive plant, which folds its leaves in response to external disturbances such as mechanical and thermal stimulus. Once stimulated by touch or heat, *Mimosa pudica* regulates turgor pressure of motor cells located in pulvinus (a root of the leaf connected to the main branch). Owing to the fact that swelling motor cells are distributed mainly on one side of midrib, each leaf undergoes bending motion in the direction towards where less swelling occurs as shown in Figure 3.1[2].

Inspired by this elegant mechanism for producing movement, this chapter presents novel microactuators powered by hydrogel swelling. Hydrogels are a network of polymer chains that undergoes volumetric change upon solvent absorption. Since the first

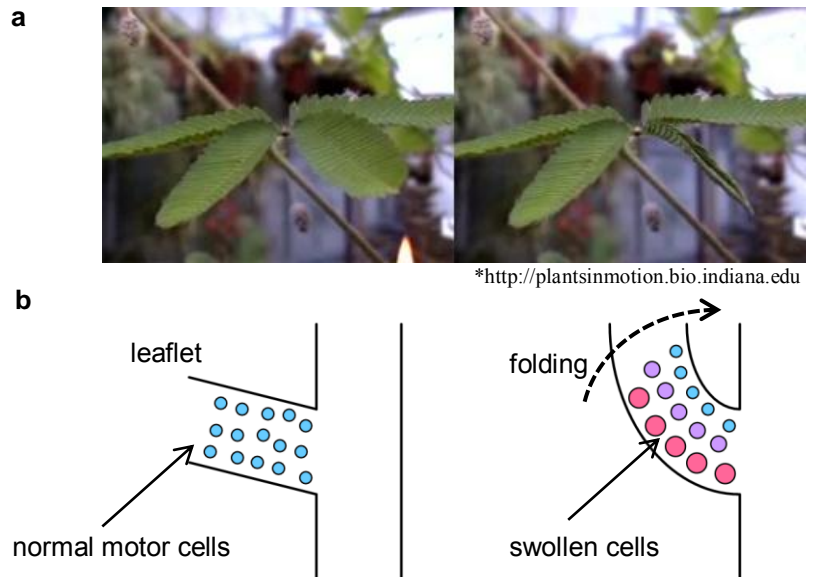


Figure 3.1 *Mimosa pudica* and its moving mechanism. (a) Motor cells at pulvinus are in normal state in open leaves (b) Selective increase of turgor pressure in motor cells results in folding motion of leaves.

demonstration of reversible expansion and contraction of hydrogels [3], this unique phenomenon has been intensively studied experimentally [3-9] and theoretically [10, 11]. More recently, many hydrogels have been found responsive to a variety of environmental stimuli such as temperature, pH, light, electric field and many others [3-9]. Along with the direct conversion of chemical energy to mechanical work, the responsive properties of hydrogels allows for integration of multiple functions including sensing and actuation in a single device, which leads to diverse applications in microfluidics [4], optics [5], and drug delivery [12].

Although many polymeric micro devices driven by swelling have been reported [13-15], these actuators are in simple geometry such as sphere and strip and fine control of motion and its time scale remain challenging. Furthermore, in many cases the device

should be made of several different polymers or completely immersed in solvent for actuation. In this chapter, polymeric micro device fabricated using 3D parallel micro fabrication technique, projection micro-stereolithography (P μ SL) [16] , is presented. By virtue of complex 3D fabrication capability, microfluidic channels are embedded in the device for direct solvent delivery. When solvent is delivered to the destination, it creates swelling gradient as it diffuses into polymer network from one side to the other, thereby producing net motion as shown in Figure 3.2. Therefore, complex motion requires only a single droplet of solvent and the movement can be designed by appropriate selection of the distribution and dimension of the embedded microfluidic network.

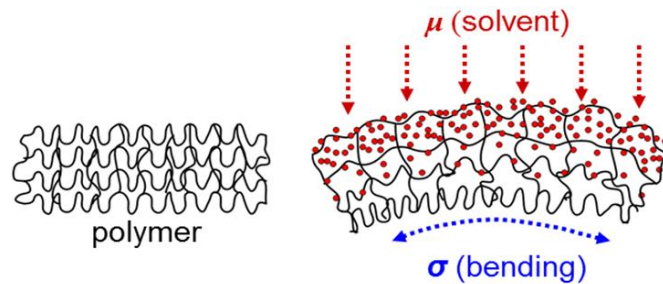


Figure 3.2 Schematic of polymer network in dry state (left) and in swollen state (right). Swelling gradient created by direct solvent delivery to one side of the polymer generates bending motion of the polymer

It has been reported that time scale of plant movement is limited by characteristic poroelastic time which is proportional to the square of the smallest dimension of moving part [17]. In this chapter, swelling mechanism of polymer is investigated based on Tanaka's theory [10] and is experimentally demonstrated that there exists a time scale of the device which is equivalent to the poroelastic time. Also, swelling-driven 3D microdevices including artificial micro *Mimosa pudica*, soft robotic gripper, self-foldable

active antenna and stent are presented for demonstration of this novel actuation mechanism.

3.2 THEORY

3.2.1 EQUILIBRIUM SWELLING AND ENERGY CONVERSION

First, equilibrium swelling of polymer in solvent is investigated to understand basic swelling behavior. The result of this analysis can be used to tailor volumetric swelling behavior of polymer and to maximize mechanical energy generation. Hydrogel is an elastomer, so it exhibits elastic behavior. On the other hand, solvent molecules stay and migrate in and out of hydrogel network, so hydrogel also has liquid nature. Therefore, swelling of hydrogel is described by Flory-Huggins mixing theory with additional consideration of elastic contribution [11, 18]. For isotropic swelling, the length-wise stretching ratio λ of hydrogel in solvent under mechanical stress s at equilibrium state can be obtained using the equation below derived as [11]

$$\frac{sv}{kT} = Nv \left(\lambda - \frac{1}{\lambda} \right) + \lambda^2 \log \left(1 - \frac{1}{\lambda^3} \right) + \frac{1}{\lambda} + \frac{\chi}{\lambda^4} \quad (3.1)$$

where N is crosslinking density, v is molecular volume of solvent, and χ is Flory-Huggins interaction parameter, respectively. In case of free swelling (i.e. no mechanical stress), equation (3.1) is reduced to

$$Nv \left(\lambda_{eq} - \frac{1}{\lambda_{eq}} \right) + \lambda_{eq}^2 \log \left(1 - \frac{1}{\lambda_{eq}^3} \right) + \frac{1}{\lambda_{eq}} + \frac{\chi}{\lambda_{eq}^4} = 0 \quad (3.2)$$

where λ_{eq} is equilibrium swelling ratio. Here, the first term represents entropic increase due to elastic stretching of the polymer network, the second and third terms represent entropic contribution due to mixing of polymer and solvent molecules, and the last term represents enthalpic penalty against mixing the two molecules, respectively. χ depends on the combination of polymer-solvent pair. With other conditions being equal, the lower the χ , the more solvent can diffuse into and mix with polymer network against elastic stretching of polymer network, and thus the polymer swells larger in the solvent. Once polymer-solvent is given (or given χ), swelling ratio depends on crosslinking density. As can be expected, the lower the crosslinking density, the larger the swelling ratio because entropic penalty due to elastic stretching of the network is less. Crosslinking density is closely related to the elastic modulus of the polymer with the following equation [19],

$$E = 3NkT$$

(3.3)

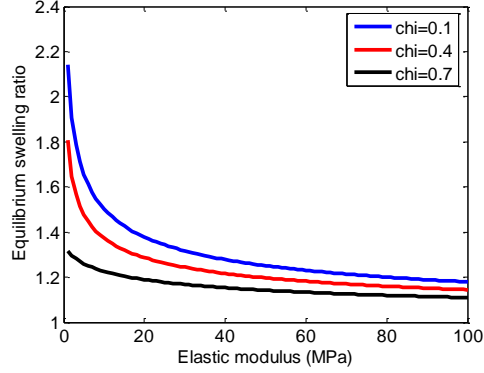


Figure 3.3 Equilibrium swelling ratio against elastic modulus of polymer for different Flory interaction parameters.

where k and T are Boltzmann constant and absolute temperature, respectively. Figure 3.3 presents the relationship between equilibrium swelling ratio and Young's modulus for different Flory interaction parameters.

Under quasi-static assumption, equation (3.1) gives the change in mechanical stress or swelling pressure as polymer network swells in solvent. Here we define swelling pressure as the maximum external stress that the polymer network can sustain at given swelling ratio. Transient response is not taken into consideration in this analysis. Since swelling ratio is equivalent to strain and swelling pressure corresponds to stress, we can estimate maximum energy we can obtain from the swelling process by integrating stress-strain curve. Figure 3.4 shows swelling pressure change for different Flory interaction parameters and corresponding energy density. From this result, we can conclude that polymer-solvent combination having lower Flory interaction parameter yields higher energy transduction as well as higher equilibrium swelling ratio. This result provides useful information about the selection of polymer network and swelling solvent.

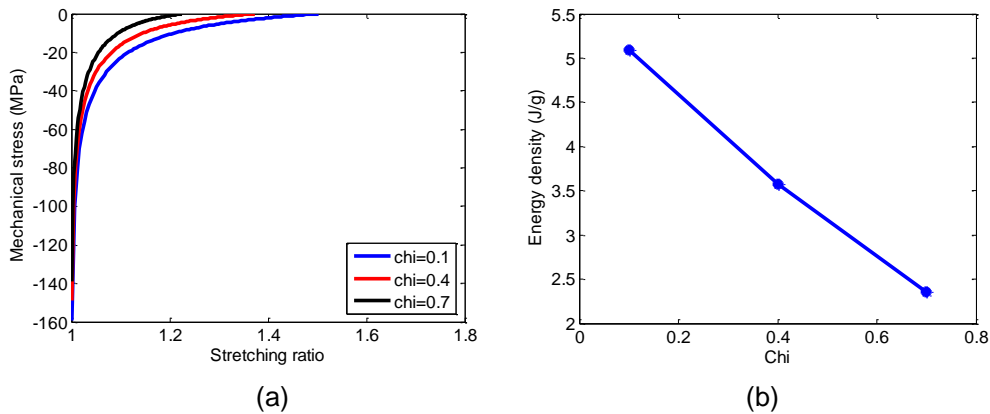


Figure 3.4 (a) Swelling stress change for different Flory interaction parameter and (b) corresponding energy density produced in swelling process.

For given polymer-solvent combination, we can further engineer swelling behavior and energy conversion by controlling fabrication process condition. As introduced in chapter 2, our digital freeform micro fabrication system, P μ SL, allows for controlling the crosslinking density of polymer at single pixel level. Given illumination time and chemistry, bright area in the digital dynamic mask delivers higher intensity of light, thus polymer is more densely crosslinked. In contrast, gray area transfers lower light intensity, thus polymer is less crosslinked. As shown in equation (3.3), crosslinking density determines the modulus of resulting structure. Figure 3.5 shows swelling pressure change for different crosslinking densities, thus elastic moduli, and corresponding energy density. The result suggests that more energy conversion as well as larger swelling ratio is expected for less crosslinked polymer for a given Flory interaction parameter.

Considering that low crosslinked polymer is not favorable for structural stability and reliability in general, this analysis is expected to be used to find an optimal process condition to meet the structural requirement and the need for maximum energy

conversion simultaneously.

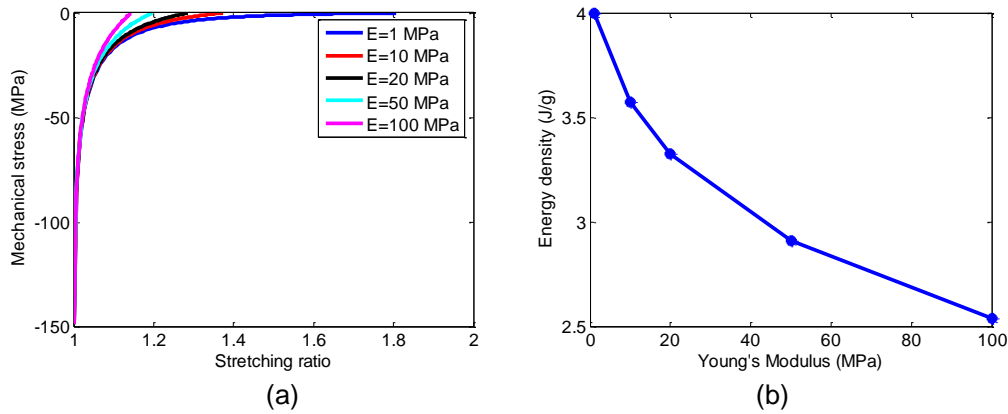


Figure 3.5 (a) Swelling stress change for different crosslinking densities and (b) corresponding energy density produced in swelling process.

3.2.2 KINETICS OF SWELLING-DRIVEN ACTUATION

Time scale of the motion is inherently tied to the kinetics of solvent diffusion because the actuation of the present device is driven by local swelling of polymer as a result of solvent penetration into polymer. Therefore, study for solvent migration in polymer and associated swelling deformation is important to understand and control this new class of micro actuation. In particular, solvent migration in swelling polymer shows complex behaviour, as the interface of wet (rubbery) region moves along with solvent diffusion into the dry (glassy) region. The swelling deformation of the structure induces mechanical stress, which in turn affects the solvent diffusion because diffusion is strongly influenced by mechanical condition of the polymer network. This coupled diffusion and deformation is investigated more rigorously using viscoelastic material model and phenomenological diffusivity model in Chapter 6. In this chapter, a simple analytical

model is used to investigate the relationship between design parameters and time scale of the actuation.

Tanaka and Fillmore [10] suggested that kinetics of swelling gel can be explained via stress relaxation in polymer network induced by osmotic pressure. It is assumed that polymer is under compressive stress when it is dry and that the stress is relaxed when solvent is absorbed in polymer. Polymer swelling in solvent can be represented as quasi-static force equilibrium between stress gradient in polymer and friction from solvent penetration,

$$\nabla \cdot \tilde{\sigma} = f \frac{\partial \bar{u}}{\partial t} \quad (3.4)$$

where $\tilde{\sigma}$ is the stress tensor, \bar{u} is the displacement vector, and f is the friction coefficient between polymer network and solvent. Accompanied with the following constitutive equation (3.5), compatibility equation (3.6), and one dimensional assumption (3.7),

$$\sigma_{ik} = K \nabla \cdot \bar{u} \delta_{ik} + 2\mu \left(\varepsilon_{ik} - \frac{1}{3} \nabla \cdot \bar{u} \delta_{ik} \right) \quad (3.5)$$

$$\varepsilon_{ik} \equiv \frac{1}{2} \left(\frac{\partial u_k}{\partial x_i} + \frac{\partial u_i}{\partial x_k} \right) \quad (3.6)$$

$$\bar{u} = u(x, t) \quad (3.7)$$

where K , μ , and ε are bulk modulus, shear modulus, and strain, respectively, the equation (3.4) can be written as diffusion equation,

$$\frac{\partial u}{\partial t} = D \frac{\partial^2 u}{\partial x^2} \quad (3.8)$$

where $D = (K + 4\mu/3)/f$ is diffusion coefficient.

This equation of motion is used to analyze the swelling motion of cantilever beam with embedded microfluidic channel as shown in Figure 3.6a. From the experimental measurement of fully swollen state of polymer, one can determine the initial condition,

$$u(x,0) = \Delta L_0 \frac{x}{L} \quad (3.9)$$

where L is initial dimension of polymer and ΔL_0 is dimensional increment at fully swollen state. Also, we assume free stress at channel-polymer interface and fixed boundary condition on the dry side as below.

$$u(0,t) = 0 \quad (3.10)$$

$$\sigma_{xx}|_{x=L} = K \frac{\partial u}{\partial x} \Big|_{x=L} = 0 \quad (3.11)$$

By solving the equation (3.8) with the initial condition (3.9) and boundary conditions (3.10) and (3.11), displacement field and stress relaxation in polymer during swelling can be simulated. The result is shown in Figure 3.6. Note that the displacement field is normalized with respect to the total increment ΔL_0 and the stress to the Young's modulus E . Experimental result was fitted to determine diffusion coefficient D due to difficulty in measuring friction coefficient f . In addition to the numerical solution, it is well known that one can solve the diffusion equation (3.8) analytically using Fourier series and the characteristic time in the exact solution is $\tau = L^2 / D$ where $D = E / f$ [10]. This characteristic swelling time can be considered as a time scale of the actuation. It has been reported that the principle of plant movement is diffusive equilibration of pressure by internal fluid transport in elastic tissue and that its time scale is characterized by

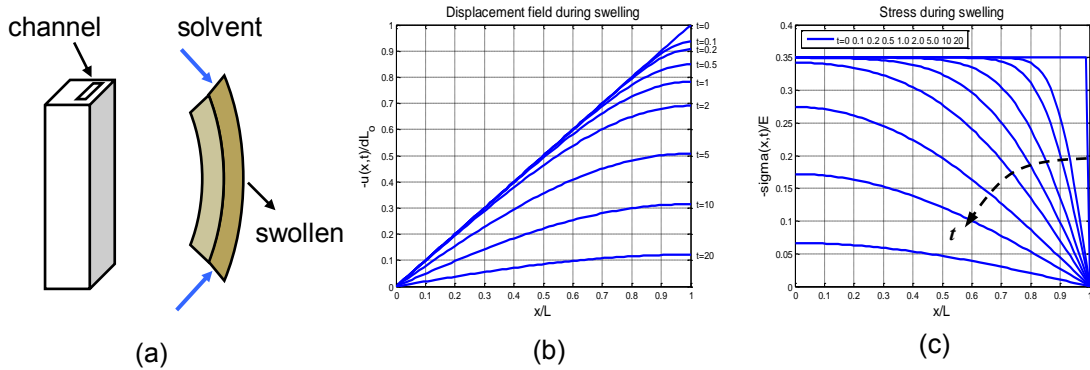


Figure 3.6 (a) Bending of beam caused by asymmetric swelling induced by solvent delivery through embedded channel. (b) simulated displacement field and (c) stress relaxation along the cross section (x -dir) during swelling ($L=75\mu\text{m}$, $D=2.2\times 10^{-10}\text{m}^2/\text{s}$)

poroelastic time $\tau_p \sim \mu L^2 / kE$, where μ is viscosity of internal fluid and k is hydraulic permeability [17]. It is important to note that actuation mechanism of our device and

moving plants results in the similar time scale. Furthermore, the time scale depends on the dimension as L^2 , which implies that we can enhance the speed of actuation effectively by reducing the size of actuator.

To simulate the bending motion of the cantilever beam, we approximate σ_{yy} to σ_{xx} obtained above under the isotropic swelling assumption for simplicity. Then non-uniform stress distribution creates bending moment in beams as illustrated in Figure 3.7 according to the following equation,

$$M_z(t) = \int_0^L \sigma_{yy}(x,t) \cdot w \cdot x \, dx \quad (3.12)$$

where w is the thickness of the beam in z direction. Angular displacement of beam can be estimated from the bending moment from beam theory [20].

$$\theta(t) \sim \frac{M_z(t)}{I_{zz}} \quad (3.13)$$

Bending motion of swelling beams with different dimension in width was simulated using above equations and shown later in Figure 3.12 along with experimental result.

Although this analysis is based on some approximations and used a fitting parameter of f , it gives essence of scaling law for swelling actuation time scale. More

rigorous modeling effort is presented in Chapter 6.

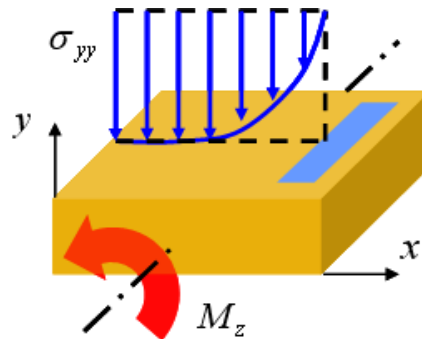


Figure 3.7 Schematic diagram of bending moment development on the cross section of beam due to non-uniform stress distribution

3.3 CHARACTERIZATION OF SWELLING-DRIVEN MOTION

As a fabrication method for 3D polymeric device with embedded microfluidic channels, projection micro-stereolithography(PμSL) [16] discussed in Chapter 2 is used. Poly(ethylene glycol) diacrylate (PEGDA, MW575) hydrogel is used, but any photo-curable polymer that swells in solvent can be used for the device actuated in this principle.

3.3.1 SWELLING CHARACTERIZATION

To understand fundamental swelling characteristics of hydrogels, equilibrium swelling test was carried out for different processing conditions and different solvents. PEGDA specimen as shown in Figure 3.8a was fabricated to study the effect of crosslinking ratio of polymer on swelling. First pillar was polymerized under higher light

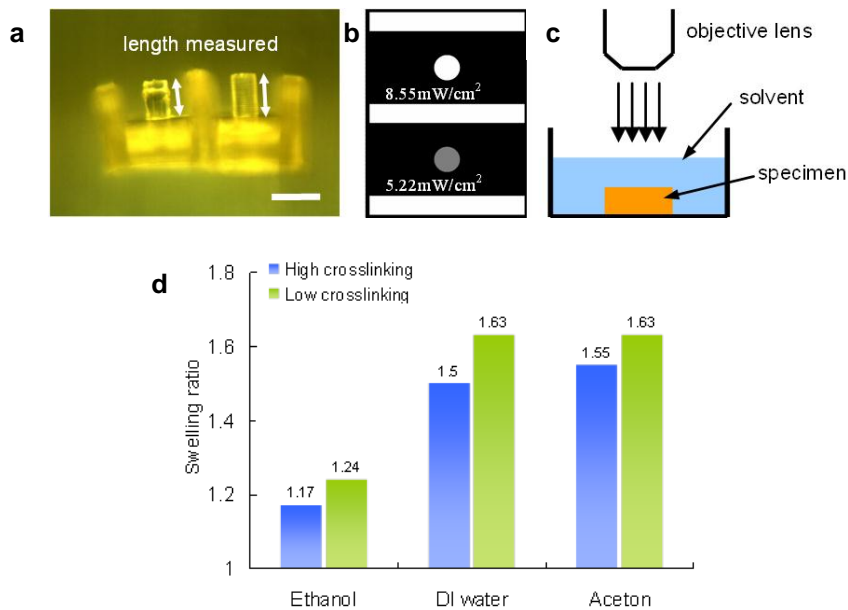


Figure 3.8 (a) Swelling ratio test specimen (b) Gray scale of sliced image enables light intensity control within a projection plane during fabrication (c) Experimental setup (d) Equilibrium swelling ratio in different solvents.

intensity ($8.55\text{mW}/\text{cm}^2$), thus has higher crosslinking density, and the second pillar was polymerized under relatively lower light intensity ($5.22\text{mW}/\text{cm}^2$), thus has lower crosslinking density. Light intensity was controlled within a projection plane by using gray-scale image mask shown in Figure 3.8b. Exposure time for each layer was 15 seconds and thickness of each layer was $25\ \mu\text{m}$. This specimen was immersed into ethanol, de-ionized (DI) water and acetone in which its swelling ratio was measured through microscope (Figure 3.8c) until it reached steady state. From the result shown in Figure 3.8d, we see that swelling ratio of lower cross-linking density is higher than that of higher crosslinking density. This result coincides well with the prediction from the analysis shown in Figure 3.3. In addition to cross-linking density, swelling ratio also

depends on solvent because of different Flory interaction parameter for different solvents. Figure 3.8d shows that swelling ratio in DI water and acetone is comparable but larger than in ethanol. This result not only provides qualitative validation of the theoretical prediction, but also demonstrates that swelling behavior of the structure can be altered by controlling process condition of P μ SL.

3.3.2 GENERATION OF MOTION

3.3.2.1 Direct solvent delivery through microfluidic channels

Leaf folding of *Mimosa pudica* results from selective swelling of cells. Likewise, local swelling control in hydrogel structure is essential to create motion in hydrogel devices. In this work, it is realized by direct delivery of solvent through embedded microvascular network. Taking advantage of 3D fabrication capability of P μ SL, embedded microfluidic channels in the structure can be designed and fabricated as shown in Figure 3.9a. Once the inlet of the channel touches solvent droplet, the channel is immediately filled with solvent via capillary action. Then, the solvent diffuses into the polymer network through the channel wall, which results in local swelling around the channel, unlike other hydrogel systems in which the entire device needs to be immersed in solvent for actuation. Asymmetric swelling gradient develops when the channels is positioned off the center as shown in Figure 3.9a, causing the structure bend as demonstrated in Figure 3.9b. More complex movement can be designed by appropriate selection of the distribution and dimension of the embedded microfluidic network. This motion only requires a single droplet of solvent, with no need for any valve-pump system and external power supply. In addition, wedge-shaped cross-section of the channel

(Figure 3.9a) facilitates fast evaporation of solvent through the opening, allowing for quick geometrical restitution when allowed to dry for reversible actuation.

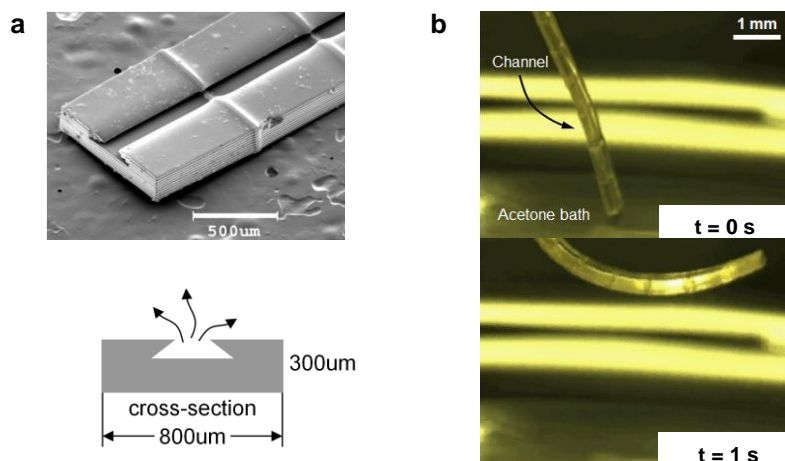


Figure 3.9 (a) SEM image of the hydrogel beam with embedded microfluidic channel. Lower image shows cross-sectional shape and dimension. (b) Actuation of the device. Microfluidic channel is embedded facing to the left side. When the tip of the channel touches solvent, solvent fills the channel via capillary force and subsequent local swelling around the channel makes the beam bend.

3.3.2.2 Crosslinking density control using gray scale mask

Local swelling is important in motion generation and it is shown above that direct solvent delivery through microfluidic network creates swelling gradient in polymer structure for bending motion. This method is novel and good, especially for transient motion, but may not be the best approach when the deformed configuration needs to be kept over time, or a “grab-and-hold” type of actuation, because swelling gradient disappears as solvent further diffuses and the hydrogel eventually becomes its original shape with increased dimension, in as shown in Figure 3.10a. In addition, it is obvious that this actuation principle is not applicable for devices operating in water. In such cases, swelling actuation can be created by local crosslinking density control. As demonstrated

in Figure 3.8, crosslinking density can be tailored at a single pixel level by controlling UV light illumination intensity using gray scale images and digital dynamic mask generator in P μ SL. This means that crosslinking density can be heterogeneously distributed over the polymer structure to create swelling gradient in equilibrium swelling owing to the fact that swelling ratio depends highly on crosslinking density as shown in Figure 3.3.

Figure 3.10b depicts how swelling motion is created by varying crosslinking density in a structure. Crosslinking density of the beam is low on the right half and high

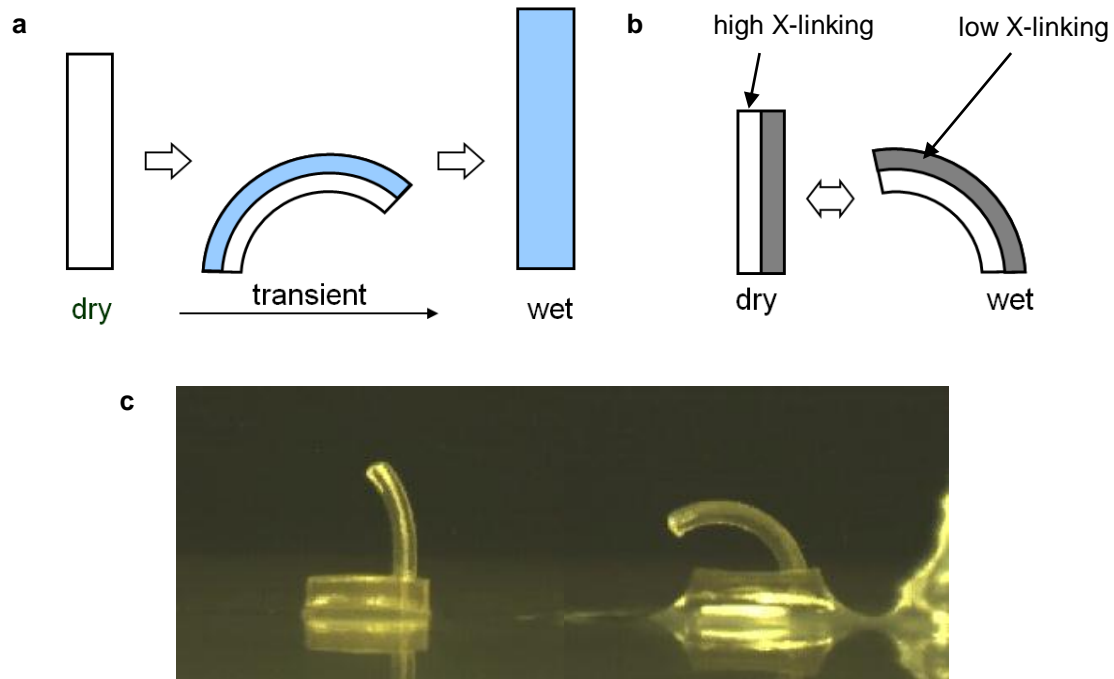


Figure 3.10 (a) swelling gradient by local solvent delivery. Motion is transient response and disappear in equilibrium swelling state (b) swelling gradient by different swelling ratio and (c) demonstration of the actuation.

on the left half. Allowed to swell, low crosslinked side expands larger than the high crosslinked side, making the structure bend. Deformed shape lasts without shape

restitution as long as it is wet. Figure 3.10c shows the device actuation demonstrated in this mechanism. Here a microfluidic channel is used not to generate swelling gradient but to supply the solvent, thus it is embedded at the center of the beam. This actuation may find applications for under water actuators such as cell manipulators and vascular stent.

3.3.3 DIFFUSION AND ACTUATION TIME SCALE

In order to investigate the controllability of actuation time scale, we designed six cantilever beams with embedded microfluidic channel as shown in Figure 3.11a. All the beams are 1400 μm long and 200 μm wide. Channels are 150 $\mu\text{m} \times 50 \mu\text{m}$ in cross section, and embedded 25 μm from the beam's outer surface. The dimension of the remaining part in the cross section where solvent needs to propagate through varies from

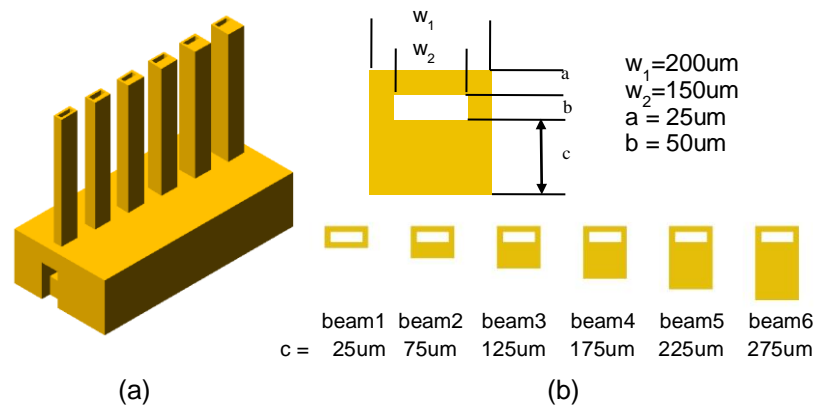


Figure 3.11 (a) Bending beams with embedded micro fluidic channels (beam height: 1400 μm , base: 2400 $\mu\text{m} \times 1200 \mu\text{m}$). Channels are connected together in the base for simultaneous solvent delivery to all channels. (b) Cross sectional dimensions of each beam.

25 μm up to 275 μm with 50 μm increment (Figure 3.11b). When a droplet of solvent is applied to the opening of the channel at the base, all the channels are filled with solvent

automatically and immediately by capillary action. Then, area near the channel becomes wet first while the other side remains dry due to finite solvent penetration speed.

Therefore, non-uniform stress distribution is developed because stress relaxation takes place only in wet region as explained by the theory discussed above. Since the ratio of swollen to dry region is different in each beam, time scale and deflection of bending motion is different as shown in Figure 3.11. Note that beam 1 does not bend but extends only because of uniform stress distribution due to its symmetric cross section. Bending motion was recorded from the front of the sample as shown in Figure 3.12a. From this video, the distance between the tip and the base of each beam was measured and bending

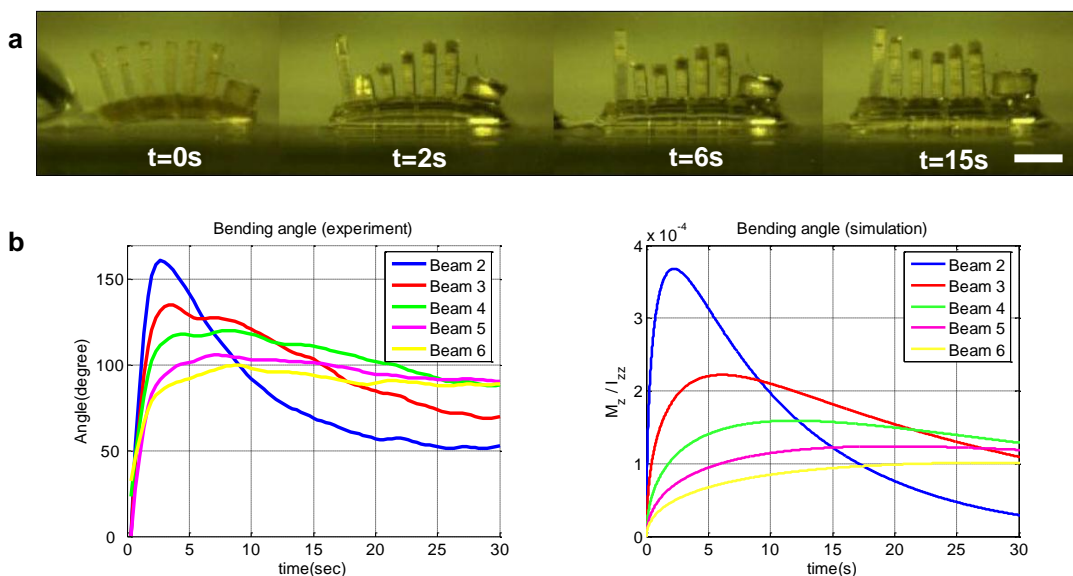


Figure 3.12 Diffusion length as a limiting factor for actuation time scale. (a) time-lapsed images of beam bending during swelling actuation. Channels are on the back of the beams and therefore bending direction is toward the front. Scale bar indicates 1 mm. (b) Bending angle with time measured from experiment (left) and simulation (right)

angle has been obtained using simple geometric relationships as shown in b. Not only does this result verify the theoretical model presented in the previous chapter, but it also demonstrates that the actuation time scale of this device is highly tunable in design stage.

3.3.4 SWELLING ACTUATION TIME SCALE LIMIT

3.3.4.1 Plant motion and poroelastic time scale

Swelling driven motion control by local swelling is inspired by plant motion. In fact, there are host of moving plants in nature displaying dynamic motions for different purposes including nutrition, defense, and pollination. Skotheim and Mahadevan [17] classified various non-muscular plant movements based on physical basis of the motion. They also explained swelling driven plant motion as diffusive equilibration of pressure via fluid transport in soft, elastic tissue. They derived poroelastic time scale $\tau_p \sim \mu L^2 / kE$ (μ : fluid

viscosity, k : permeability, E : elastic modulus) which separates plants movement into two categories; slow movement limited by water transport and rapid movement relying on elastic instability. Therefore, time scale of swelling driven plant motion is limited by this

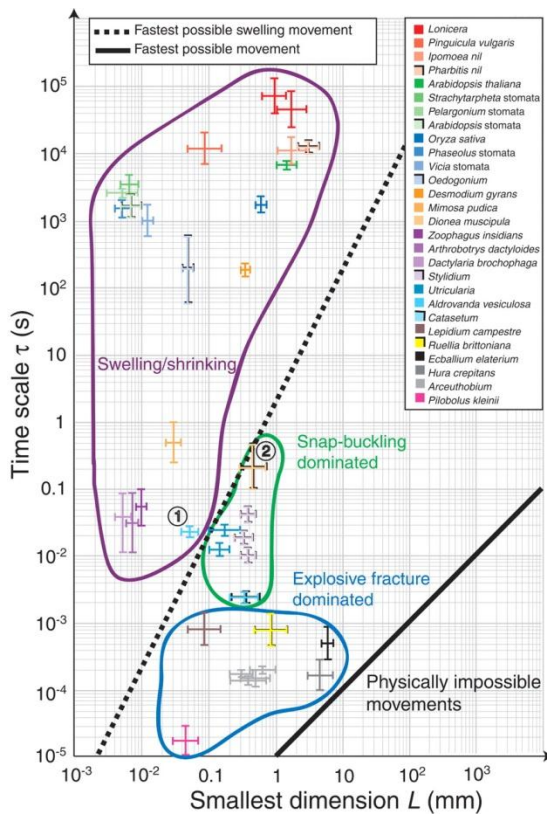


Figure 3.13 Classification of plant movements [17]

characteristic time scale which depends highly on the length scale. This suggests that rapid actuation requires either small size or incorporation of other mechanisms such as elastic instability. It is interesting to note that poroelastic time scale is in the same form of the characteristic swelling time scale of gel $\tau_s \sim fL^2 / E$ (f : viscous friction coefficient) obtained from Tanaka and Fillmore's model discussed in previous section. This further suggests that swelling motion of the polymeric actuators is also limited by the poroelastic time scale τ_p .

In order to find the limiting time scale of swelling driven polymeric actuation, permeability of the polymer was measured using Darcy's law as shown in Figure 3.14. Hydrogel was polymerized inside a glass tube and water transport driven by pressure P through the gel was measured by monitoring water meniscus movement on the other side of the gel. From the cross sectional area A and meniscus movement over the period of time, water flux J can be calculated. With known fluid viscosity, permeability k of the gel was obtained using Darcy's law. Permeability of the PEGDA hydrogel measured in this way is $k \sim 10^{-19} \text{ m}^2$. Using viscosity of acetone $\mu = 0.32 \times 10^{-3} \text{ Pa} \cdot \text{s}$ and Young's modulus $E = 10 \text{ MPa}$, poroelastic time scale of our swelling actuator is obtained as

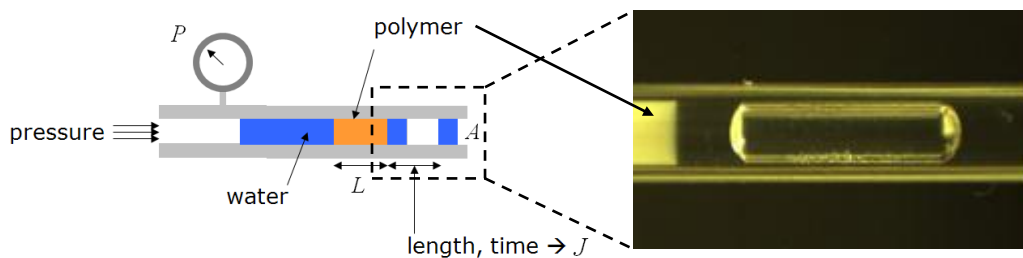


Figure 3.14 Polymer permeability measurement based on Darcy's law.

$$\tau_p \sim \frac{\mu}{\kappa E} L \sim \frac{0.32 \times 10^{-3}}{10^{-18} \times 10^7} L^2 \sim 3.2 \times 10^2 L^2 \text{ [s/mm}^2\text{]}. \quad (3.14)$$

To compare this with experiment, time scale of actual swelling motion was measured. Polymer beams with microfluidic channels as shown in Figure 3.15a were fabricated. Here the wall thickness of the beam is the diffusion length which determines motion time during swelling actuation. The length change of each beam was measure and plotted in scale. As the channel is at the center of the beam, beams stretch only without bending Figure 3.15b. Curves are fitted to the dynamic response of 1st order system, $L(t) = A - B \exp(-t/t_0)$, and time scale is defined as time at which the response reaches 63% $(1 - 1/e)$ of the steady state value. Result is listed in Table 3.1.

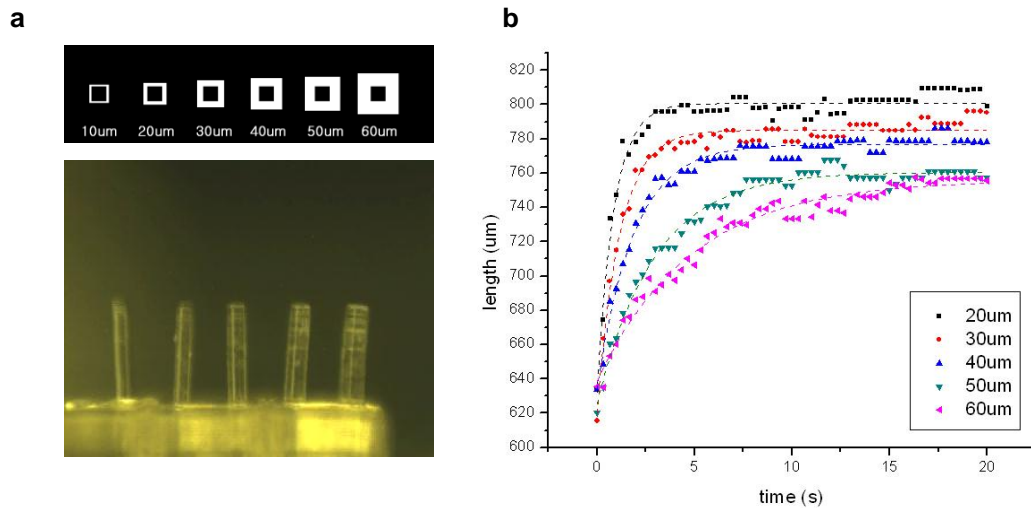


Figure 3.15 (a) polymer beams with different length scale for time scale measurement. Cross sectional area (above) and experiment (below). (b) length change of each beam with time, which is fitted to 1st order system to obtain swelling time scale.

Table 3.1 Fitting results and time scales of beams with different length scale.

| | A (μm) | B (μm) | t_0 (sec) | R^2 |
|------|-----------------------|-----------------------|-------------|-------|
| 20um | 802 | 169 | 0.76 | 0.94 |
| 30um | 788 | 166 | 1.06 | 0.94 |
| 40um | 779 | 143 | 1.67 | 0.97 |
| 50um | 762 | 135 | 2.57 | 0.98 |
| 60um | 758 | 118 | 4.32 | 0.98 |

Poroelastic time scale obtained in equation (3.14) is drawn together with experimentally measured time scale of swelling beams in Figure 3.15. We see that the swelling actuation of our device is indeed limited by poroelastic time scale as plant motion is. In plant kingdom, however, there are rapidly moving plants beyond the poroelastic time scale by gaining additional speed from elastic instability such as snap-buckling and fracture explosion [17]. Because the swelling actuation of our device is based on the same principle, the actuation speed of swelling driven actuators can also be enhanced by following nature's guide. This is covered in the next chapter.

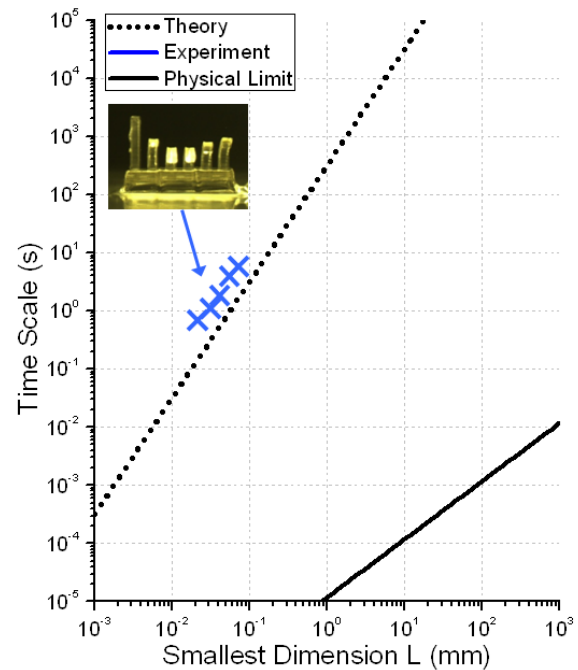


Figure 3.16 Swelling actuation time scale is limited by poroelastic time scale.

3.4 SWELLING-DRIVEN ACTUATORS: DEVICE DEMONSTRATION

3.4.1 ARTIFICIAL SENSITIVE PLANT

To demonstrate that the motion can be programmed by appropriate distribution of microfluidic network in this actuation mechanism, a micro polymeric device which mimics the movement of *Mimosa pudica* was fabricated. This artificial micro Mimosa consists of combination of beams as structural components and embedded capillary network for solvent delivery (Figure 3.17a). Each leaflet is 1000 μm long and half of it near the base has embedded channel inside branched out from main channel (Figure 3.17b). This part plays a role as a pulvinus which generates folding motion of leaves when solvent is delivered. Note that channel is located off the center axis of leaflet from

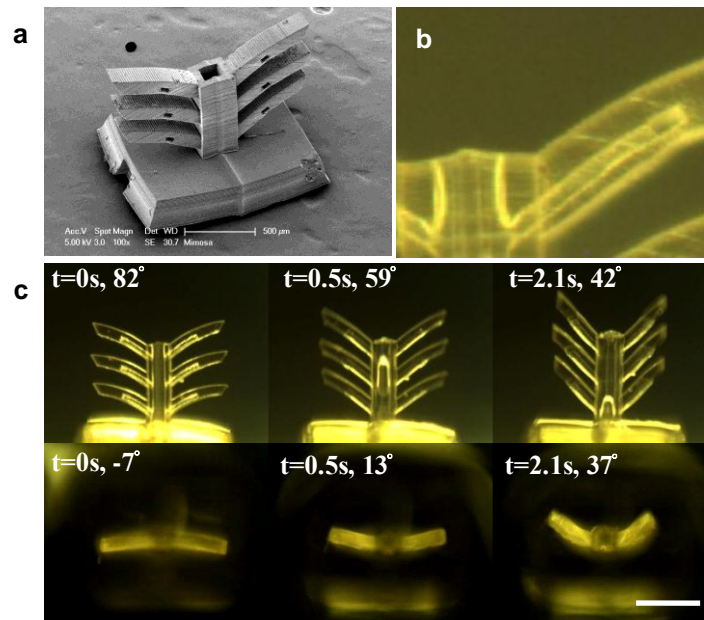


Figure 3.17 (a) Artificial micro Mimosa. (b) Embedded capillary network for solvent delivery. (c) Time-lapsed leaf folding motion of artificial micro Mimosa. Front view and top view. Scale bar in (c) indicates 500 μm .

both front view and top view so that bending occurs in vertical and horizontal direction simultaneously when swelling takes place. End of channels is open for an exit of the air inside as well as the ease of solvent evaporation during de-actuation (Figure 3.17b). Figure 3.17c shows leaf folding motion of artificial micro Mimosa. When a solvent droplet is applied, solvent is delivered to the base of leaves immediately by capillary action, leading to a fast folding of leaves. Angle of leaves to the main post in vertical plane changes from 82° when they are open to 42° when they are completely closed at $t=2.1$ s. Also, angle in horizontal plane changes from -7° when they are open to 37° at $t=2.1$ s. In addition, this motion is completely reversible because leaves return to its open position as solvent evaporates through openings at the end of channels. This result demonstrates that swelling of hydrogel can be controlled locally by designing capillary network accordingly, which enables fine tuning of direction of motion as well as its time scale in 3D space.

3.4.2 SOFT ROBOTIC GRIPPER

Soft robotic gripper that can do mechanical work was designed and fabricated as shown in Figure 3.18. Four swelling-driven actuator beams were put together equally spaced around the base post constituting gripping fingers. Each beam is 4 mm long, 1 mm wide, and $500\ \mu\text{m}$ thick. A wedge-shaped open surface channel of $500\ \mu\text{m} \times 200\ \mu\text{m}$ in cross section is embedded facing the center, making beams bend outward on acutation.

Channels from each beam are connected and merge into the main channel at the center of the base post where solvent droplet is applied. For P μ SL fabrication, layers thickness is $50\ \mu\text{m}$ and illumination time for each layer is 3 seconds. Fingers are closed in

its original configuration, but they open once solvent is supplied through embedded channels by applying a droplet on the main channel. When allowed to dry, fingers returns back to original shape as solvent evaporates through open channels. In this process, fingers can grip and hold an object as demonstrated in Figure 3.18. The object is a soft gel cylinder of 2.5mm in diameter, 3.2 mm in height, and 20mg in weight. The object can be release by applying another solvent droplet to open the figure because the actuation is fully reversible and repeatable. This soft robotic gripper does not require any other auxiliary devices such as battery and electronic wires, making the overall actuating system simple and compact. This gripping device may find applications where precise and self-operating manipulation of delicate objects is required, such as manipulation of living cells and tissues.

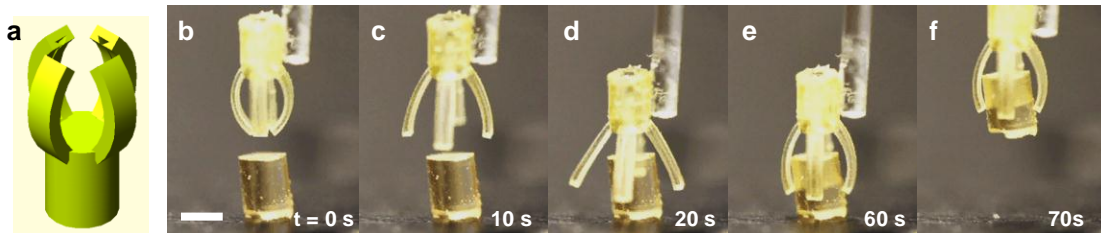


Figure 3.18 Soft robotic gripper. (a) CAD drawing (b) initial dry state (c) solvent droplet is applied to make fingers open (d) lowered to approach the object (e) allowed to dry to grip the object during deswelling (f) lifted to pick up the object. Scale bar is 2mm.

3.4.3 SELF-FOLDABLE ACTIVE ANTENNA

The ability of hydrogels to reversibly deform in response to external stimuli combined with 3D micro fabrication technology offers unique opportunities to explore a new class of transforming devices and systems. In particular, hydrogels have received much attention in the emerging field of flexible electronics where there is increasing

demand for reconfigurable structure into which electronic components are incorporated. Especially, reversibly deformable micro antenna will find numerous potential applications requiring wireless communication or remote sensing. As an example device, flexible electrode bearing self-foldable smart micro antenna array was fabricated. PEGDA beam ($800\mu\text{m}\times 500\mu\text{m}\times 5000\mu\text{m}$) with two embedded microfluidic channels was fabricated. One of the channels is filled with liquid metal alloy (Galinstan, melting point: -20°C , electrical conductivity: $3.46\times 10^6\text{S/m}$), and the other is for actuation solvent. Reversible actuation of PEGDA beam containing liquid metal alloy was successfully demonstrated as shown in Figure 3.19b. Figure 3.19a illustrates the operation concept.

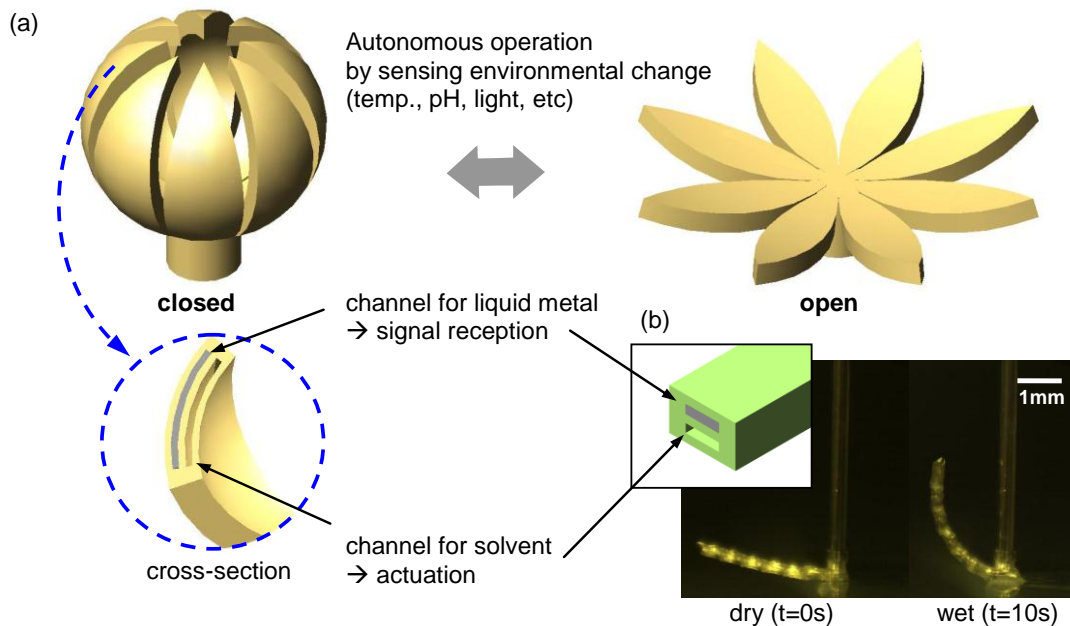


Figure 3.19 (a) Concept of foldable smart micro antenna array. (b) Swelling actuation of PEGDA beam with two microfluidic channels, one filled with liquid metal alloy.

500 μm thick and 4mm long straight polymer beam with embedded liquid electrode deforms to arc shape with radius of curvature of 1.7mm. Liquid metal alloy

integrated in the microfluidic channel in the hydrogel antenna not only functions as a signal receptor but also ensures electric continuity during significant deformation of the antenna. Deformation including the change in shape, dimension, and orientation can be translated into the modulation of antenna performance such as resonant frequency and radiation pattern. This smart antenna can be made to operate autonomously and reversibly by sensing environmental changes, such as temperature and humidity, depending on the choice of responsive hydrogels.

3.4.4 VASCULAR STENT

Vascular stent is an artificial tube inserted into a natural conduit in the body to prevent or counteract localized flow constriction. Stent should be compact in size so it can be navigated smoothly through vessels, and it should be able to radially expand upon activation once it is deployed at constriction site. Stent is widely used in the treatment of arterial stenosis to prevent acute vessel closure in a variety of large vessels [21]. Currently, most stent are made of metals such as stainless steel and shape memory alloys. However, metallic structure is often too stiff to navigate through complex vessel systems. More importantly, stiffness mismatch between metallic stent and soft vessel wall potentially causes restenosis [22]. Therefore, soft active materials such as shape memory polymer and responsive hydrogels are gaining attention for potential materials for vascular stent. Although there have been many reports regarding application of different soft materials for active vascular stent, manufacturing issue has been a remaining challenge because conventional material processing methods – machining, laser cutting, and molding, to name a few – do not offer capability of engineering soft materials into

micro-scaled intricate 3D tubular structures. Here, the present actuation principle enabled by P μ SL is used to demonstrate potential application of hydrogels for vascular stent.

PEGDA hydrogel stent was fabricated as shown in Figure 3.20a. Making use of digital dynamic mask of P μ SL, crosslinking density of the structure is heterogeneously distributed. As volumetric swelling varies depending on crosslinking density as discussed above, bimorph effect can be obtained with a single material. Blue part is highly crosslinked, thus it provides structural integrity with less swelling. On the other hand, gray part is less crosslink, so it swells and shrinks to add activeness to the device. By appropriately distributing these parts, radial expansion can be obtained. Figure 3.20b illustrates working principle of the device. In the experiment, angle between unit struts

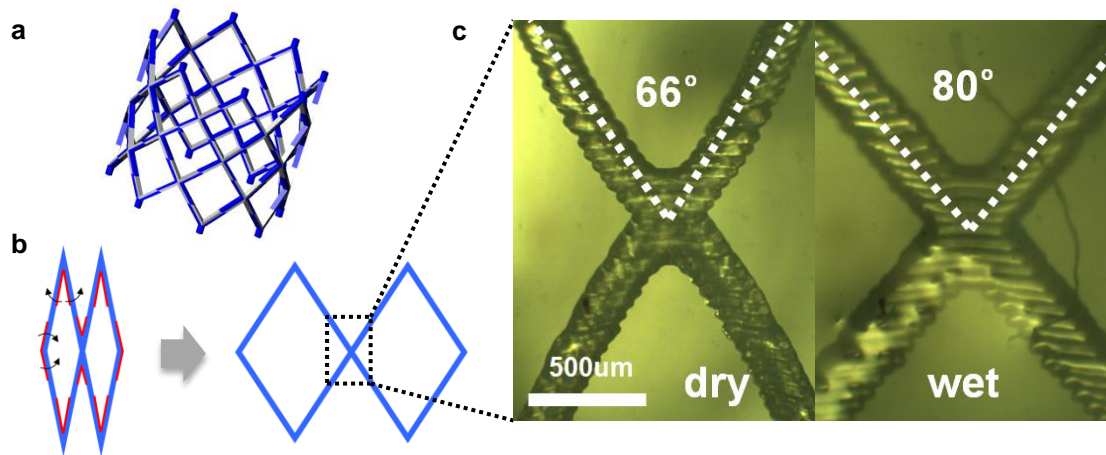


Figure 3.20 (a) CAD drawing of hydrogel stent. Blue and gray part indicates highly crosslinked rigid structure and low crosslinked swelling part, respectively. (b) Schematic of actuation of two unit cells of stent. Red part swells to expand the unit cells laterally (right). (c) Micrograph of PEGDA stent in dry (left) and swollen (right) states

were measured as shown in Figure 3.20c. Angle of 66° in dry state becomes 80° in wet state, which corresponds 8% of radial expansion. The expansion can be further increased

by carefully designing the thickness ratio of two parts. Also, the activation can be associated with external stimulus such as temperature if responsive hydrogel is used.

3.5 SUMMARY

This chapter presents a bio-inspired microactuator driven by polymer swelling. Embedded microfluidic channels in the device enables local control of stress at micro scale by delivering solvent to the specific location where swelling is needed for complex motion. Theoretical and experimental study of swelling shows that direction and speed of the actuation are highly tunable by design. This actuation mechanism requires no external power source but a single droplet of solvent for actuation. Actuation is fully reversible in that the moving components return to their original configuration as solvent evaporates. This actuation scheme has a great potential in a wide variety of applications, such as soft robotics, artificial muscle, and autonomous micro systems.

3.6 REFERENCES

1. Kovacs, G.T.A., *Micromachined Transducers Sourcebook*. 1998, Boston: WCB/McGraw-Hill.
2. Taya, M., *Bio-inspired design of intelligent materials*, in *EAPAD Proceedings of SPIE* 2003. p. 54-65.
3. Kuhn, W., et al., *Reversible Dilatation and Contraction by Changing the State of Ionization of High-Polymer Acid Networks*. *Nature*, 1950. **165**: p. 514-516.

4. Beebe, D.J., et al., *Functional hydrogel structures for autonomous flow control inside microfluidic channels*. Nature, 2000. **404**(6778): p. 588-590.
5. Dong, L., et al., *Adaptive liquid microlenses activated by stimuli-responsive hydrogels*. Nature, 2006. **442**(7102): p. 551-554.
6. Sidorenko, A., et al., *Reversible Switching of Hydrogel-Actuated Nanostructures into Complex Micropatterns*. Science, 2007. **315**(5811): p. 487-490.
7. Lendlein, A., et al., *Light-induced shape-memory polymers*. Nature, 2005. **434**(7035): p. 879-882.
8. Tanaka, T., et al., *Collapse of Gels in an Electric Field*. Science, 1982. **218**: p. 467-469.
9. Miyata, T., N. Asami, and T. Uragami, *A reversibly antigen-responsive hydrogel*. Nature, 1999. **399**(6738): p. 766-769.
10. Tanaka, T. and D.J. Fillmore, *Kinetics of Swelling of Gels*. Journal of Chemical Physics, 1979. **70**(3): p. 1214-1218.
11. Hong, W., et al., *A theory of coupled diffusion and large deformation in polymeric gels*. Journal of the Mechanics and Physics of Solids, 2008. **56**(5): p. 1779-1793.
12. Cao, X., S. Lai, and L. James Lee, *Design of a Self-Regulated Drug Delivery Device*. Biomedical Microdevices, 2001. **3**(2): p. 109-118.
13. Gerlach, G., et al., *Chemical and pH sensors based on the swelling behavior of hydrogels*. Sensors and Actuators B: Chemical, 2005. **111-112**: p. 555-561.
14. Kim, D. and D.J. Beebe, *Hydrogel-based reconfigurable components for microfluidic devices*. Lab on a Chip, 2007. **7**(2): p. 193.

15. Guan, J., et al., *Self-Folding of Three-Dimensional Hydrogel Microstructures*. The Journal of Physical Chemistry B, 2005. **109**(49): p. 23134-23137.
16. Sun, C., et al., *Projection micro-stereolithography using digital micro-mirror dynamic mask*. Sensors and Actuators A: Physical, 2005. **121**(1): p. 113-120.
17. Skotheim, J.M. and L. Mahadevan, *Physical Limits and Design Principles for Plant and Fungal Movements*. Science, 2005. **308**(5726): p. 1308-1310.
18. Flory, P.J. and J. Rehner, *Statistical mechanics of cross-linked polymer networks II: Swelling*. Journal of Chemical Physics, 1943. **11**(11): p. 521-526.
19. Ward, I.M. and D.W. Hadley, *An Introduction to the Mechanical Properties of Solid Polymers* 2nd ed. 1993, Chichester, New York: J. Wiley & Sons.
20. Shames, I.H., *Introduction to Solid Mechanics*. 2nd ed. 1989, Upper Saddle River: Prentice-Hall, Inc.
21. Small, I.V.W., et al., *Biomedical applications of thermally activated shape memory polymers*. Journal of Materials Chemistry, 2010. **20**(17): p. 3356.
22. Rolland, P.H., et al., *Compliance Matching Stent Placement in the Carotid Artery of the Swine Promotes Optimal Blood Flow and Attenuates Restenosis*. European Journal of Vascular and Endovascular Surgery, 2004. **28**(4): p. 431-438.

4. ACTUATION SPEED ENHANCEMENT BY SNAP- BUCKLING INSTABILITY

4.1 INTRODUCTION

Adaptive materials that can sense and react to external signals have been attracting growing attention in various fields of science and engineering because of their potential for autonomous and multifunctional devices and systems. Hydrogels, which swell and contract in response to a wide range of environmental changes, have been intensively studied as one of the most promising functional materials [1-7]. However, the operation speed of hydrogel-based devices is inherently limited by the slow diffusion of solvent into polymer network[2]. On the other hand, nature offers a novel solution to breach this barrier as demonstrated in the insect-trapping action of Venus flytrap. This astonishingly fast motion is attained by involving snap-buckling instability [8, 9]. Inspired by this exquisite mechanism, this chapter presents rapid actuation of a micro hydrogel device by exploiting swelling-induced snap-buckling [10]. Utilizing its fast actuation speed, the device can even jump by itself upon wetting. It is demonstrated that elastic energy is effectively stored and quickly released from the device by incorporating elastic instability. In our experiment, the micro device could generate a snapping motion within 12 milliseconds, releasing power at a rate of 34mW/g. This engineered microgel will open up new gateways for intelligent systems in diverse fields, such as microfluidics, soft robotics, artificial muscle, and biomedical engineering.

Hydrogels are a network of polymer chains that undergoes volumetric change upon solvent absorption. Since the first demonstration of reversible expansion and contraction of hydrogels [1], this unique phenomenon has been intensively studied experimentally [1-7] and theoretically [11, 12]. More recently, many hydrogels have been found responsive to a variety of environmental stimuli such as temperature, pH, light, electric field and many others [1-7]. Along with the direct conversion of chemical energy to mechanical work, the responsive properties of hydrogels make it possible to integrate multiple functions including sensing and actuation in a single device, which leads to diverse applications in microfluidics [2], optics [3], and drug delivery [13].

What remains as a challenge, however, is to fulfill a high speed operation in hydrogel devices. Swelling of hydrogel occurs when solvent diffuses into polymer network. Since diffusion time of solvent molecules scales with diffusion length of polymer as L^2 in general [11], the need of fast actuation is pushing down the ultimate dimension of the hydrogel devices [2]. However, miniaturization often causes inevitable sacrifices in operating stroke, mechanical strength, and/or reliability. More importantly, required actuation speed of a device is not necessarily matched with dimension. Hence, the dependence of operation speed on dimension is definitely a hindrance in exploring further possibilities for hydrogel devices.

Interestingly, one can find a similar dilemma in plant kingdom. Plants developed unique movements for different purposes such as nutrition [8], pollination [14], and defense [15]. These elaborate motions are based on swelling of cells induced by internal fluid flow. The time scale of this hydro-elastic motion, called poroelastic time, is

dependent on the square of the characteristic length scale of plants [9], which is exactly the same limitation as found in hydrogel swelling. Surprisingly, though, some carnivorous and sensitive plants learned to make rapid motions regardless of their size using elastic instability [8, 9]. In this mechanism, length scale is no longer a limiting factor. The Venus flytrap, for example, closes their leaves in a fraction of a second to trap insects. The doubly curved shape of their leaves leads to snap-buckling instability, making the leaf closure much faster beyond the poroelastic time [8]. In this way, Venus flytraps can have large but fast enough leaves to catch preys, which would not be possible without elastic instability.

In this chapter, swelling-induced snap-buckling, inspired by the insect-trapping action of Venus flytrap, is investigated to generate astonishingly fast actuation in a 3D micro hydrogel device. It is demonstrated that elastic energy is effectively stored and quickly released from the device by incorporating elastic instability. Utilizing its rapid actuation speed, the device can even jump by itself upon wetting.

4.2 THEORY: SNAP-BUCKLING INSTABILITY

Recent studies has unveiled the mysterious insect-trapping motion of Venus flytrap and found that secret is on the shape of their leaves; bending in doubly curved leaves gives rise to elastic instability which creates fast movement by snap-buckling [8]. Dimensionless total elastic energy of doubly curved plate due to bending and stretching deformation has been derived as

$$U(K_x, K_y, K_{xn}, \alpha) = U_{bending} + \alpha U_{stretching} = (K_x - K_{xn})^2 + (K_y - 1)^2 + \alpha(K_x K_y - 1)^2 \quad (4.1)$$

where $K_x = \kappa_x / \kappa$, $K_y = \kappa_y / \kappa$, and $K_{xn} = \kappa_{xn} / \kappa$ are dimensionless parameters representing the curvature in x direction, the curvature in y direction, and the natural curvature in x direction, respectively. The dimensionless geometric parameter $\alpha = L^4 \kappa^2 / h^2$ (L : radius of doubly curved plate, κ : initial curvature, h : thickness of doubly curved plate) determines the degree of coupling between bending and stretching energy. For a given α , the shape of the plate as a function of K_{xn} can be found by minimizing the total elastic energy U , i.e. solving the following equations.

$$\frac{\partial U}{\partial K_x} = \frac{\partial U}{\partial K_y} = 0 \quad (4.2)$$

Figure 4.1a shows the solutions of equation (1.2) when $\alpha = 0, 0.5, 0.8, 1.0,$ and 1.5 . One can see that for α smaller than a critical value ($\alpha < 0.8$) the solution is unique, thus the shape of the shell changes continuously. On the other hand, for α greater than a critical value ($\alpha > 0.8$) a bi-stable region appears in which multiple solutions exist. In this region, there is discontinuity in elastic energy between one solution to the other as shown in Figure 4.2b where the dimensionless elastic energy is plotted. When the deformation reaches the point where it becomes mechanically unstable, the structure shifts into the other stable configuration in which the energy level is lower. The energy released from this energy gap is mostly converted into kinetic energy generating a rapid motion. This

phenomenon becomes more apparent as the coupling parameter α increases.

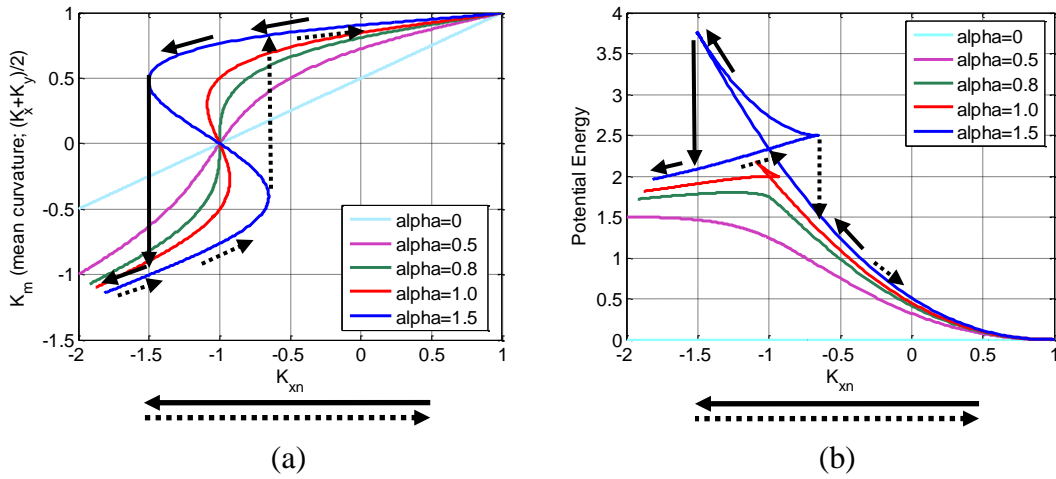


Figure 4.1 Snap-buckling instability and energy release for rapid motion. (a) Geometric change with respect to natural curvature. Snap-buckling occurs for $\alpha > 0.8$. (b) Dimensionless energy change with respect to natural curvature.

4.3 DESIGN AND FABRICATION

Following nature's guide as implemented in Venus flytraps, a hydrogel device in a doubly curved shape is designed and fabricated to incorporate elastic instability as illustrated in Figure 4.2. As a fabrication method for 3D polymeric device with embedded microfluidic channels, projection micro-stereolithography was used (P μ SL) [16]. It is capable of fabricating intricate three dimensional micro structures in a layer-by-layer fashion with a resolution up to 2 μ m. Firstly, 3D CAD drawing of the device is sliced into a set of layers. The image of each layer is sent to a Liquid Cristal on Silicon (LCoS, Canon) chip which plays a role as a dynamic mask generator. A flood of UV light (436 nm) from mercury lamp is reflected off the dynamic mask and then the beam containing the image is optically routed and focused on the surface of prepolymer solution through

the 10x reduction projection lens in the light path. Although fabrication area for one exposure is about 1200 μm by 800 μm , larger area can be covered using x-y stages. Once a layer is polymerized on the substrate, the z-stage drops the substrate under the surface of the solution by the thickness of the next layer, and the machine projects the next image to polymerize the following layer on top of the preceding layer. This process proceeds iteratively until all the layers are completed. Layer thickness of the doubly curved plate and the base of the device in this study are 15 μm and 25 μm , respectively. Light intensity on the prepolymer surface was 6.17 mW/cm^2 and exposure time for 15 μm and 25 μm thick layers were 12 s and 20 s, respectively.

The leaf is a 1200 μm by 1200 μm plate with thickness of 100 μm , and is convex outward with a radius of curvature of 800 μm . For solvent delivery, three microfluidic channels of 150 μm by 50 μm in cross-section are embedded with 400 μm spacing on the inner surface of the leaf. Thus, the device changes the curvature from convex to concave upon swelling. The embedded microfluidic channels play a critical role in generating a 3D motion. Unlike other hydrogel systems in which the entire device needs to be immersed in solvent for actuation, swelling in our device takes place locally around the channels by direct solvent delivery. Therefore, complex motion requires only a single droplet of solvent and the movement can be designed by appropriate selection of the distribution and dimension of the embedded microfluidic network. In addition, wedge-shaped cross-section of the channel (Figure 4.2b) not only promotes simple and fast delivery of solvent via capillary force, but also allows fast evaporation of solvent through

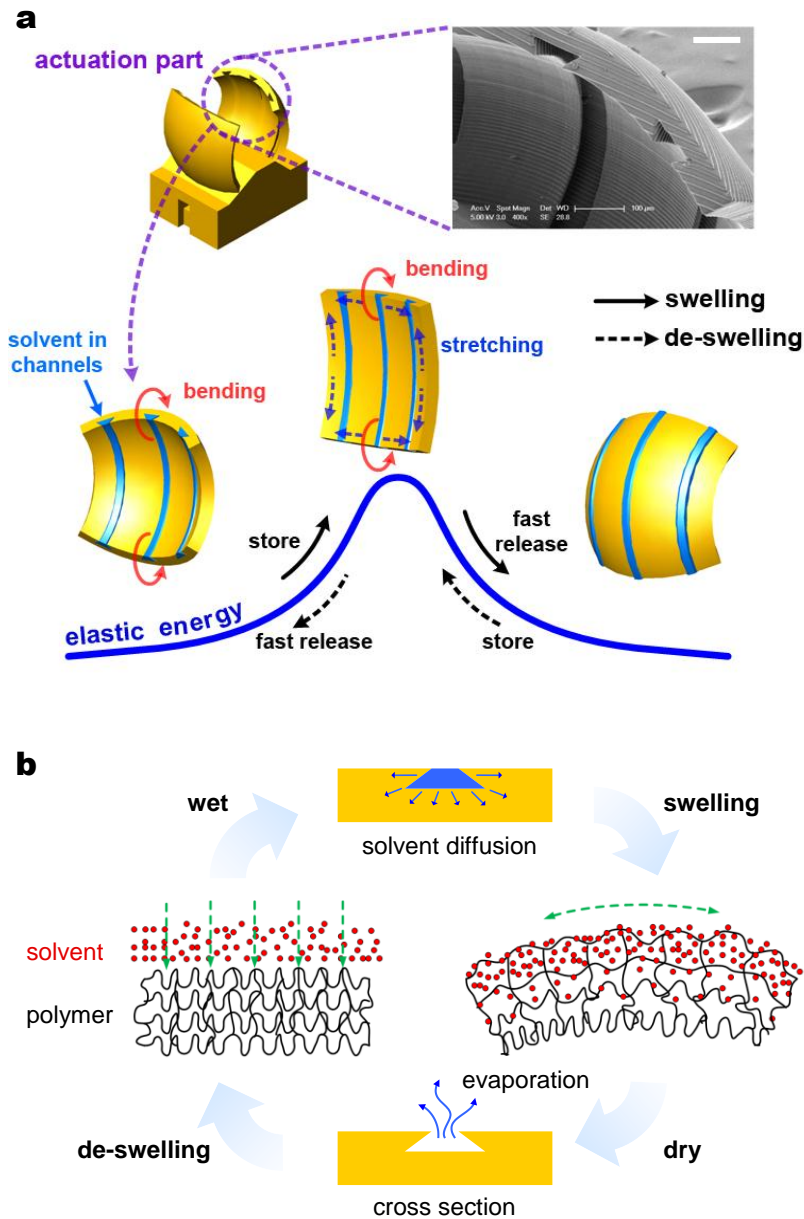


Figure 4.2 Swelling-induced snap-buckling in a doubly curved hydrogel device with embedded microfluidic channels. (a) 3D micro hydrogel device in doubly curved shape and scanning electron microscope (SEM) image of embedded microfluidic channels. Scale bar indicates 100 μm . (b) Swelling and de-swelling mechanism using embedded microfluidic channels.

the opening for quick geometrical restitution when the device is allowed to dry.

For snap-buckling instability, it is essential to create directional swelling deformation of the device in addition to the doubly curved shape. The Venus flytrap, for instance, actively regulates internal hydraulic pressure to bend their leaf in the direction perpendicular to the midrib [8]. In mechanical point of view, the leaf is an elastic plate in doubly curved shape. When bent along one axis only, elastic body becomes stretched as a result of bending-stretching coupling of doubly curved plate, thereby storing elastic energy. As the leaf further deforms and passes through the energy barrier, stored elastic energy is instantaneously released and converted into kinetic energy, creating a rapid trap closure. Likewise, the swelling of the device needs to be controlled in such a way that the curvature is actively manipulated only in one direction while the curvature in the other direction remains passive. Although there have been a few reports of fast polymer actuation using elastic instability [17, 18], full control over the motion has not been demonstrated so far due to the lack of local swelling control.

To achieve directional swelling of doubly curved hydrogel device, the microfluidic channels are aligned vertically with spacing in between, as depicted in Figure 4.3. Once supplied to the channels, solvent diffuses out in all directions around the channel. However, if the distance between the channels is far enough (400 μm), swelling deformation in lateral direction is negligible within a short period of actuation time since the solvent diffusion speed is finite. Thus, only small portion in the gap between the gap gets wet. On the contrary, swelling along the channels can quickly cause significant amount of bending in vertical direction as the diffusion length in thickness direction is

relatively short (50 μm). To quantitatively show this, the time scale of swelling in each direction can be roughly estimated. Time scale of diffusion is $\tau \sim L^2 / D$ where diffusivity can be taken as water diffusivity $D \sim 2 \times 10^{-9} \text{ m}^2/\text{s}$. Then diffusion time scale, thus swelling time scale, in lateral direction and vertical direction can be obtained by

$$\tau_{lateral} \sim \frac{(200 \times 10^{-6})^2}{2 \times 10^{-9}} = 20 \text{ s}$$

$$\tau_{vertical} \sim \frac{(50 \times 10^{-6})^2}{2 \times 10^{-9}} = 1.25 \text{ s}$$

It shows high contrast in time scale of swelling in different direction, justifying the hypothesis that directional swelling can be achieved by carefully design the distribution of microfluidic channels. In this way, local swelling around the aligned channels makes the doubly curved device bend only along the vertical axis and, as a result, snap-buckling occurs. Similarly, the device snaps back to the original shape during de-swelling as illustrated in Figure 4.2a.

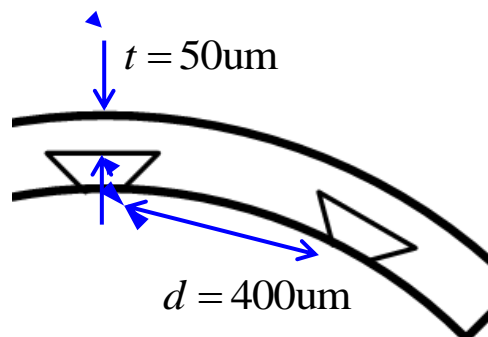


Figure 4.3 Cross section of the doubly-curved plate and the location of microfluidic channels. Directional swelling required to trigger snap-buckling instability results from the difference of diffusion length in different direction.

4.4 EXPERIMENT

4.4.1 MATERIALS

The prepolymer solution used to make the hydrogel consists of poly(ethylene glycol) diacrylate (PEGDA) (MW~575, Sigma-Aldrich) with 2.0 wt.% photoinitiator (Irgacure 819, Ciba) and 0.75 wt.% photoabsorber (Sudan I, Sigma-Aldrich). The solvent used for swelling is acetone (99.8%, Sigma-Aldrich).

4.4.2 SWELLING CHARACTERIZATION

Polymer specimen was fabricated to study equilibrium swelling ratio of the polymer in acetone (Figure 4.4b). The specimen was polymerized under 6.74 mW/cm^2 of UV (H-line, 436 nm). Exposure time for each layer is 12 seconds and thickness of each layer is $15 \text{ }\mu\text{m}$.

The length of specimen was measured through microscope when it was dry and when it was in equilibrium swelling state in acetone (Figure 4.4a). Swelling ratio here was obtained by dividing the swollen length by the dry length. From the result shown in Figure 4.4c, swelling ratio of the polymer under the fabrication condition described above is 1.42 ± 0.03 . This value will change under different fabrication condition because of different cross-linking density of polymer.

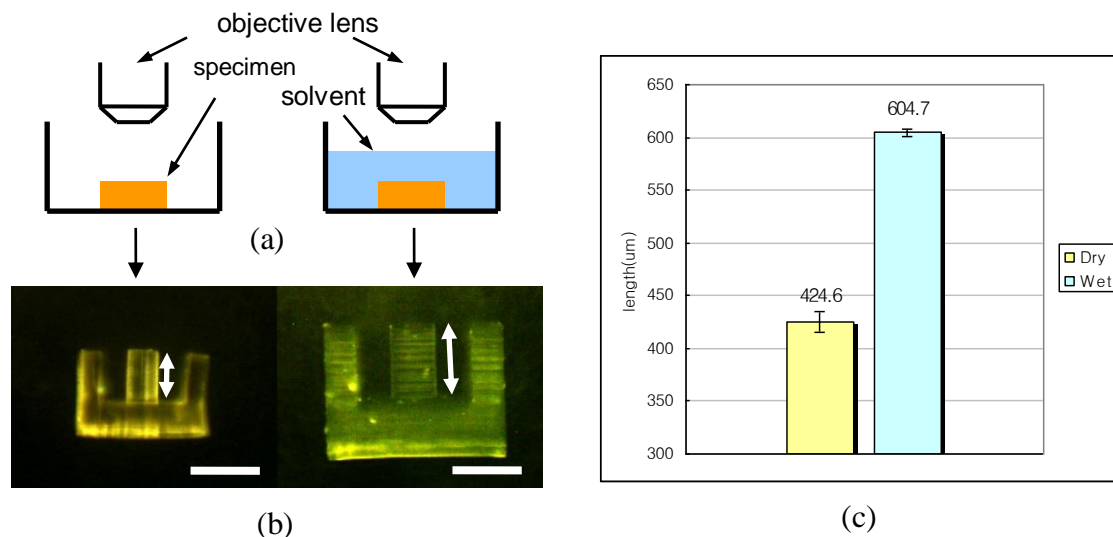


Figure 4.4 Measurement of equilibrium swelling ratio. (a) Experimental setup to measure the length of the specimen. (b) Specimen when it is dry (left) and swollen (right). Scale bar indicates 500 μm . (c) Length of the specimen measured when it was dry and swollen. Swelling ratio (swollen length / dry length) from the data is 1.42 ± 0.03 .

4.4.3 SNAP-BUCKLING ACTUATION EXPERIMENT

To investigate the effect of elastic instability on motion speed, the motion of the device were captured using high speed camera (Redlake Image, 250 fps). Image analysis software is used to measure the angle of the line connecting the tip and the base of the device from the initial configuration at each frame (Figure 4.5b). Geometric change in the snapping process of the doubly curved plate is shown in Figure 4.5c. The angle changed abruptly from 48° to 80° in 12 milliseconds with a maximum angular velocity as high as 100 rad/s. This is an exceptionally high speed to obtain in a hydrogel device. In comparison with natural system, angular velocity observed in most Venus flytraps' leaves is below 10 rad/s [8]. As a control experiment, another sample was tested that has the

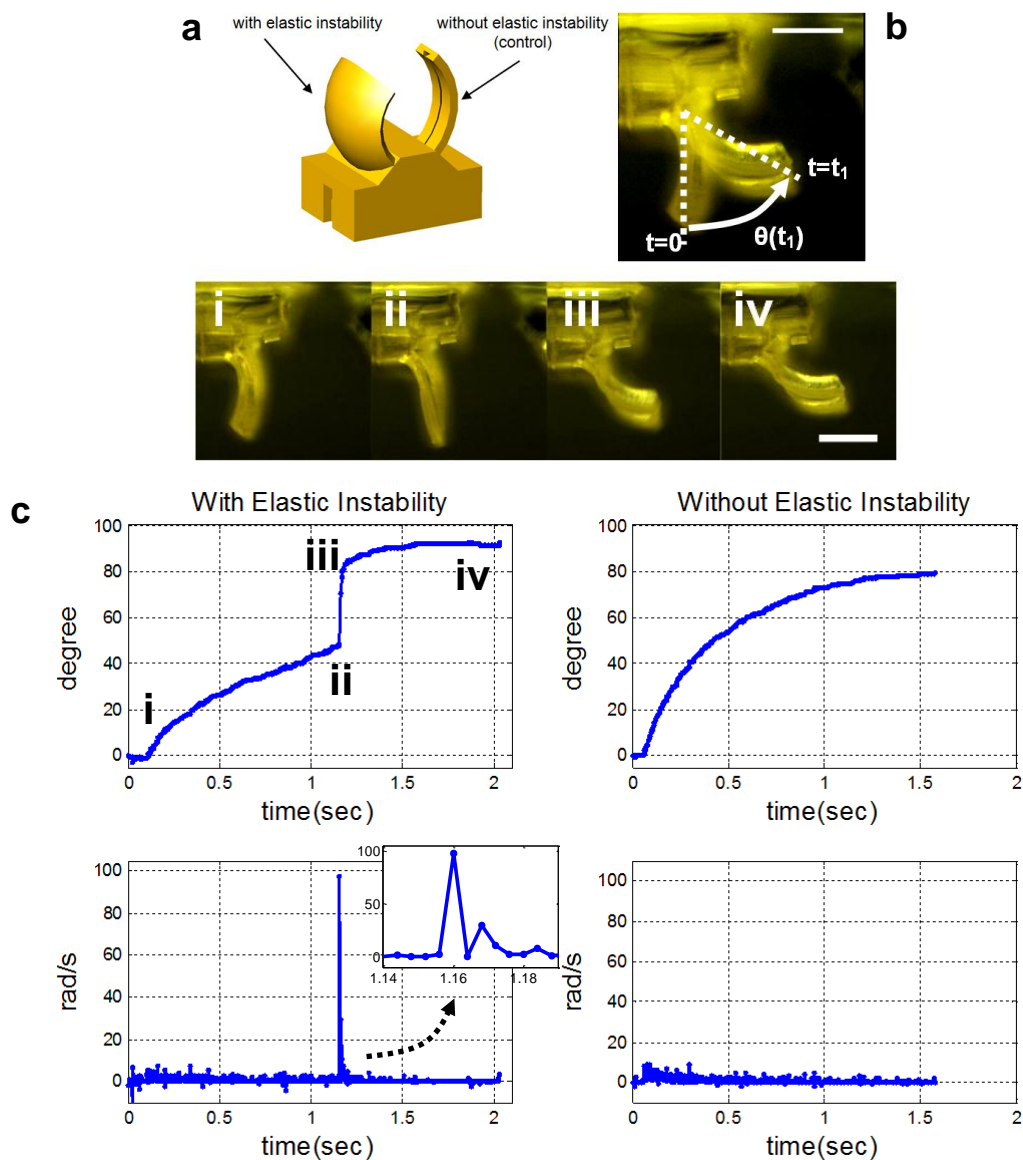


Figure 4.5 Enhancement of actuation speed by elastic instability. (a) 3D micro hydrogel device with elastic instability and a control sample. (b) Angle measurement during actuation. The doubly curved leaf points downwards. (c) angular displacement and angular velocity from actuators with (right column) and without (left column) elastic instability, respectively. The shape change of the device during actuation. Snap-buckling occurs between **ii** and **iii**. All scale bars indicate 500 μm .

same curvature in vertical direction but has no curvature (flat) in horizontal direction (Figure 4.5a). The control sample therefore experiences just uniaxial bending without elastic instability during actuation. The width of the control sample (400 μm) is one third of the doubly curved sample and it has a single channel in the middle, thus its structural resistance against swelling actuation is the same as the doubly curved sample. Resulting motion of the control sample exhibits a smooth and continuous angle change with a maximum angular velocity less than 10 rad/s. The sharp contrast of these two experiments shows remarkable enhancement of actuation speed of hydrogel device via elastic instability. Angular velocity was measured from several experiments as shown in Table 4.1. Although angular velocities in other measurements were not as high as 100 rad/s, they are all higher than the angular velocity of the control experiment (~ 10 rad/s) where there is no elastic instability. This proves that actuation enhancement by elastic instability is significant and reproducible.

Table 4.1 Actuation measurement from snap-buckling experiments

| | angular displacement ($^{\circ}$) | maximum angular velocity (rad/s) |
|--------------|-------------------------------------|----------------------------------|
| Experiment 1 | 32 | 97 |
| Experiment 2 | 22 | 78 |
| Experiment 3 | 24 | 80 |
| Experiment 4 | 18 | 55 |
| Experiment 5 | 15 | 39 |
| Experiment 6 | 14 | 44 |

4.4.4 EFFECT OF COUPLING PARAMETER ON SNAP-BUCKLING

Theory says that there exists critical value of dimensionless parameter α_{cr} , above which snap-buckling is observed. To experimentally validate this, five leaves with different value of α from 0.2 to 6.2 were fabricated and tested. Figure 4.6 shows detailed dimension and shape of each leaf. In our experiment, there was a clear distinction in motion between two groups of leaves; leaf 1 and 2 opened and closed continuously while leaf 3, 4, and 5 showed snap-through motion ($\alpha > 2.2$). Also we observed that snap-through velocity increases with α as expected by theoretical model. The curvature of leaf 5 changed its sign abruptly from 0.4 to -0.5.

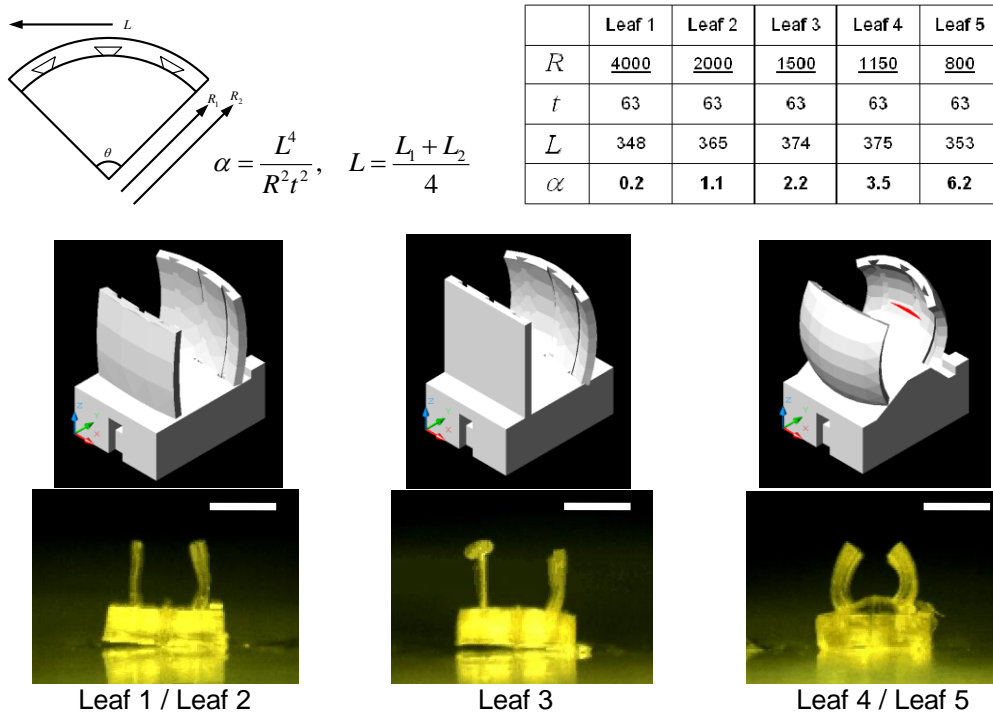


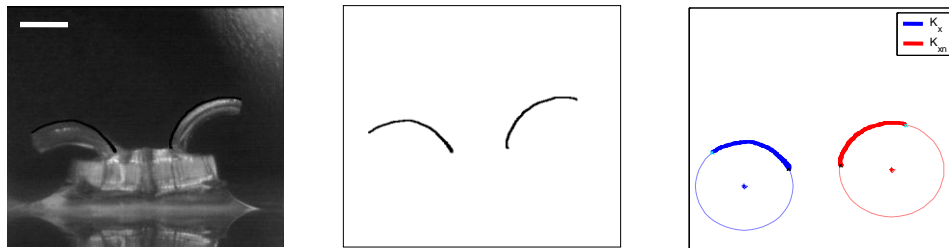
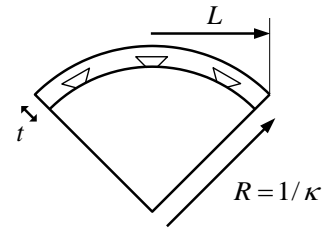
Figure 4.6 3D CAD drawing and microscope image of 5 leaves. All scale bars indicate 1mm.

Two doubly-curved plates with different coupling parameters were fabricated to investigate more quantitatively how the coupling parameter affects snap-buckling motion. Two samples have the same thickness h and length L , but different initial curvature κ , thus different dimensionless coupling parameter $\alpha = L^4 \kappa^2 / h^2$ (Table 2). Corresponding coupling parameter α of each sample is 3.5 and 6.2, respectively. For each device, the control sample was also fabricated to obtain the natural curvature κ_{xn} which would be the actual curvature without bending-stretching coupling. The motion was captured using high speed camera (Redlake Image, 125 fps) and extracted the curvature in vertical direction using circle fitting (Figure 4.7a; κ_x in the left, κ_{xn} in the right in each figure). Every frame (125 fps) was analyzed in the fast-moving range around the snap-buckling, but for the sake of efficiency every fifth frame (25 fps) was analyzed in slow-moving range before and after snap-buckling. Figure 4.7b shows the time course of the dimensionless curvature K_{xn} and K_x which are normalized with respect to the initial curvature. For both samples, the natural curvature K_{xn} changes smoothly, whereas at certain point the actual curvature K_x abruptly changed the sign from positive to negative, indicating the occurrence of snap-buckling. This is presented more effectively by plotting the actual curvature K_x against the natural curvature K_{xn} (Figure 4.7c). The result that the slope of transition is steeper for the high coupling sample implies that the snap-buckling is more significant when α is greater. If it were not for the bending-stretching coupling ($\alpha = 0$), they would follow the dotted line on which the actual curvature K_x and the natural curvature K_{xn} are the same. Furthermore, it takes more time to trigger

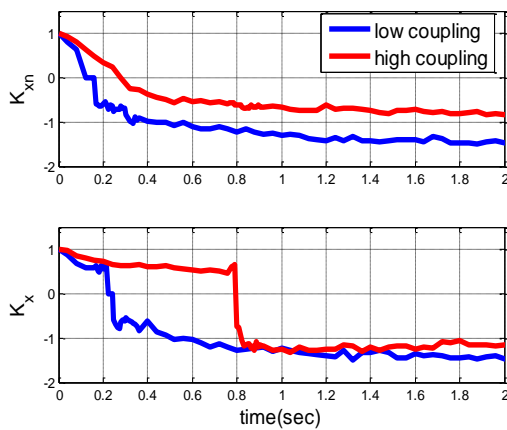
snap-buckling in high coupling sample (Figure 4.7b, lower), which implies that as α increases more elastic energy needs to be stored owing to higher energy barrier. This suggests that for greater α more energy is released during snap-buckling, hence one can expect faster actuation.

Table 4.2 Dimension for two samples with different coupling parameters

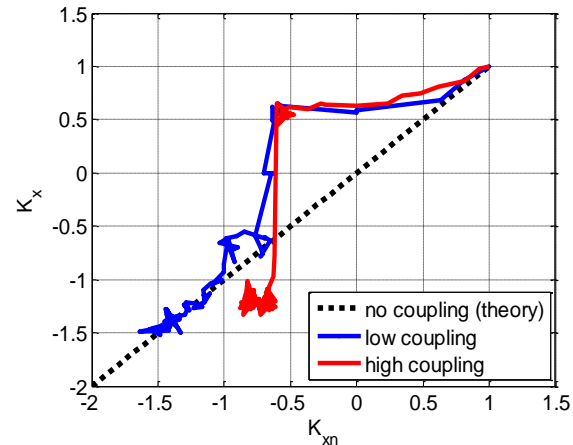
| | κ (μm^{-1}) | t (μm) | L (μm) | α |
|---------------|---------------------------------|-----------------------|-----------------------|----------|
| low coupling | 1/1150 | 63 | 370 | 3.5 |
| high coupling | 1/800 | 63 | 370 | 6.2 |



(a)



(b)



(c)

Figure 4.7 Coupling parameter and snap-buckling. (a) Image analysis to obtain the curvature of samples using circle fitting. (b) Dimensionless curvature change over time during experiment. (c) Actual curvature against natural curvature. The steeper the slope of transition (larger α), the more significant the snap-buckling is.

4.5 MICROGEL JUMP AND ESTIMATION OF ENERGY RELEASE

To demonstrate the maximum use of enhanced speed obtained by swelling-induced snap-buckling, a micro hydrogel device was made jump upon wetting (Figure 4.8). In this sample, both legs of the device are doubly curved hydrogel plates with embedded microfluidic channels. Hence, they open and close rapidly via snap-buckling during swelling and de-swelling, respectively. When a solvent droplet is applied, swelling causes the legs to open outward and consequently the device sits on the ground. When the device returns to its original configuration as the solvent evaporates, the legs close quickly by snap-buckling, generating a thrust to make the device itself jump off the ground. The numbers in Figure 4.8 indicate the sequence of the jumping event. The device is placed on a glass substrate (1). When a solvent droplet is applied to the left leg (2), the solvent not only

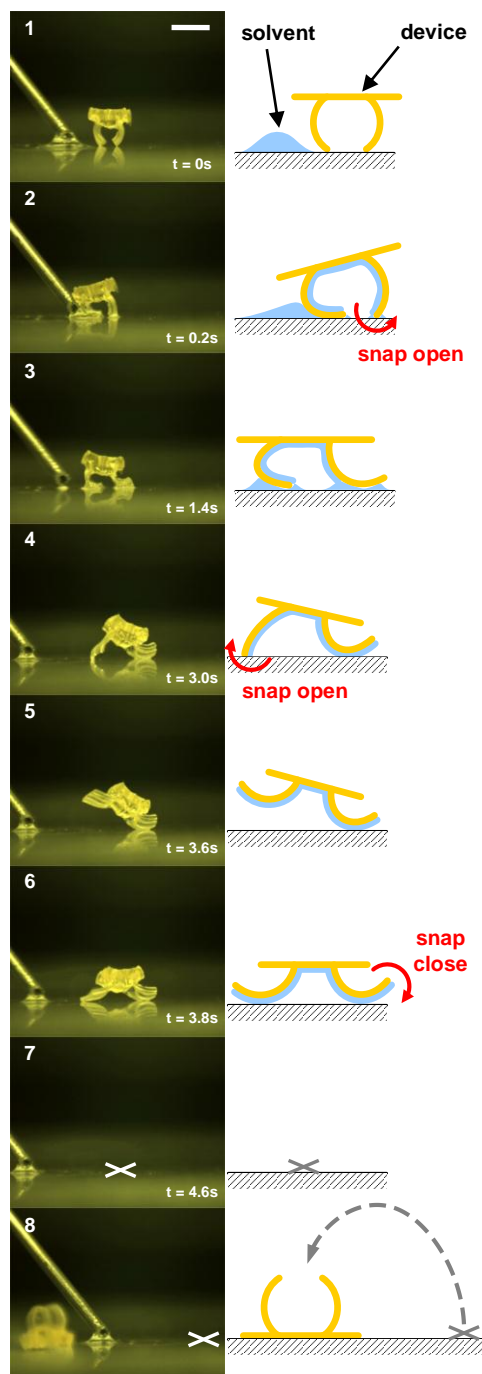


Figure 4.8 Microgel jump

surrounds the leg, it also fills all the microfluidic network in the device by capillary action. Even after solvent surrounding the legs evaporates, embedded microfluidic channels are still filled with solvent, resulting in bending of legs outwards (3-5). With two legs bent outwards, the device is ready to jump (6). As the solvent in the channels further evaporates, snap-buckling takes place as the legs snap back to the original shape in de-swelling process. This rapid motion produces enough thrust for jumping. The device jumps out of the view field (7) and is found outside the initial view field (8). Cross mark indicates the initial position of the device. It flew about 7 mm, which is about five times as long as its own length.

As the elastic energy stored in the device is converted into kinetic energy during snap-buckling, one can estimate how much energy was stored and released from the device by measuring the jumping trajectory. Energy release during snap-buckling was estimated from the jumping trajectory. Overall, stored elastic energy is converted into energy in several forms such as translation energy, rotation energy, internal dissipation by viscosity, energy required to overcome the stiction to the ground when it jumps, and energy consumed by drag from the air.

$$E_{elastic} = E_{translation} + E_{rotation} + E_{dissipation} + E_{stiction} + E_{drag} \quad (4.3)$$

The parabolic trajectory of jumping (Figure 4.9) allows us to calculate $E_{translation}$ which can be an estimation of the minimum energy released from the snapping motion because

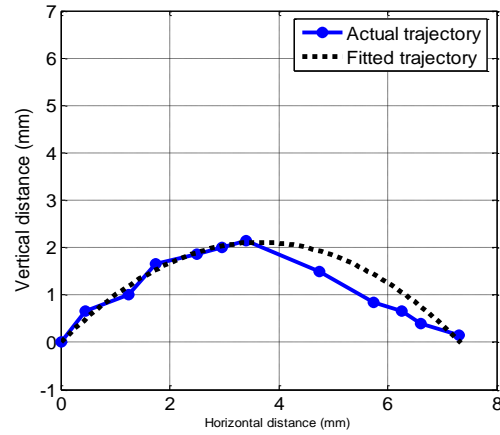
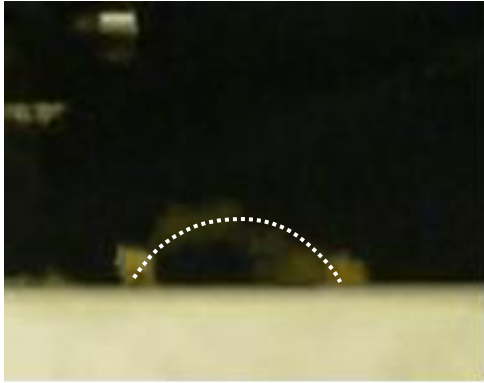


Figure 4.9 Jumping trajectory for energy analysis. Trajectory of jumping motion is measured from experiment and fitted to an ideal parabola for estimation of energy release.

$E_{elastic} > E_{translation}$. The measured distance and height of the parabolic trajectory are 7.33 mm and 2.11 mm, respectively. Provided that the trajectory is an ideal parabola following $(x, y) = (v_0 t \cos \theta, v_0 t \sin \theta - gt^2 / 2)$, one can calculate the launching angle $\theta = 49^\circ$ and initial velocity $v_0 = 260.7$ mm/s. Thus, it gives

$$E_{translation} = \frac{1}{2} m v_0^2 = \frac{1}{2} (0.75 \text{ mg})(260.7 \text{ mm/s})^2 = 25.5 \text{ nJ} \quad (4.4)$$

where $m = 0.75$ mg is the total mass of the device in dry state. Energy density of this device can be estimated by dividing the energy by the mass of the actuation part (a leg) only. With the actuation time of 12 milliseconds, the power density of the device can be estimated as follows.

$$\text{Energy density} = E_{\text{translation}} / m_{\text{leg}} = 25.5 \text{ nJ} / 0.062 \text{ mg} = 0.41 \text{ mJ/g} \quad (4.5)$$

$$\text{Power density} = (0.41 \text{ mJ/g}) / (12 \text{ ms}) = 34 \text{ mW/g} \quad (4.6)$$

which is comparable to that of our own muscle (100 mW/g) [19].

4.6 SUMMARY

This chapter presented a 3D microgel actuator and a method to significantly enhance the actuation speed of the devices by incorporating elastic instability. This actuation strategy can be also associated with a wide range of external stimuli (temperature, pH, light, etc.) with a proper choice of stimuli-responsive hydrogel. It is expected that adding agility to the integrated functionalities of hydrogel will greatly extend the potential of hydrogel devices and systems. The fast, responsive, and multifunctional devices enabled by this approach will allow us to envision entirely new opportunities in various fields, such as self-operating pumps and fast-switching valves in microfluidic devices, soft robots with artificial muscle, and fast drug delivery vehicles for prompt measures in medical emergency.

4.7 REFERENCES

1. Kuhn, W., et al., *Reversible Dilation and Contraction by Changing the State of Ionization of High-Polymer Acid Networks*. Nature, 1950. **165**: p. 514-516.
2. Beebe, D.J., et al., *Functional hydrogel structures for autonomous flow control inside microfluidic channels*. Nature, 2000. **404**(6778): p. 588-590.

3. Dong, L., et al., *Adaptive liquid microlenses activated by stimuli-responsive hydrogels*. Nature, 2006. **442**(7102): p. 551-554.
4. Sidorenko, A., et al., *Reversible Switching of Hydrogel-Actuated Nanostructures into Complex Micropatterns*. Science, 2007. **315**(5811): p. 487-490.
5. Lendlein, A., et al., *Light-induced shape-memory polymers*. Nature, 2005. **434**(7035): p. 879-882.
6. Tanaka, T., et al., *Collapse of Gels in an Electric Field*. Science, 1982. **218**: p. 467-469.
7. Miyata, T., N. Asami, and T. Uragami, *A reversibly antigen-responsive hydrogel*. Nature, 1999. **399**(6738): p. 766-769.
8. Forterre, Y., et al., *How the Venus flytrap snaps*. Nature, 2005. **433**(7024): p. 421-425.
9. Skotheim, J.M. and L. Mahadevan, *Physical Limits and Design Principles for Plant and Fungal Movements*. Science, 2005. **308**(5726): p. 1308-1310.
10. Lee, H., C. Xia, and N.X. Fang, *First jump of microgel; actuation speed enhancement by elastic instability*. Soft Matter, 2010. **6**(18): p. 4342.
11. Tanaka, T. and D.J. Fillmore, *Kinetics of Swelling of Gels*. Journal of Chemical Physics, 1979. **70**(3): p. 1214-1218.
12. Hong, W., et al., *A theory of coupled diffusion and large deformation in polymeric gels*. Journal of the Mechanics and Physics of Solids, 2008. **56**(5): p. 1779-1793.
13. Cao, X., S. Lai, and L. James Lee, *Design of a Self-Regulated Drug Delivery Device*. Biomedical Microdevices, 2001. **3**(2): p. 109-118.

14. Edwards, J., et al., *Botany: A record-breaking pollen catapult*. Nature, 2005. **435**(7039): p. 164-164.
15. Pickard, B.G., *Action Potentials in Higher Plants*. Botanical Review, 1973. **39**: p. 172-201.
16. Sun, C., et al., *Projection micro-stereolithography using digital micro-mirror dynamic mask*. Sensors and Actuators A: Physical, 2005. **121**(1): p. 113-120.
17. Holmes, D.P. and A.J. Crosby, *Snapping Surfaces*. Advanced Materials, 2007. **19**(21): p. 3589-3593.
18. Borno, R.T., J.D. Steinmeyer, and M.M. Maharbiz, *Transpiration actuation: the design, fabrication and characterization of biomimetic microactuators driven by the surface tension of water*. Journal of Micromechanics and Microengineering, 2006. **16**(11): p. 2375-2383.
19. Madden, J.D., *Mobile Robots: Motor Challenges and Materials Solutions*. Science, 2007. **318**(5853): p. 1094-1097.

5. PATTERN TRANSFORMATION USING SWELLING-INDUCED BUCKLING INSTABILITY

5.1 INTRODUCTION

Buckling instability has been studied extensively for the last few decades as one of the most critical structural failure modes [1]. This conventional theme is recently gaining new attention as a useful way for creation and transformation of patterns because buckling is often accompanied with large deformation and radical shape change of the structure. Nature has already developed such techniques to leverage mechanical instability to create a wealth of complex patterns. As biological tissues and organisms grow non-uniformly or under constraints, plane features transform into rich patterns with complexity as found in such examples as wavy edges of plant leaves [2], fine annular patterns in fingerprints [3, 4], and inter-connected creases of brain cortex [5].

This elegant approach to achieve pattern transformation by harnessing mechanical instability has not been much explored with artificial materials and man-made structures until recent progress in material science and manufacturing technologies for soft materials such as elastomers and hydrogels. Particularly, swelling gels have attracted increasing interest because they can actively grow and shrink depending on environmental conditions such as humidity, temperature, and pH [6-8]. Hydrogel-based structures, therefore, can spontaneously create and reversibly pose different patterns via buckling without the need for external load to trigger mechanical instability. This holds

great potential to provide new opportunities in development of self-operating devices with switchable functionalities, in biomedical engineering where creation of physiologically relevant environment is crucial, or in the study of morphogenesis of tissues and organs in biology, to name a few.

Recently, simple geometries of hydrogel systems have been investigated in this context. Wrinkle formation of swelling thin film and gel strips confined on a hard substrate has been demonstrated [9-12]. Pattern transformation of periodic pores in polymer film governed by swelling-induced elastic instability has been investigated for its potential application as tunable photonic crystal [13]. Other geometries such as annular disk have been also studied [14]. Taking advantage of buckling for pattern formation, however, has not been extended to more diverse shapes and geometries to further explore inspirations from nature where a plethora of stunning features are found. Of particular interest in our study is tubular structure with circumferential wrinkles, which holds crucial physiological significance as well as its own geometrical importance. For example, wrinkled airway of asthmatic bronchiole results from the swollen inner cell layer. Hence, their topology and corresponding mechanical condition are key factors to better understand the physiological circumstances that diseased cells experience and to develop improved treatment for this chronic disease [15, 16]. Although numerical and theoretical studies on non-planar geometries such as tube and sphere have been reported [17, 18], few have been able to create soft tubular structure with well controlled dimensions and constraints due primarily to lack of 3D fabrication technology for

hydrogels. It has been even more challenging to reproduce complex patterns emerging in such structures.

This chapter presents well-controlled pattern transformation of tubular-shaped microgels using swelling-induced circumferential buckling and mechanism behind the pattern formation is explained by simple energy analysis. 3D micro-fabrication technology, projection micro-stereolithography (PuSL) [19], was employed to construct tubular hydrogel micro-structures, the bottom end of which is fixed to impose constraints against swelling as shown in Figure 5.1. Characteristic dimensional parameters, t , h , and D represent thickness, height, and diameter of the model structure in dry state, respectively. With the fixed boundary condition on the bottom, gel develops nonhomogeneous stress when allowed to swell. Depending on dimension, constrained

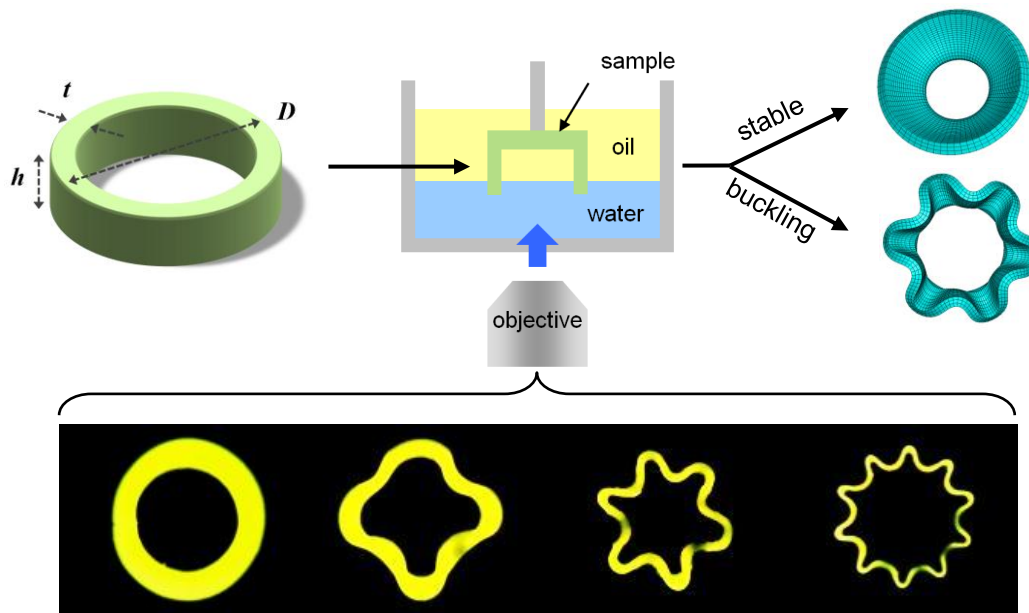


Figure 5.1 Constrained swelling of gel tube leads to buckling instability, transforming the circular shape into wrinkled patterns with different wave numbers depending on dimension

swelling gives rise to buckling instability, causing the circular wall to transform into wrinkled patterns with different wave numbers as shown in Figure 5.1. An analytical model developed here using elastic energy predicts that stability of the system depends on $(t/h)^2$, and swelling ratio λ , and that instability patterns are determined by and only by h/D . Based on the theory, a series of samples with different dimensions were designed and fabricated. The original circular shape was transformed into wavy circumferential buckling patterns in our swelling experiment and the number of waves in buckled configurations agreed well with the theoretical prediction. Numerical simulation using ABAQUS also showed close relationship between geometric parameters and resulting buckling patterns. It is expected that this study on buckling of swelling gels will not only help us better understand the mechanics of soft materials, but it will also contribute to increasing the breadth of possible application in many emerging fields where complex morphologies and dramatic pattern shift are of critical importance, such as tissue engineering and tunable photonic/phononic band gap materials.

5.2 THEORY

The model system in our study is a cylindrical-walled hydrogel tube as shown in Figure 5.2. Diameter, height, and wall thickness of the tube are denoted as D , h , and t , respectively. Cylindrical coordinate system (r, θ, z) is used to describe deformation. The base of the tube is fixed to the substrate, whereas the rest of the structure is free to swell. When allowed to swell without any constraint, length-wise equilibrium swelling ratio is λ . It is assumed that the whole structure first swells to the fully swollen state and then the

bottom end is forced to fit into its original dry dimension. Therefore, fully swollen state is considered as stress-free and zero energy state and any deformation from it increases elastic energy of the system. The system poses a shape that minimizes the total potential energy. With the given boundary condition, there are two possible configurations for the swollen tube to adopt in order to accommodate expanded geometry in the original dimension; compression or buckling as illustrated in Figure 5.1. For compressed configuration in which the structure stays stable, the cross-section of the tube remains circular with the radius varying with height. Therefore, increase in potential energy results solely from the in-plane compression of the structure. On the other hand, situation is not as simple in buckled configuration where wrinkled wall undergoes bending in both circumferential and axial direction. The elastic energy for both configurations are analyzed to predict stability as well as post-buckling pattern for unstable cases.

5.2.1 STABLE CONFIGURATION

For stable configuration, cross-section of the tube remains circular with the radius being a function of height only. It is assumed that radius is linearly varying from the dry radius, R ($=D/2$), at the fixed bottom to the fully swollen radius, λR , at the top as shown in Figure 5.2a. Then, radius can be written as

$$r = r(z) = R \left(1 + (\lambda - 1) \cdot \frac{z}{h} \right) \quad (5.1)$$

Since only in-plane compression is involved, total elastic energy in the stable configuration is obtained as

$$U_{stable} = \int \frac{1}{2} E \varepsilon_{\theta\theta}^2 dV = \frac{1}{24} \pi E D t h \cdot b(\lambda) \quad (5.2)$$

where $\varepsilon_{\theta\theta}(z) = \frac{r - \lambda R}{\lambda R} = -(1 - \frac{1}{\lambda})(1 - \frac{z}{h})$ is strain in circumferential direction and

$$b(\lambda) = (1 - \frac{1}{\lambda})^2 (3 + \lambda).$$

5.2.2 BUCKLED CONFIGURATION

Once the structure becomes mechanically unstable, it buckles creating wrinkles along its circumference. In this configuration, swollen length fits into confined geometry by posing wavy shape at cost of elastic energy as shown in Figure 5.2b. If this were the only energy penalty, buckling pattern would always be the lowest possible mode because lower mode is energetically more favorable. On the other hand, the wall is fixed on the bottom, which confines the wall elastically. Hence, the tube wall deflects outwards or inwards depending on the position on the wave with the distance as large as the wave amplitude. Larger wave amplitude results in more deflection, thus requiring higher elastic energy. In general, given overall wave arclength, wave amplitude is inversely proportional to the number of waves. Thus, higher mode having smaller wave amplitude

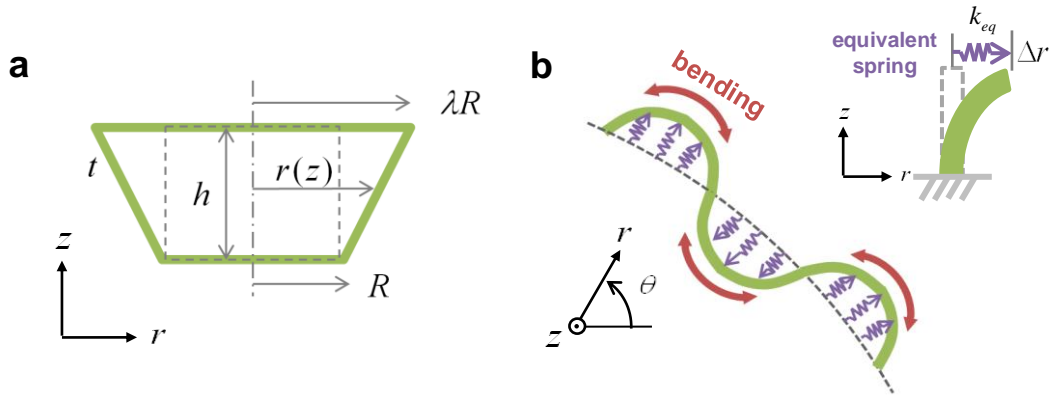


Figure 5.2 Model geometry (a) compressed configuration – side view (b) buckled configuration – top view

is energetically favorable in this perspective. Therefore, with the two energy contributions working together, there exists an optimum mode that gives minimum total potential energy.

Assuming that wavy pattern follows sinusoidal function along the circumference, amplitude of sinusoidal wave for given arclength can be inversely calculated and obtained in a closed form using approximation for the elliptic integral [20]. Radius of wrinkled cross-section can be written as

$$r(\theta, z) = R \left\{ 1 + \frac{2}{n} a(\lambda) \cos n\theta \cdot \frac{z}{h} \right\} \quad (5.3)$$

where n is a number of waves along the circumference and $a(\lambda) = \sqrt{\left(\frac{2}{3-\lambda}\right)^2 - 1}$ (see

Appendix A for derivation). Here, it is again assumed that wave amplitude varies linearly

with height to be consistent with fixed boundary condition on the bottom. Elastic energy from bending of the wrinkled wall is obtained by [21]

$$U_{bending} = \frac{1}{2} \int EI \kappa^2 dV = \frac{\pi E t^3 a^2(\lambda) h}{9D} n^2 \quad (5.4)$$

where, $I = \frac{t^3 R d\theta}{12}$ and $\kappa \approx \frac{1}{R^2} \frac{\partial^2 r(\theta, z)}{\partial \theta^2}$ are bending moment of inertia and curvature of the wave. Note that energy is proportional to n^2 , which means that lower mode is energetically favorable.

Next, elastic energy due to the confinement on the substrate is considered. For simplicity, equivalent springs for cantilevers are introduced to model elastic confinement which connect each point on the top circumference of the tube to the confined base as shown in Figure 5.2b. Then each spring undergoes stretching by the distance to the neutral circumferential line, which is the wave amplitude at each point, $\Delta r = r(\theta; z = h) - R$. From beam theory, equivalent spring constant of infinitesimal segment of the wall is given by [1]

$$k_{eq} = \frac{E t^3 R d\theta}{4h^3} \quad (5.5)$$

Energy due to the elastic confinement is therefore obtained as

$$U_{conf} = \int \frac{1}{2} k_{eq} (\Delta r)^2 = \frac{\pi E t^3 D^3 a^2 (\lambda)}{16 h^3} \cdot \frac{1}{n^2} \quad (5.6)$$

Note that the energy in this case is inversely proportional to n^2 , which means that higher mode is energetically favorable.

From equation (5.4) and (5.6), total elastic energy for buckled configuration, therefore, is given by

$$U_{unstable} = U_{bending} + U_{conf} = \frac{\pi E t^3 h a^2 (\lambda)}{9 D} \left[n^2 + \frac{9}{16 (h/D)^4} \cdot \frac{1}{n^2} \right] \quad (5.7)$$

Compression in buckled configuration, especially close to the bottom confinement is neglected for the sake of simplicity. It is important to note that two terms are proportional to n^2 and $1/n^2$, respectively. The former is from bending (lower energy for lower mode) and the latter is from confinement (lower energy for higher mode).

5.2.3 BUCKLING MODE

It is found that the opposite dependence on mode number of two different energy contributions involved in equation (5.7) brings the system to a certain buckling mode in the event of buckling. Moreover, it is interesting to note that parameters involved in this competition are h and D only. In other words, other factors such as thickness, swelling ratio, and elastic modulus of the structure have no influence in the formation of instability pattern. Figure 5.3a plots total energy level for each buckling mode for different h/D ratio.

As it shows, one can find an optimum mode number \tilde{n} at the lowest energy point and this number varies depending on h/D of the sample. The smaller the h/D is, the higher the optimum mode number is, resulting in more wrinkling in instability pattern. Figure 5.3b plots the total potential energy for different possible buckling modes as a function of h/D . This clearly shows the mode that gives the lowest elastic energy for different h/D as plotted in dotted line, suggesting consequent buckling patterns for given dimension. The

buckling mode number, \tilde{n} , can be analytically obtained by $\frac{\partial U_{tot}}{\partial n} = 0$, and is expressed

in terms of dimensional parameters as

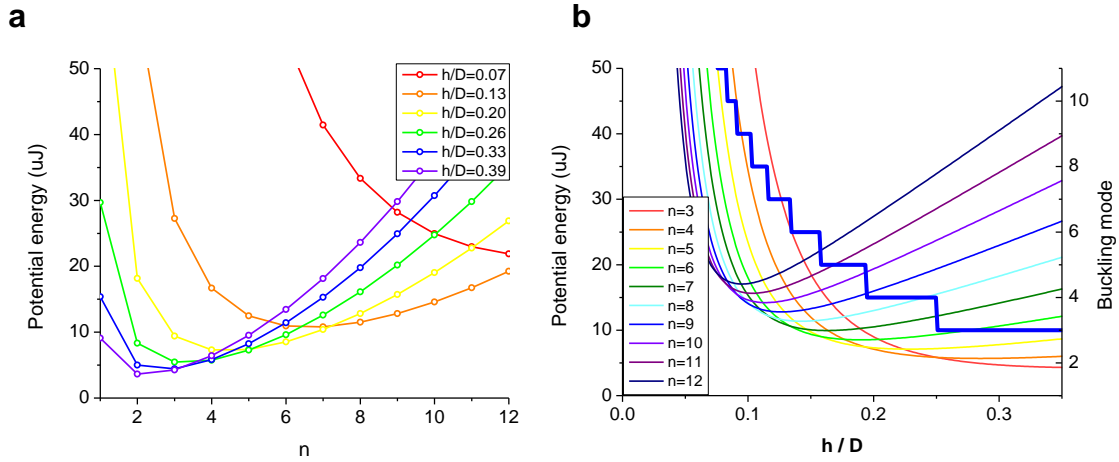


Figure 5.3 (a) Potential energy for different h/D . The optimum mode of the lowest energy varies with h/D . (b) Potential energy for different buckling mode. Minimum energy mode varies with h/D , resulting in different buckling patterns.

$$\tilde{n} = \frac{\sqrt{3}}{(h/R)} = \frac{1.732}{(h/R)} \quad (5.8)$$

Corresponding wave length can be obtained as

$$\tilde{\lambda} = \frac{2\pi R}{\tilde{n}} = 3.628 \cdot h \quad (5.9)$$

It shows that buckling wave length depends only on the wall height h , which agrees very well with the previous result found in the literature ($\lambda = 3.256h$) [14].

Elastic energy for the optimum buckling mode is given by

$$U_{unstable}|_{n=\tilde{n}} = \frac{\pi E t^3 h a^2(\lambda)}{9D} \left[\tilde{n}^2 + \frac{9}{16(h/D)^4} \cdot \frac{1}{\tilde{n}^2} \right] = \frac{1}{6} \pi E t^3 D \frac{1}{h} \cdot a^2(\lambda) \quad (5.10)$$

5.2.4 STABILITY

Now stability criteria is considered. Between circular (stable) and buckled (unstable) state, the system chooses the configuration at the lower energy level.

Instability index is defined as follows using equation (5.1) and (5.10) to characterize relative magnitude of the energy levels.

$$\gamma = \frac{U_{stable}}{U_{unstable}} = \frac{1}{(t/h)^2} \cdot c(\lambda) \quad (5.11)$$

where $c(\lambda) = \frac{1}{4} \frac{(1-\frac{1}{\lambda})^2(3+\lambda)}{\left(\frac{2}{3-\lambda}\right)^2 - 1}$ is a function of swelling ratio λ only. $\gamma > 1$ means

$U_{stable} > U_{unstable}$, thus the system tends to buckle, while $\gamma < 1$ means $U_{stable} < U_{unstable}$,

thus the system remains stable. It implies that stability is determined by the square of the

aspect ratio of tube wall, $\left(\frac{t}{h}\right)^2$, and swelling ratio λ . This also matches well with the

result found in the literature ($\lambda_{cr} = 0.867 \frac{t^2}{h^2}$) [14]. λ_{cr} required for the onset of buckling

instability is calculated and plotted as a function of the wall aspect ratio t/h in Figure 5.4,

suggesting that slender walled tube becomes mechanically unstable at smaller swelling ratio.

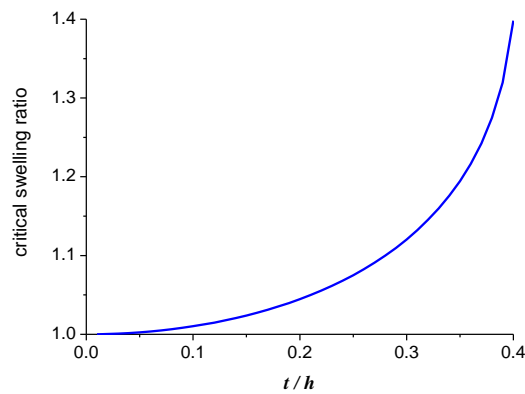


Figure 5.4 Critical swelling ratio for mechanical instability as a function of the wall aspect ratio t/h .

5.3 EXPERIMENT

In this study, Poly(ethylene glycol) diacrylate (PEGDA) hydrogel was used. Porous PEGDA was synthesized by mixing PEGDA (MW575, Sigma Aldrich) with PEG (MW200, Sigma Aldrich) in a weight ratio of 1:3, followed by addition of 0.5% wt. of photo-initiator (phenylbis(2,4,6-trimethylbenzoyl) phosphine oxide, Sigma Aldrich) for photopolymerization under ultraviolet (UV) illumination (wavelength: 405nm). Not being polymerized, PEG contributes to reducing crosslinking density by occupying intermolecular space between PEGDA during photo-polymerization, resulting in low modulus and large swelling ratio. Diameter of hydrogel disks in dry state and fully swollen state in de-ionized (DI) water was measured to obtain equilibrium swelling ratio λ_{eq} . Length-wise swelling ratio of each hydrogel in equilibrium swelling state were 1.75. Elastic modulus in swollen state was 0.11 MPa. This hydrogel dramatically changes optical property from transparent to opaque as it swells, which facilitates visualization of the shape of the swollen sample in experiment.

Projection micro-stereolithography (P μ SL) were used to fabricate 3D hydrogel tube samples. P μ SL is a digital freeform microfabrication technology capable of fabricating complex shaped 3D micro architectures by using a spatial light modulator and an ultraviolet (UV) light emitting diode coupled to a projection lens system to convert liquid monomer to solid polymer in an additive, layer-by-layer fashion [19]. Therefore, tube designs with different geometries and dimensions created by CAD software can be rapidly fabricated into actual samples. After fabrication, samples were rinsed in acetone for 2 hours to wash out uncured PEG in the structure. Then samples were allowed to dry

in a vacuumed desiccator for 30 minutes, so acetone can evaporate out. For swelling experiment, a sample was placed upside down and put in the bath with DI water covered with oil layer on top as illustrated in Figure 5.1. Then the sample was lowered and brought into contact with DI water surface for swelling, while base substrate part of the sample stayed in the top oil layer. In this way, only tube part can swell by DI water while their base was still fixed in the confined dimension. The entire swelling process was monitored through an objective lens and recorded by CCD camera attached to it.

As discussed above, stability of the swelling tube depends on t/h and λ , and buckling pattern is determined only by h/D . This can be described together in the stability map shown in Figure 5.5a. With the horizontal and vertical axes representing h/D and t/D , respectively, any tube geometries can be mapped onto this plot. For given equilibrium swelling ratio λ , corresponding wall aspect ratio t/h that meets the critical condition for instability, $\gamma = 1$, can be represented by a straight line drawn from the origin. The area under this line is unstable region where $\gamma > 1$, hence buckling is expected upon swelling for samples falling in this region. The slope of this line increases with λ , making the unstable region larger. Furthermore, since buckling pattern relies only on h/D , one can expect the buckling mode number based on the position of the sample on this map. Therefore, stability of the swelling gel tube as well as buckling pattern can be predicted together by mapping the dimensions onto the stability map.

To demonstrate control over pattern production, tube samples in different dimensions were designed based on the stability map as shown in Figure 5.5a. The stability line was drawn for $\lambda = 1.5$. Samples on the same sloped line have the same

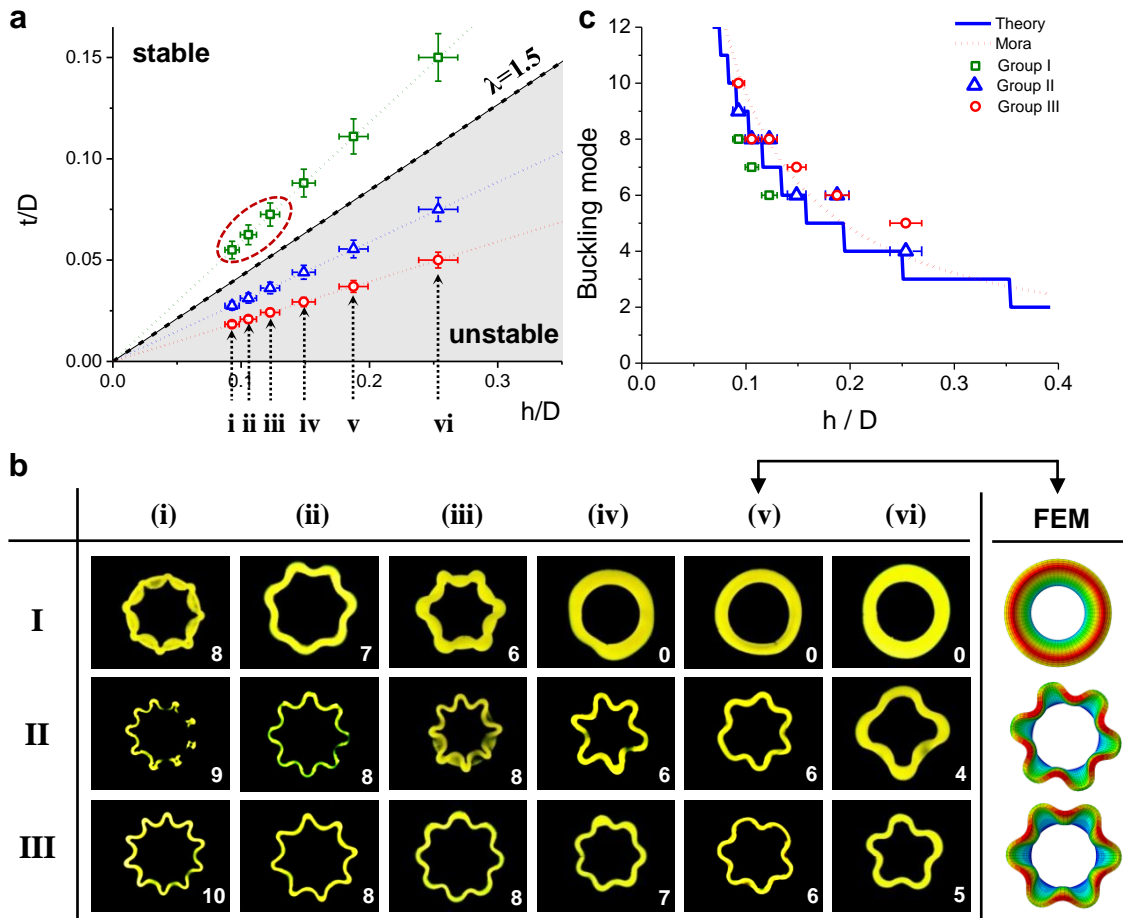


Figure 5.5 (a) Stability map. Critical t/h line for $\lambda=1.5$ divides upper stable region and shaded unstable region below. Samples are grouped into three groups (I-III) by t/h for stability and into six groups (i-vi) by h/D for buckling pattern. (b) Patterns formed in swelling experiment. Samples in the same row have the same t/h , thus showing the same stability behavior, except for I-(i), (ii), and (iii). Samples in the same column have the same h/D , thus forming patterns with close wave numbers once becoming unstable. FEM simulation result for the group (v) is also presented showing good agreement with experiment. (c) Buckling mode number from unstable samples from experiment. They match well with the prediction by the present theory as well as the linear elasticity model from the literature [14].

instability index. Instability indices defined by equation (5.11) for each line are 0.46, 1.85, and 4.16, respectively, which means that the first group above the stability line should remain stable while the other two groups below the stability line are expected to buckle. On the other hand, samples aligned on the same vertical line should transform into the same buckling pattern regardless of t because they have the same h/D .

Figure 5.5b presents representative patterns obtained in the experiment from different groups. Although some samples in group I became unstable and posed buckled configuration, samples in group I tend to remain stable during swelling, while samples in group II and group III underwent mechanical instability and transformed into wrinkled patterns. Moreover, despite different wall aspect ratio t/h across samples in group II and group III, resulting buckling patterns from samples with the same h/D were close to each other as our theory suggests. This result also shows close agreement with finite element method (FEM) simulation by ABAQUS. A set of representative results is shown in Figure 5.5b. The present results for buckling mode numbers are shown in Figure 5.5c. Instability patterns from samples with a wide range of dimension collapse well around theoretical prediction, validating the theory that only h/D matters for buckling pattern formation. This demonstrated full control over the pattern of gel tubes formed by mechanical instability.

5.4 SUMMARY

In summary, this chapter presented well-controlled wrinkle formation of confined hydrogel tube using swelling-induced circumferential buckling. A simple theory based on

elastic energy has also been developed to find that key dimensional parameters sensitive to stability and buckling pattern formation are thickness to height ratio and height to diameter ratio, respectively. Our experimental results showed good quantitative agreement with theoretical prediction as well as FEM simulation. In this study, it has been demonstrated that to make use of mechanical instability of hydrogel is a simple method for spontaneous formation of complex patterns. Furthermore, reversible nature of swelling and shrinking of hydrogel offers unique opportunities to develop versatile devices with tunable properties. The study on buckling of swelling gels will contribute to increasing the breadth of possible application in many emerging fields where complex morphologies and dramatic pattern shift are of critical importance, such as tissue engineering and tunable photonic/phononic band gap materials.

5.5 REFERENCES

1. Shames, I.H., *Introduction to Solid Mechanics*. 2nd ed. 1989, Upper Saddle River: Prentice-Hall, Inc.
2. Sharon, E., M. Marder, and H.L. Swinney, *Leaves Flowers and Garbage Bags: Making Waves*. *American Scientist*, 2004. **92**: p. 254-261.
3. Kücken, M. and A.C. Newell, *Fingerprint formation*. *Journal of Theoretical Biology*, 2005. **235**(1): p. 71-83.
4. Liang, H. and L. Mahadevan, *The shape of a long leaf*. *Proceedings of the National Academy of Sciences*, 2009. **106**(52): p. 22049-22054.

5. Bayer, S.A. and J. Altman, *The human brain during the second trimester*. 2005, Boca Raton: Taylor & Francis
6. Sidorenko, A., et al., *Reversible Switching of Hydrogel-Actuated Nanostructures into Complex Micropatterns*. *Science*, 2007. **315**(5811): p. 487-490.
7. Dong, L., et al., *Adaptive liquid microlenses activated by stimuli-responsive hydrogels*. *Nature*, 2006. **442**(7102): p. 551-554.
8. Beebe, D.J., et al., *Functional hydrogel structures for autonomous flow control inside microfluidic channels*. *Nature*, 2000. **404**(6778): p. 588-590.
9. Breid, D. and A.J. Crosby, *Effect of stress state on wrinkle morphology*. *Soft Matter*, 2011. **7**(9): p. 4490.
10. Chan, E.P. and A.J. Crosby, *Fabricating Microlens Arrays by Surface Wrinkling*. *Advanced Materials*, 2006. **18**(24): p. 3238-3242.
11. Trujillo, V., J. Kim, and R.C. Hayward, *Creasing instability of surface-attached hydrogels*. *Soft Matter*, 2008. **4**(3): p. 564.
12. DuPont Jr, S.J., et al., *Swelling-induced instabilities in microscale, surface-confined poly(N-isopropylacrylamide) hydrogels*. *Soft Matter*, 2010. **6**(16): p. 3876.
13. Jang, J.-H., et al., *Combining Pattern Instability and Shape-Memory Hysteresis for Phononic Switching*. *Nano Letters*, 2009. **9**(5): p. 2113-2119.
14. Mora, T. and A. Boudaoud, *Buckling of swelling gels*. *The European Physical Journal E*, 2006. **20**(2): p. 119-124.

15. James, A.L., P.D. Pare, and J.C. Hogg, *The Mechanics of Airway Narrowing in Asthma*. The American review of respiratory disease, 1989. **139**(1): p. 242-246.
16. Redington, A.E., *Airway wall remodelling in asthma*. Thorax, 1997. **52**(4): p. 310-312.
17. Moulton, D.E. and A. Goriely, *Circumferential buckling instability of a growing cylindrical tube*. Journal of the Mechanics and Physics of Solids, 2011. **59**(3): p. 525-537.
18. Li, B., et al., *Surface Wrinkling Patterns on a Core-Shell Soft Sphere*. Physical Review Letters, 2011. **106**(23).
19. Sun, C., et al., *Projection micro-stereolithography using digital micro-mirror dynamic mask*. Sensors and Actuators A: Physical, 2005. **121**(1): p. 113-120.
20. Luke, Y.L., *Approximations for Elliptic Integrals*. Mathematics of Computation, 1968. **22**: p. 627-634.
21. Landau, L.D., *Theory of Elasticity*. 1986, Oxford, New York: Pergamon Press.

6. NON-FICKIAN SOLVENT DIFFUSION COUPLED WITH LARGE DEFORMATION OF SWELLING GELS

6.1 INTRODUCTION

Hydrogel is a network of polymer chains which allows the diffusion of solvent in the network. Upon solvent absorption, hydrogel undergoes substantial volumetric change. This unique process has become increasingly important in many applications ranging from micro-actuators [1] to tissue engineering [2] to drug delivery [3, 4]. Response time of hydrogel swelling is very important in many applications, particularly in three dimensional (3D) active hydrogel structures driven by swelling demonstrated in previous chapters. In such devices, embedded microfluidic channels in the device deliver solvent directly to specific locations for local swelling control. Therefore, complex 3D motion of the micro device is enabled by appropriate selection of the distribution of capillary network [5, 6], unlike other hydrogel actuators where actuation relies mostly on simple expansion and shrinkage of the whole device [1, 7]. As the dynamic behavior of hydrogel is controlled by the diffusion of the solvent into the polymeric network, a rigorous study for solvent migration into glassy polymer and associated swelling deformation is critical to understand and exploit this new class of micro actuation.

There have been many efforts to develop a rigorous framework to describe the coupled large deformation and diffusion in gels [8-11]. However, for most glassy polymers, physical situation is even more complex. At temperatures far above T_g (glass

transition temperature), the diffusion follows Fick's law, where the flux increases linearly with the gradient of solvent concentration. However, near or below T_g , more complicated non-Fickian behavior is observed. One particular instance of non-Fickian diffusion is called Case II diffusion which is characterized by a sharp diffusion front that separates the swollen rubbery part and the dry glassy part of the polymer [12]. A meaningful mechanism to explain the Case II diffusion is the competition between the rate of relaxation of the polymeric network and the diffusion of solvent [13]. Because of the complexities including moving sharp interface between dry (glassy) and wet (rubbery) regions and strong coupling between solvent migration and large amplitude of deformation of gel, the coupled Case II diffusion and large deformation has not been fully explained by a mathematical model [9].

Diffusion experiment on PEG-DA hydrogel which drives the microactuators presented in previous chapters also shows Case II diffusional behavior when the solvent migrates into hydrogel. Crosslinking density of PEG-DA gel was controlled in such a way that the gel not only expands in volume upon swelling, but its optical property also changes. The gel which is transparent in dry state becomes white and opaque when it gets wet, facilitating the visual distinction between dry and wet area. The PEG-DA rod was brought into contact with DI water, while evolution of diffusion interface along the axial direction of the rod was monitored. Figure 6.1 apparently shows the sharp front which indicates a typical feature of Case II diffusion.

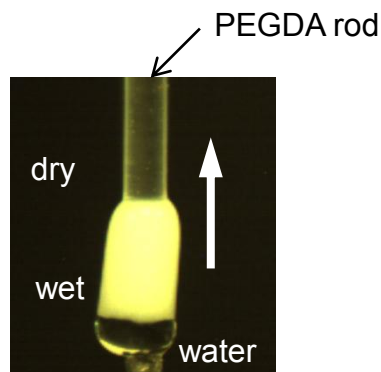


Figure 6.1 Water diffusion experiment on a PEGDA rod. Transparent polymer becomes white when it gets wet. A sharp boundary separating dry and wet region is clearly observed, indicating Case II diffusion characteristics.

Therefore, development of mathematical model to capture dynamic behavior of glassy polymer subjected to solvent migration is important to understand underlying actuation principle of the hydrogel devices. To this end, this chapter presents experimental techniques to quantitatively analyse diffusional behavior of solvent into glassy polymer and to identify and characterize parameters necessary for a mechanics model for Case II diffusion coupled with large deformation of the network. The model is validated by comparing with experiments.

6.2 DIFFUSION EXPERIMENT

6.2.1 MATERIAL SYNTHESIS

Porous PEG-DA hydrogel was synthesized by mixing PEG-DA prepolymer (MW575, Sigma Aldrich) with PEG (MW200, Sigma Aldrich) in a weight ratio of 1:3 followed by addition of 0.5% wt. of photo-initiator (phenylbis(2,4,6-trimethylbenzoyl)

phosphine oxide, Sigma Aldrich) for photo-polymerization under UV illumination ($\lambda=365\text{nm}$). Not being polymerized, PEG contributes to reducing crosslinking density by occupying intermolecular space between PEG-DA during photo-polymerization, resulting in low modulus and large swelling ratio.

6.2.2 ONE DIMENSIONAL DIFFUSION EXPERIMENT ON A GEL ROD

One dimensional (1D) diffusion experiment was carried out on a gel rod. Although a gel rod swells in radial direction as well, 3D effect of shear stress and lateral swelling can be negligible because of high aspect ratio to highlight the diffusion and swelling in axial direction. Water diffusion and associated swelling of the gel rod was quantified by directly measuring diffusion front propagation and swelling length. In Case II diffusion, there is always a sharp boundary between dry and wet regions because diffusion is limited by slow mechanical relaxation of polymer. The gel rod was brought in contact with a water droplet on the tip. Water droplet size was controlled by syringe pump in such a way that the size of water droplet was kept large enough to supply enough amount of water for swelling at all time and that, at the same time, droplet was small enough so water does not make any contact with the side wall of the gel. Water started to diffuse into the polymer network, creating a visible boundary indicating the location of diffusion front. This experiment was carried out in oil bath to prevent possible evaporation of water through the side wall of the wet part, ensuring that solvent migration is primarily in the direction along the axis only without any loss of flux. The location of the diffusion front and the tip of the rod were measured by a digital camera over the

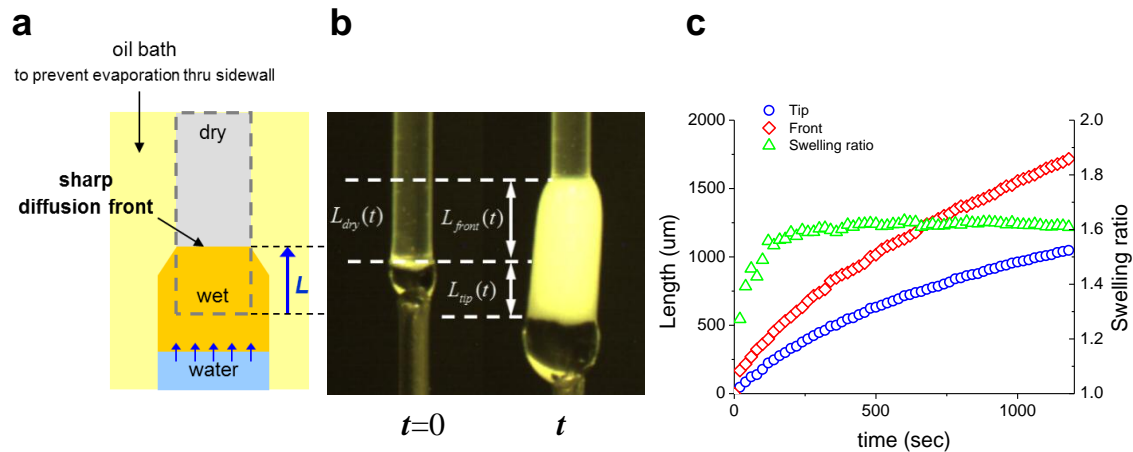


Figure 6.2 One dimensional diffusion experiment on a gel rod. (a) experimental setup (b) micrographs of the sample during experiment (c) data collected from the experiment

course of diffusion process. The result is shown in Figure 6.2c. Although diffusion is initially not at constant propagation speed, tip growth and diffusion front propagation settle in a linear regime in later stage of the experiment. It is highly possible that abnormal diffusion behavior in the beginning of the experiment comes from lateral swelling of the rod. Although the rod is considered as 1D system here, hydrogel physically swells isotropically. Therefore, in the very beginning of the swelling experiment when the effect from lateral expansion is not negligible compared to axial expansion, 1D approximation does not hold. In later stage, when axial swelling length became relatively larger than lateral swelling length, diffusion front propagates at constant speed, showing Case II diffusion characteristics. This regime can be also identified by looking at the region where swelling ratio behind the diffusion front is constant ($t > 1000$ s), which is another unique feature of Case II diffusion. In this stage, diffusion front propagation speed was about $0.7 \mu\text{m/s}$. This 1D diffusion experimental

result is compared with simulation result to validate the mechanism model later in this chapter.

6.2.3 EFFECT OF MECHANICAL CONSTRAINT ON DIFFUSION

Solvent migration in polymeric network is highly influenced by the microenvironment where solvent molecules are situated. To be more specific, diffusivity is strongly depending on the intermolecular structure between polymer crosslinking sites. More densely packed polymer chains hinder solvent molecule transport, resulting in low solvent diffusivity. Presence of mechanical stress prevents or promotes swelling expansion by mechanically compressing or relaxing polymer network, which can entirely change the diffusional behavior. To study the effect of mechanical constraint, two gel rods under different mechanical conditions were tested. One was allowed to swell freely in space (Figure 6.3a), whereas the other was confined in tightly fitted glass tube when solvent was applied (Figure 6.3b). Oil layer between the gel rod and the glass tube worked as lubricant, minimizing the effect of frictional shear stress. Diameter of both gel rods are 1.6 mm. As you can see from the result, the free swelling rod displayed Case II diffusion behavior, forming sharp diffusion interface and swelling ratio plateau. However, diffusion front in confined swelling was not as obvious as in free swelling. Also, swelling ratio behind the diffusion front increased with time, suggesting that substantial concentration gradient existed in the wet region. This is more like Fickian diffusion. More apparent difference was observed in diffusion front propagation speed, which was 0.69 $\mu\text{m/s}$ in free swelling, whereas 0.06 $\mu\text{m/s}$ in confined swelling, respectively. It is interesting to observe that diffusion speed of the same solvent in the same hydrogel

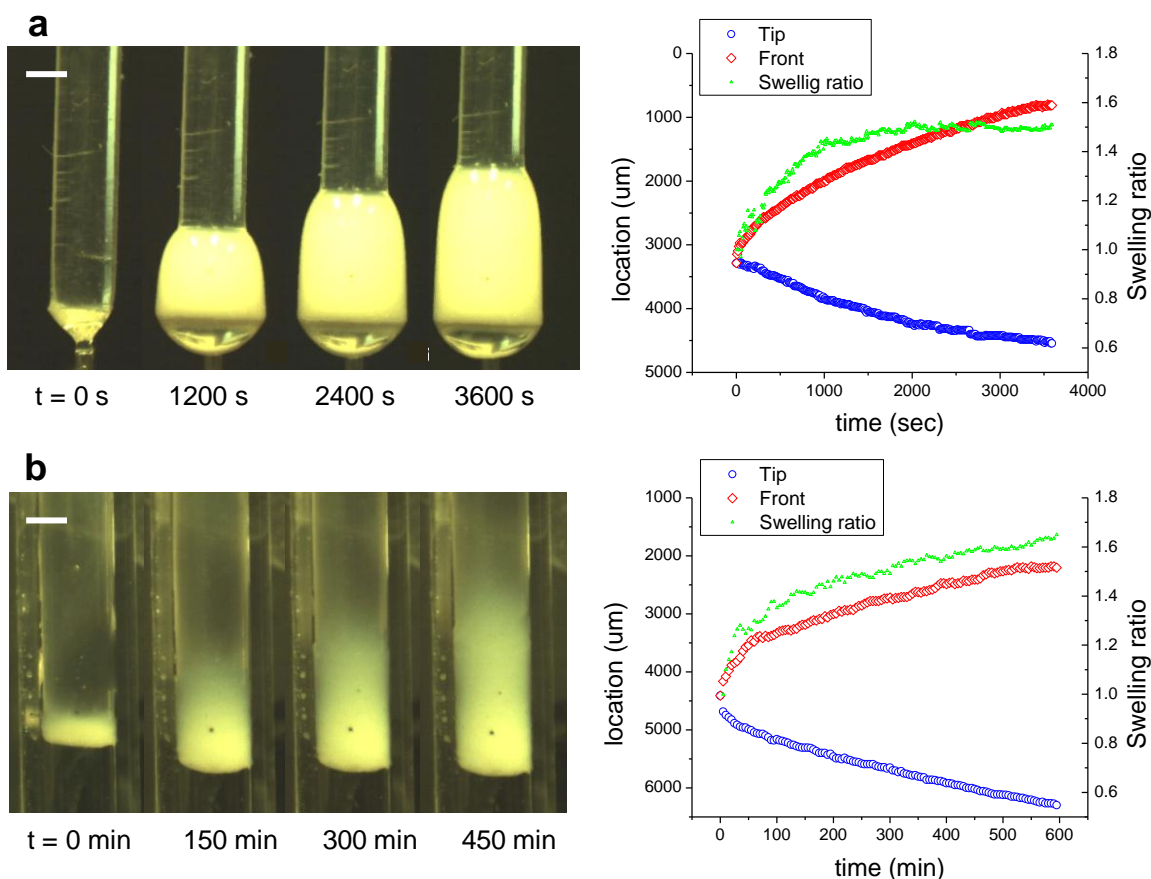


Figure 6.3 Diffusion experiments on a free swelling rod (a) and a rod swelling in a confined glass tube (b). scale bars indicate 1mm.

differs by an order of magnitude depending on the mechanical circumstance. This demonstrates that diffusion kinetics and elastic response of the gel is highly connected and emphasizes that it is important to quantify solvent transport as a function of polymer network expansion, which is covered later in this chapter.

6.2.3.1 Effect of rod diameter on diffusion

A PEGDA rod is used as one dimensional system to study swelling and diffusion. However, as gel swells in all directions 3D effect is not negligible especially in the beginning of the diffusion experiment when aspect ratio of swollen region is not yet high.

To see how rod diameter affects diffusion and swelling, three gel rods with different diameter were tested. Diameter of each rod was 1.1mm, 1.5mm, and 2.15mm, respectively, and their length-wise swelling ratio is all 1.6. Figure 6.4 shows the result from all experiment plotted together for comparison. Diffusion trends were all the same, but the diffusion in thickest rod is slightly slower than the thinner two. This might be attributed to that the amplitude of shear stress that diffusion front has to overcome at the dry-wet interface is greater in the thick rod. Therefore, 3D effect is relatively more significant for the thick rod. This is also consistent with the observation from the swelling ratio trend. Appearance of swelling plateau, which can be an indicator of the beginning of the 1D Case II diffusion regime, is earlier for the thin rod and later for thick rod. This means that diffusion in thick rod suffered longer from 3D effect. Collectively, the result suggests that thinner rod is better for one dimensional diffusion experiment. Rods with diameter from 500 μ m to 1mm can be considered good for 1D diffusion experiment for practical issues such as structural integrity and handling.

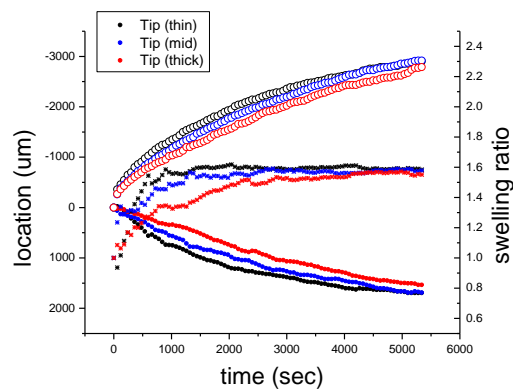


Figure 6.4 1D diffusion experiment on gel rods with different diameter

6.2.4 ONE DIMENSIONAL DIFFUSION EXPERIMENT ON A SPHERICAL GEL

Sphere is a perfect geometry to study one dimensional diffusion and swelling. Although swelling is still physically a three dimensional event, solvent migration and corresponding dimensional change can be formulated by one dimensional mathematic description in spherical coordinate because of radial symmetry. Here diffusion experiment on a gel sphere is presented.

6.2.4.1 Sample preparation

Sphere is one of the simplest geometries, but not an easy one to make. In this study, spherical gel samples were made using suspension photopolymerization as illustrated in Figure 6.5. PEGDA monomer was put into oil bath. Since PEGDA and oil are immiscible, PEGDA tends to stay together forming a large droplet. Once stirred, it dissociates into many small droplets of PEDGA, each of which is in spherical shape to minimize surface energy. UV is then illuminated before long to initiate photopolymerization, because small PEGDA droplets collapse together overtime and precipitate due to relatively higher density. The sphere were washed and rinsed

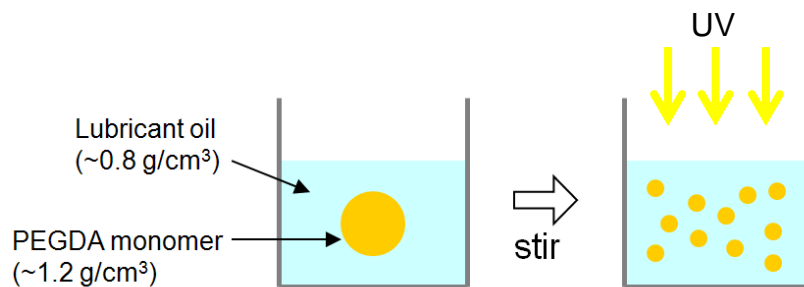


Figure 6.5 Fabrication of spherical gels by photopolymerization in suspension. Taking advantage of immiscible fluid, spherical geometry is created.

thoroughly with acetone, and allowed to dry in a desiccator before the experiment.

Diameter of resulting gel spheres ranges widely spanning from a few microns to millimeters. Smaller spheres are favorable in general in terms of uniformity of material property, but for practical reasons, $\sim 500\ \mu\text{m}$ diameter spheres were used.

6.2.4.2 Experiment and result

A gel sphere was placed in water while diffusion front penetration and swelling diameter were recorded by a camera. Clear moving interface was observed between transparent dry core and swollen outer shell. The time course of dimensional change and water swelling front movement have been measured and are plotted together in Figure 6.6.

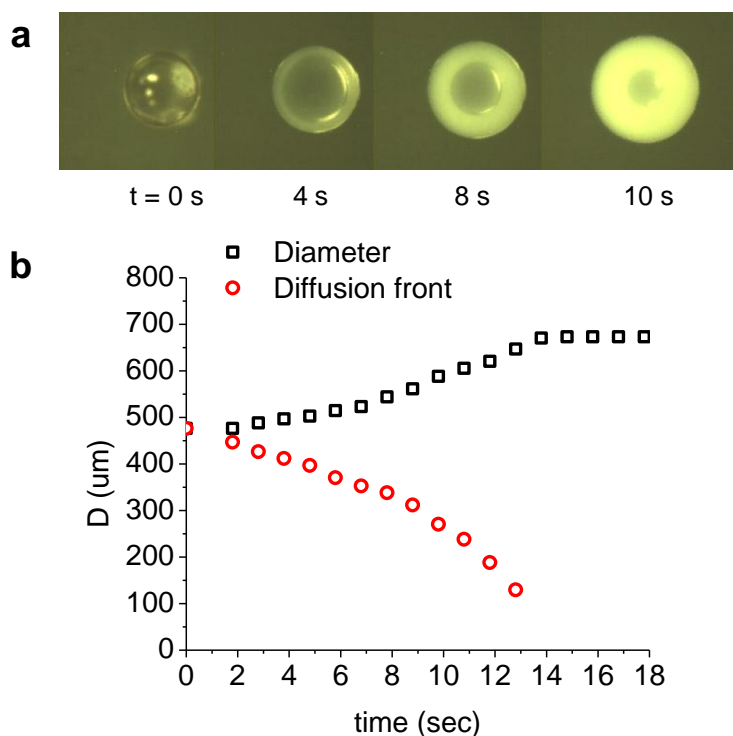


Figure 6.6 (a) diffusion experiment on a gel sphere (b) time course of dimensional change and water diffusion front. A scale bar indicates $500\ \mu\text{m}$.

Interestingly, diffusion front propagation speed gets faster as it further travels and approaches the core, in contrast to the case of rod experiment where diffusion front propagation speed gets slower as shown in Figure 6.2. This accelerating diffusion front speed has been explained as an outcome of the effect of spherical geometry, not a nature of diffusion itself [14].

6.2.5 DIFFUSIVITY MEASUREMENT

6.2.5.1 Background

Diffusion is a mass transport process resulting in mixing of molecules without bulk motion or agitation. Diffusion coefficient, which characterizes proportionality of the flux with respect to concentration gradient, is highly influenced by factors including the size of diffusing molecules, temperature, and the environmental microstructure. Of paramount importance in molecular diffusion are physical properties of the microenvironment where diffusing molecules are transporting through since molecular collision which hinders thermodynamic Brownian motion of particles is one of the critical factors to determine diffusivity.

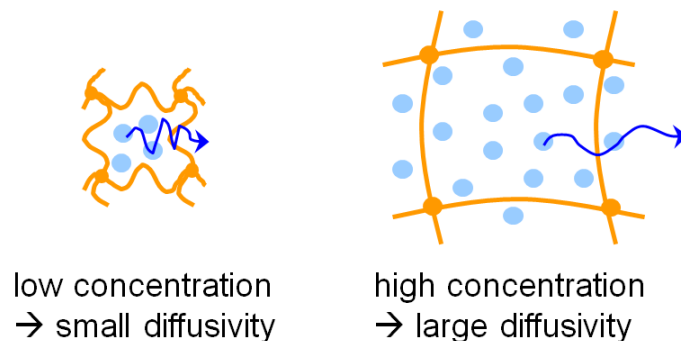


Figure 6.7 Different solvent diffusivity in different swelling concentration (or polymeric network expansion)

Diffusion of solvent molecules in polymer is therefore vastly affected by microstructure of polymeric network. In particular, diffusivity of solvent in swelling gel depends highly on the degree of swelling deformation because swelling relaxes molecular entanglement of polymer chains, allowing solvent molecules to migrate with less molecular collision against polymer chains, as illustrated in Figure 6.7. As macroscopic behavior of hydrogel depends on microscopic diffusional motion of solvent molecules, it is very important to characterize and quantify how solvent diffusivity changes with polymer swelling.

Magnetic resonance imaging (MRI) provides a unique opportunity to quantify diffusion properties of solvent molecules in biological samples [15] and in polymer network [16, 17], because it is able to characterize diffusional behavior non-invasively.

Nuclear magnetic resonance (NMR) scan begins with the excitation of the nuclei with a 90 degree radiofrequency (rf) pulse, which results in tilting the magnetization vector (spin) perpendicular to the magnetic field. Subsequently, spin precesses around the magnetic field with angular frequency proportional to the magnetic field. Exponential decay of the transverse component of the spin is characterized by spin-

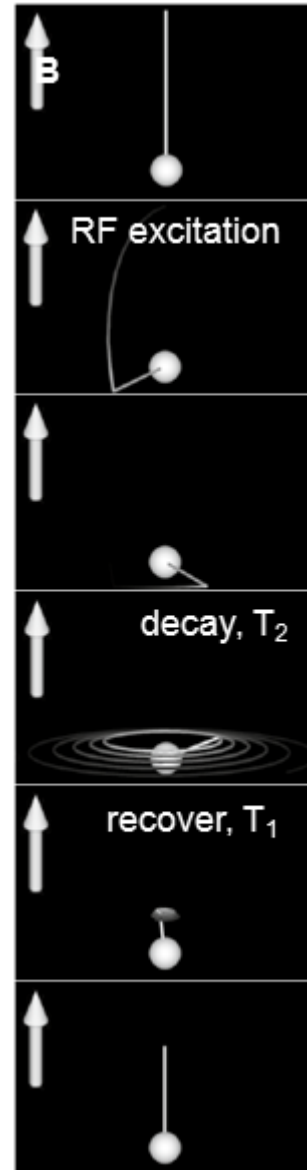


Figure 6.8 NMR scan [15]

spin relaxation time, T_2 , and exponential recovery of longitudinal spin component is characterized by spin-lattice relaxation time, T_1 . If this is done in magnetic gradient, spins in different location experience different magnetic field, thus having different precession angular frequency. If there were no molecular transport, phase shift would depend on the location and remain coherent. However, as a result of diffusion of molecules in space, phase incoherency occurs over time and is detected by scanner, providing spatio-temporal information of migrating molecules. This signal allows for measurement of diffusivity.

The process is mathematically described as

$$I \propto w \cdot \exp(-T_E/T_2) \cdot [1 - \exp(-T_R/T_1)] \cdot \exp(-bD) \quad (6.1)$$

where I denotes local signal intensity, w water volume fraction, T_E echo time, T_R repetition time, b diffusion sensitivity factor, and D diffusivity, respectively [15]. If a series of signals are acquired under different magnetic gradient (by varying b) while keeping the other parameters the same, diffusivity can be obtained by the following equation.

$$D = -\frac{\ln[I(b_2)/I(b_1)]}{b_2 - b_1} \quad (6.2)$$

6.2.5.2 Sample preparation

Because of the aforementioned advantages, MRI is employed in this work to probe *in situ* water diffusivity in PEG-DA hydrogel. For concentration dependent diffusivity, gel samples with different solvent concentration were prepared. A glass tube was filled with PEGDA prepolymer solution and illuminated for 10 s in UV oven,

followed by another 10 s exposure after flipping. A gel rod was then retrieved out of the glass tube mold and put in acetone bath for rinse for 3 hours, followed by 1 hour dry in a vacuum desiccator. PEGDA gel rods with diameter of 2.94mm and 4.17mm were made in this way using glass tubes with different diameter. Then these samples were inserted into MRI glass tubes with the inner diameter of 5mm. The samples were allowed to swelling inside the tube as shown in Figure 6.9. Due to the confinement from the MRI glass tube wall, resulting swelling ratios of each sample were 1.7 and 1.2, respectively.

Corresponding solvent volume fractions $\phi = \frac{\lambda^3 - 1}{\lambda^3}$ are 0.8 and 0.42 respectively. Another

MRI glass tube was filled with water for the sample with solvent volume fraction of 1.

Three samples with solvent volume fraction 0.42, 0.8, and 1 were tested.



Figure 6.9 Sample preparation for MRI diffusivity measurement. Diffusivity of water from three samples with solvent volume fraction 0.42, 0.8, and 1 was measured.

6.2.5.3 Result

Diffusivity in these gel samples was measured by 600MHz NMR scanner. The measurement was carried out by Prof. Georgiadis group. The diffusivity was determined using a standard pulsed field gradient spin-echo sequence with different diffusion sensitivity factors [16]. Figure 6.10 shows linear fitting of the data collected from different samples with different solvent concentration using equation (6.2). Slope of the fitted line gives diffusivity.

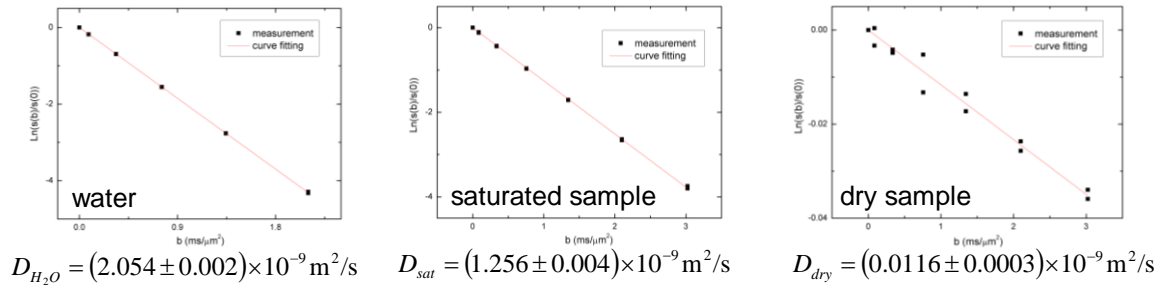


Figure 6.10 Diffusivity of water in samples with different water concentration

Acquired local water concentration and diffusivity of each sample was mapped to construct the diffusivity profile as a function of solvent volume fraction obtained above. The data points were fitted to Thomas and Windle's phenomenological model [13] as shown in Figure 6.11, to obtain $D = D_0 \exp(a_d \phi) = 0.0019 \times \exp(17.6 \times \phi) \times 10^{-9} \text{ m}^2/\text{s}$ where D_0 is diffusivity of water in the dry polymer and a_d solvent-dependent diffusion constant.

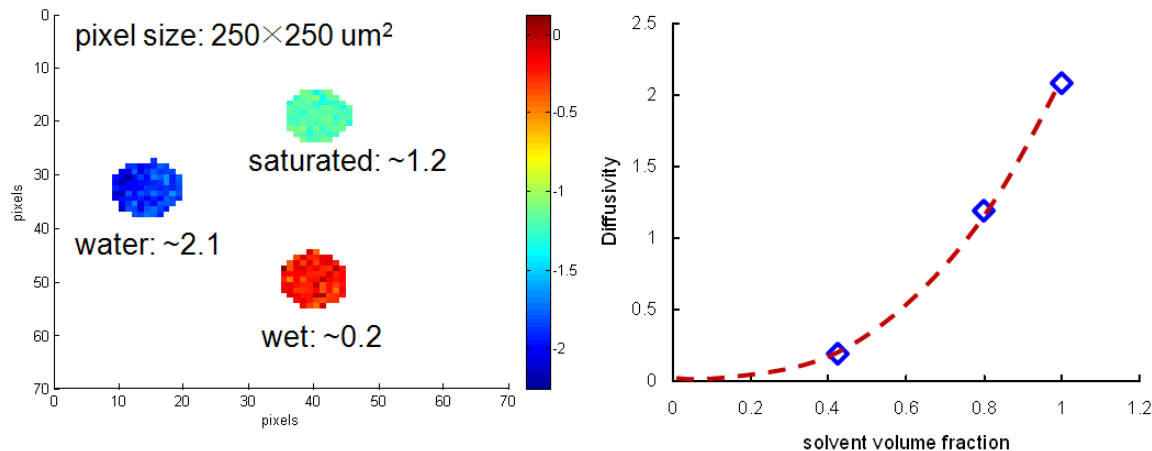


Figure 6.11 Local diffusivity and water concentration measurement result. The result is fitted to phenomenological diffusivity function to obtain diffusivity parameters.

6.3 MECHANICS MODEL

A phenomenological model for the coupled large deformation and case II diffusion in gels is briefly presented. The present mechanics model was developed in collaboration with Prof. Jiang in Arizona State University and more detail about the model can be found elsewhere [18]. The detailed topics include the review of the reference and current configurations that are needed to describe the finite deformation during swelling/shrinking of the gel, followed by the introduction of the field variables used in the model. Using the principle of virtual work, the equilibrium equations and boundary conditions are then described. The mass conservation law of solvents is established in the reference configuration. The materials models, i.e., the constitutive relations of polymeric network are viscoelastic and the diffusion law is specified.

6.3.1 CONFIGURATIONS AND FIELD VARIABLES

The deformation gradient \mathbf{F} which maps the reference configuration \mathcal{R} (e.g., dry state) and current configuration \mathcal{r} (e.g., swollen state) as shown in Figure 6.12 is given by

$$\mathbf{F}(\mathbf{X}, t) = \frac{\partial \mathbf{x}(\mathbf{X}, t)}{\partial \mathbf{X}} \quad (6.3)$$

The mechanical forces do the work and deform the gel. The gel stress $\boldsymbol{\sigma}$ in the current configuration is given by

$$\boldsymbol{\sigma} = \boldsymbol{\sigma}^{def} - P\mathbf{1} \quad (6.4)$$

where $\boldsymbol{\sigma}^{def}$ is the gel stress due to the deformation of the polymeric network, $-P\mathbf{1}$ is the osmotic pressure due to the migration of the solvent molecules, and $\mathbf{1}$ is the identity tensor. The stress in the reference configuration is the second Piola-Kirchhoff stress \mathbf{T} given by

$$\mathbf{T} = \det(\mathbf{F})\mathbf{F}^{-1} \cdot \boldsymbol{\sigma} \cdot \mathbf{F}^{-T} \quad (6.5)$$

and the gel stress due to the deformation of the polymeric network is then \mathbf{T}^{def} . Here

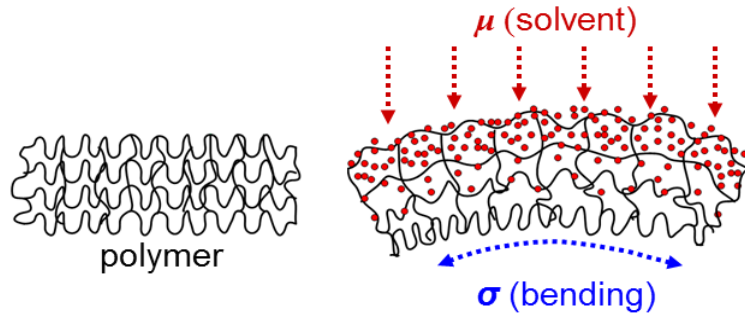


Figure 6.12 Reference (left) and current (right) configuration of polymer system experiencing swelling deformation

$\det(\mathbf{F})$ is the determinant of \mathbf{F} ; \mathbf{F}^{-1} and \mathbf{F}^{-T} are the reciprocal and the reciprocal transpose of deformation gradient \mathbf{F} , respectively.

The chemical potential μ pumps solvent molecules into the polymeric network. In the current configuration, the volume of the solvent molecules in a volume element dv is ϕdv and the change of solvent volume due to the migration of solvents crossing an area element da in the gel per unit time is $\mathbf{j} \cdot d\mathbf{a} = j_i n_i da$, where \mathbf{n} is the unit vector of an area element. In the reference configuration, the volume of the solvent molecules in a volume element dV is ΦdV and the change of solvent volume due to the migration of solvents crossing an area element $d\mathbf{A}$ in the gel per unit time is $\mathbf{J} \cdot d\mathbf{A} = J_K N_K dA$, where N_K is the unit vector of an area element.

The variables in the current and reference configurations describe the identical physics, i.e.,

$$\begin{aligned} \text{volume of solvent molecules : } \phi dv &= \Phi dV, \\ \text{volume change due to diffusion crossing an area element: } \mathbf{j} \cdot d\mathbf{a} &= \mathbf{J} \cdot d\mathbf{A}. \end{aligned} \quad (6.6)$$

Therefore, the variables defined in two configurations are related through the deformation gradient and Nanson's formula,

$$\Phi = \phi \det(\mathbf{F}) \quad (6.7)$$

and

$$\mathbf{J} = \det(\mathbf{F}) \mathbf{j} \cdot \mathbf{F}^{-T} = \det(\mathbf{F}) \mathbf{F}^{-1} \cdot \mathbf{j} \quad (6.8)$$

6.3.2 EQUILIBRIUM EQUATIONS AND BOUNDARY CONDITIONS

The equilibrium equations and traction boundary conditions in the current configuration $\boldsymbol{\kappa}$ can be established by the principle of virtual work as

$$\overset{\triangleright}{\nabla} \cdot \boldsymbol{\sigma} = \mathbf{0}, \text{ or } \overset{\triangleright}{\nabla} \cdot \boldsymbol{\sigma}^{def} = \overset{\triangleright}{\nabla} P \text{ in } \boldsymbol{\kappa}, \quad (6.9)$$

$$\mathbf{n} \cdot \boldsymbol{\sigma} = \mathbf{t} \text{ on } \boldsymbol{\alpha}. \quad (6.10)$$

From the Nanson's formula, the equilibrium equations and boundary conditions in the reference configurations are

$$\overset{\triangleleft}{\nabla} \cdot (\mathbf{T} \cdot \mathbf{F}^T) = \mathbf{0}, \text{ or } \overset{\triangleleft}{\nabla} \cdot (\mathbf{T} \cdot \mathbf{F}^T) = \det(\mathbf{F}) \mathbf{F}^{-T} \cdot \overset{\triangleleft}{\nabla} P \text{ in } V, \quad (6.11)$$

$$\mathbf{N} \cdot \mathbf{T} \cdot \mathbf{F}^T = \mathbf{a}_N \mathbf{t} \text{ on } A. \quad (6.12)$$

6.3.3 MASS CONSERVATION LAW

In the reference configuration, the conservation law in the differential form can be obtained as

$$\frac{\partial}{\partial t} \Phi(\mathbf{X}, t) + \overset{\triangleleft}{\nabla} \cdot \mathbf{J}(\mathbf{X}, t) = \mathbf{0} \text{ in } \mathcal{V}. \quad (6.13)$$

The number of solvent molecules across an interface provides the boundary condition of the mass conservation law, i.e.,

$$\mathbf{J}(\mathbf{X}, t) \cdot \mathbf{N} = \bar{J}(\mathbf{X}, t) \text{ on } \boldsymbol{\alpha}, \quad (6.14)$$

where \bar{J} is the prescribed flux across the surface.

6.3.4 CONSTITUTIVE RELATION OF THE POLYMERIC NETWORK

Glassy polymers have time-dependent viscoelastic behavior. The standard linear solid (SLS) model is the simplest model to describe both creep and stress relaxation for viscoelastic material. A pictorial representation of the SLS model is shown in Figure 6.13, in which a linear combination of two linear springs (G_r and G_m) a dashpot (η) represents elastic and viscous components, respectively. The constitutive relation is given by

$$\frac{\partial \sigma}{\partial t} + \frac{G_m}{\eta} \sigma = (G_m + G_r) \frac{\partial \varepsilon}{\partial t} + \frac{G_m G_r}{\eta} \varepsilon, \quad (6.15)$$

where the material parameters G_r and G_m the modulus, and η the extensional viscosity.

This one-dimensional small-deformation constitutive relation is extended to three-dimensional large deformation SLS model, considering the rate of second Piola-Kirchhoff stress \mathbf{T} with respect to time as objective.

$$\frac{\partial \mathbf{T}^{def}}{\partial t} + \frac{G_m}{\eta} \mathbf{T} = \frac{2}{3} (G_m + G_r) \frac{\partial \mathbf{E}^{(-1)}}{\partial t} + \frac{2G_m G_r}{3\eta} \mathbf{E}^{(-1)}, \quad (6.16)$$

where $\mathbf{E}^{(-1)} = \frac{1}{2}(\mathbf{I} - \mathbf{C}^{-1})$ is the Alamnsi strain tensor.

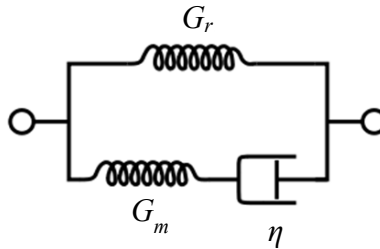


Figure 6.13 Standard linear solid (SLS) viscoelastic material model

6.3.5 DIFFUSION LAW

The flux in current configuration is adopted by Hong et al [10] as

$$\mathbf{j} = -D_{12} \left[\frac{v\phi}{kT(1-\phi)(1-2\chi\phi)} \overset{\triangleright}{\nabla} \cdot \boldsymbol{\sigma}^{def} + \overset{\triangleright}{\nabla} \phi \right], \quad (6.17)$$

where D_{12} is the mutual diffusivity, $k = 1.38 \times 10^{-23} JK^{-1}$ is the Boltzmann constant, T is the temperature, and χ is the Flory interaction parameter.

Suggested by Thomas and Windle [13] and Wu and Peppas [19], the mutual diffusivity D_{12} has a strong dependence on the solvent concentration and can be expressed in an exponential form as

$$D_{12} = D_o \exp(a_d \phi), \quad (6.18)$$

where D_o is the diffusivity of solvent into the dry polymer and $a_d (>0)$ is a phenomenological parameter that describes the solvent concentration dependence. The empirical expression (Eq. (6.18)) will be characterized in the next section and the phenomenological parameter a_d will be measured.

The flux defined in the reference configuration can be obtained by

$$\mathbf{J} = -D_{12} \left\{ \frac{v\Phi \det(\mathbf{F}) \mathbf{F}^{-1} \cdot \left[\overset{\triangleleft}{\nabla} \cdot (\mathbf{T}^{def} \cdot \mathbf{F}^T) \right]}{kT(\det \mathbf{F} - 2\chi\Phi)} + \mathbf{F}^{-1} \cdot \left[\overset{\triangleleft}{\nabla} \cdot (\mathbf{F}^{-1}\Phi) \right] \right\}. \quad (6.19)$$

Here the ideal mixing is assumed, i.e., there is no volume change during the diffusion process:

$$\det(\mathbf{F}) = 1 + \Phi. \quad (6.20)$$

In other words, both polymer and solvent molecules are incompressible during the mixing process.

6.3.6 EXPERIMENTAL CHARACTERIZATION OF MATERIAL PARAMETERS

This section characterizes the materials parameters introduced in the phenomenological model by compression test. The model presented in the previous section involves a set of parameters, including

- (1) Young's modulus of the dry polymer G_r and G_m ,
- (2) Poisson's ratio ν of the dry polymer,
- (3) extensional viscosity of the dry polymer η ,
- (4) and Flory's interaction parameter χ .

6.3.6.1 Viscoelasticity

Viscoelastic parameters including Young's modulus G_r and G_m , viscosity η , and Poisson's ratio ν of the dry polymer were measured by compression test.

Gel disks were made to measure Young's modulus G_r and G_m , viscosity η and Poisson's ratio ν of the dry polymer in compression test. 1 mm gap between two glass slides was filled with prepolymer solution. Sample was photo-polymerized for 10 s in ultraviolet (UV) oven, followed by another 10 s exposure after flipping over for uniform crosslinking. Then, the 1 mm thick film was punched to obtain a set of gel disks. Samples were put in acetone bath for rinse for 3 hours to remove remaining uncrosslinked PEG after polymerization. Then samples were allowed to dry for 1 hour in a vacuum desiccator.

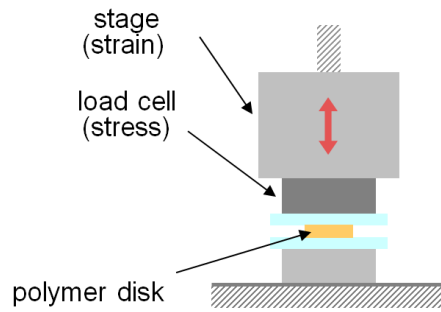


Figure 6.14 Experimental setup for compression test to measure viscoelastic mechanical parameters

A gel disk was compressed between two parallel glass plates, one of which is fixed and the other is connected to a load cell and then to a computer-controlled stage. Figure 6.14 illustrates the experimental setup. Oil is applied between the sample and the compression plates for lubrication to make ease of lateral expansion of the sample under compression.

Poisson's ratio ν of the dry polymer was first measured. A gel disk was compressed normal to the face and lateral expansion of the sample was recorded by a digital camera from the side as shown in Figure 6.15. Poisson's ratio was obtained from the input axial displacement and measured lateral expansion. Measured Poisson's ratio ν of the dry polymer was 0.45.

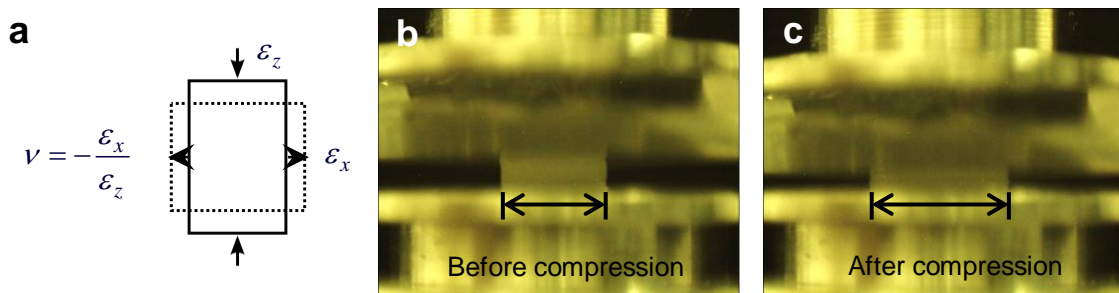


Figure 6.15 (a) Definition of Poisson's ratio. A gel disk is compressed as the radial expansion is measured before (b) and after (c) compression.

For time dependent material properties of the polymer, ramp-and-hold compressive stress input was applied and time varying stress was measured and fitted to the response of SLS model to obtain Young's modulus of the dry polymer G_r and G_m and extensional viscosity η of the dry polymer.

Ramp-and-hold compressive strain input is described as

$$\varepsilon(t) = \begin{cases} at & (t \leq t_0) \\ at_0 & (t \geq t_0) \end{cases} \quad (6.21)$$

From the constitutive relation of SLS model (6.15), stress response to input (6.21) is obtained as

$$\sigma(t) = a \left[\left\{ G_r t + \tau_m G_m \left(1 - e^{-t/\tau_m} \right) \right\} - \left\{ G_r (t - t_0) + \tau_m G_m \left(1 - e^{-(t-t_0)/\tau_m} \right) \right\} u(t - t_0) \right] \quad (6.22)$$

Stress data acquired from the compression test was then fitted to (6.22) to extract Young's modulus G_r and G_m and viscosity η of the dry polymer, as shown in Figure 6.16. Obtained values of the viscoelastic parameters are listed in Table 6.1.

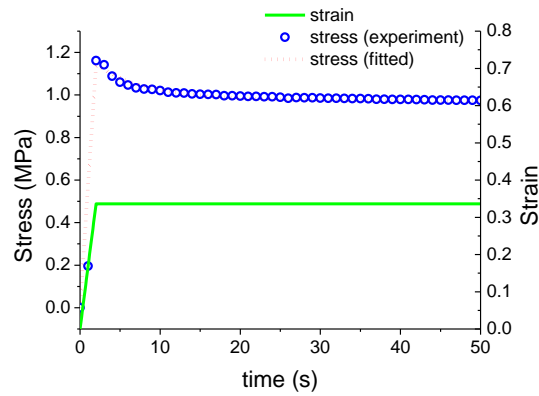


Figure 6.16 Experimentally measured stress profile resulting from ramp-and-hold strain input is fitted to SLS model to extract viscoelastic parameters.

Table 6.1 Viscoelastic parameters of the dry polymer.

| G_r (MPa) | G_m (MPa) | τ_m (s) | η ($\times 10^6$ N·s/m ²) | ν |
|-------------|-------------|--------------|---|-------|
| 2.90 | 0.58 | 6.77 | 3.91 | 0.45 |

6.3.6.2 Flory interaction parameter χ

Flory interaction parameter χ can be calculated by the experimentally measured equilibrium swelling ratio λ_{eq} . The equilibrium swelling is reached at the long-time limit, at which $\boldsymbol{\sigma} = \mathbf{0}$, $\boldsymbol{\mu} = \mathbf{0}$, $\mathbf{F} = \lambda_{eq}\mathbf{I}$. Using Eqs. (6.4), (6.5), (6.16), and eliminating P , we obtain that

$$\frac{G_r}{3} \left(\frac{1}{\lambda_{eq}} - \frac{1}{\lambda_{eq}^3} \right) + \frac{kT}{\nu} \left[\ln \left(1 - \frac{1}{\lambda_{eq}^3} \right) + \frac{1}{\lambda_{eq}^3} + \frac{\chi}{\lambda_{eq}^6} \right] = \mathbf{0}, \quad (6.23)$$

which can be used to determine the Flory interaction parameter χ .

We measured Young's modulus of the polymer above, and $G_r = 2.90\text{MPa}$. A gel disk was prepared following the same procedure for compression test. Then diameter was measured in dry state and in full swelling state in water as shown in Figure 6.17, to obtain the equilibrium swelling ratio, $\lambda_{eq} = 1.75$ where

$$\lambda_{eq} = \frac{\text{fully swollen diameter}}{\text{dry diameter}} \quad (6.24)$$

From Eq. (6.23), we obtain $\chi = 0.456$.

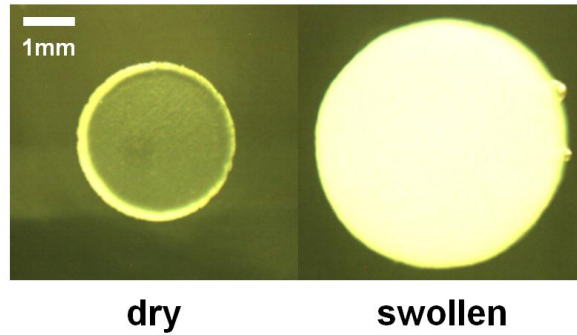


Figure 6.17 Equilibrium swelling test on a gel disk to determine Flory interaction parameter χ .

6.4 COMPARISON WITH EXPERIMENT

Using the measured materials parameters in the previous section, we apply the model to study one-dimensional solvent diffusion in a gel rod and compare with experiment.

6.4.1 THEORETICAL AND EXPERIMENTAL RESULTS AND COMPARISON

Partial differential equations from the constitutive equation and the mass conservation law are solved numerically by finite difference method. Parameters used to in the simulation are listed in Table 6.2

Table 6.2 Parameters for simulation.

| G_r (MPa) | G_m (MPa) | η ($\times 10^6$ N·s/m ²) | ν | D_0 ($\times 10^{-9}$ m ² /s) | a_d | χ |
|-------------|-------------|--|-------|--|-------|--------|
| 2.90 | 0.58 | 3.91 | 0.45 | 0.0019 | 17.6 | 0.456 |

Figure 6.18a plots the concentration profile $\Phi(X_3, t)$. It shows that there is a sharp transition differentiating the wet region (with concentration close to the equilibrium value) and the dry region (with zero concentration), which defines the sharp front. With time evolving, the front moves inside the gel and eventually the entire gel is wet. Figure 6.18b shows the concentration profile at the vicinity of the end. It indicates the transition from the short-time limit (elasticity $G_m + G_r$) to the long-time limit (elasticity G_r). The sharp front location can be obtained from Figure 6.18a and is plotted in Figure 6.18b, with comparison with experiments. It shows that this model agree well with experiments, from the match of both time scale and the overall trend of sharp front location.

The length of the rod during swelling can be obtained by

$$l(t) = \int_0^L (1 + \Phi(X_3, t)) dX_3 \quad (6.25)$$

Figure 6.18c compares the length profile $l(t)$ calculated from Eq.(6.25) and measured from experiments. It shows that the model agree well with experiments.

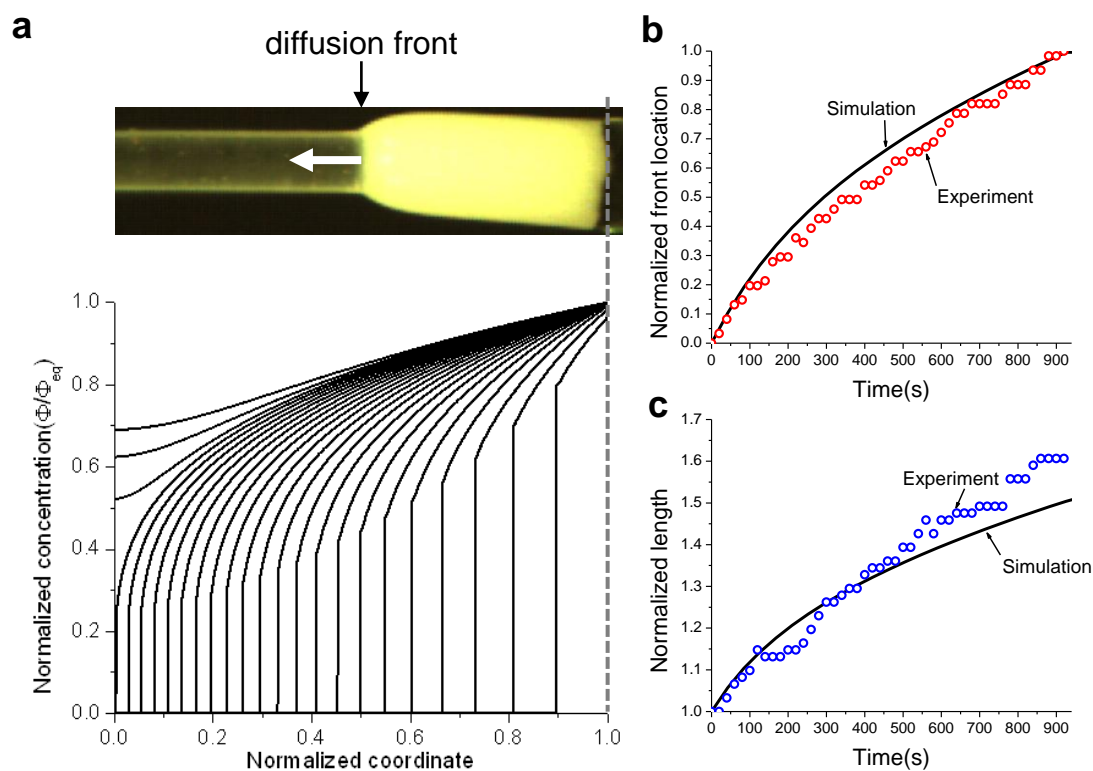


Figure 6.18 (a) Simulation result for concentration profile at different times showing propagation of sharp diffusion front. Time interval between lines is equal and 42 sec. Result comparison for (b) diffusion front propagation and (c) length of the rod over time.

6.5 SUMMARY

Here we present experimental techniques to quantify the non-Fickian diffusion in the swelling polymer in an attempt to predict the dynamics of local deformation in such solvent driven micro-actuators. We recorded the evolving diffusion front of solvent in poly(ethylene glycol) diacrylate (PEG-DA) hydrogel upon wetting. In order to measure diffusivity of solvent in the polymer, magnetic resonance imaging (MRI) was employed. In both diffusion front propagation and polymer deformation, simulation result agreed

well with 1D swelling experiment of a PEG-DA rod. Not only does the established model provide a fundamental theoretical basis for hydrogel swelling, but it will play a critical role to develop full 3D finite element method (FEM) model to analyse and predict dynamic response of swelling-driven micro actuators presented in Chapter 3 and 4 and swelling induced pattern formation discussed in Chapter 5. We expect that our theoretical model and experimental method for non-Fickian diffusion will help to provide fundamental basis in exploration of various dynamic hydrogel devices interacting with solvent molecules.

6.6 REFERENCES

1. Beebe, D.J., et al., *Functional hydrogel structures for autonomous flow control inside microfluidic channels*. Nature, 2000. **404**(6778): p. 588-590.
2. Griffith, L.G., *Tissue Engineering--Current Challenges and Expanding Opportunities*. Science, 2002. **295**(5557): p. 1009-1014.
3. Jeong, B., et al., *Biodegradable block copolymers as injectable drug-delivery systems*. Nature, 1997. **388**(6645): p. 860-862.
4. Qiu, Y. and K. Park, *Environment-sensitive hydrogels for drug delivery*. Advanced Drug Delivery Reviews, 2001. **53**(3): p. 321-339.
5. Lee, H., C. Xia, and N.X. Fang, *First jump of microgel; actuation speed enhancement by elastic instability*. Soft Matter, 2010. **6**(18): p. 4342.

6. Xia, C. and N.X. Fang, *3D microfabricated bioreactor with capillaries*. Biomedical Microdevices, 2009. **11**(6): p. 1309-1315.
7. Guan, J., et al., *Self-Folding of Three-Dimensional Hydrogel Microstructures*. The Journal of Physical Chemistry B, 2005. **109**(49): p. 23134-23137.
8. Tanaka, T. and D.J. Fillmore, *Kinetics of Swelling of Gels*. Journal of Chemical Physics, 1979. **70**(3): p. 1214-1218.
9. De Kee, D., Q. Liu, and J. Hinestroza, *Viscoelastic (Non-Fickian) Diffusion*. The Canadian Journal of Chemical Engineering, 2005. **83**(6): p. 913-929.
10. Hong, W., et al., *A theory of coupled diffusion and large deformation in polymeric gels*. Journal of the Mechanics and Physics of Solids, 2008. **56**(5): p. 1779-1793.
11. Hong, W., X. Zhao, and Z. Suo, *Large deformation and electrochemistry of polyelectrolyte gels*. Journal of the Mechanics and Physics of Solids, 2010. **58**(4): p. 558-577.
12. Alfrey, T., E.F. Gurnee, and W.G. Lloyd, *Diffusion in Glassy Polymers*. Journal of Polymer Science Part C-Polymer Symposium, 1966(12PC): p. 249-&.
13. Thomas, N.L. and A.H. Windle, *A Theory of Case-II Diffusion*. Polymer, 1982. **23**(4): p. 529-542.
14. Lee, P.I. and C.J. Kim, *Effect of Geometry on Solvent Front Penetration in Glassy-Polymers*. Journal of Membrane Science, 1992. **65**(1-2): p. 77-92.
15. Johansen-Berg, H. and T.E.J. Behrens, *Diffusion MRI: From Quantitative Measurement to In vivo Neuroanatomy*. 2009, Boston: Elsevier.

16. Raguin, G., et al. *Magnetic Resonance Imaging (MRI) of Water Diffusion in Hydroxyethyl Methacrylate (HEMA) Gels*. in *Mater. Res. Soc. Symp. Proceedings*. 2006.
17. Naji, L., J.A. Chudek, and R.T. Baker, *Magnetic resonance imaging study of a soft actuator element during operation*. *Soft Matter*, 2008. **4**(9): p. 1879.
18. Zhang, J., et al., *Coupled Large Deformation and Case II Diffusion in Gels: A Viscoelastic Model and Experimental Characterizations*. Manuscript in preparation.
19. Wu, J.C. and N.A. Peppas, *Modeling of Penetrant Diffusion in Glassy-Polymers with an Integral Sorption Deborah Number*. *Journal of Polymer Science Part B-Polymer Physics*, 1993. **31**(11): p. 1503-1518.

7. SUMMARY AND FUTURE WORK

7.1 SUMMARY

This thesis has studied design and fabrication of polymeric soft active micro devices based on an unconventional three-dimensional microfabrication technology, projection micro-stereolithography (P μ SL), and bio-inspired design principles.

Brief introduction on microfabrication technologies and hydrogels and motivation for this work were provided in Chapter 1.

A novel three dimensional microfabrication system, projection micro-stereolithography (P μ SL), was introduced in Chapter 2. Characterization for the optical lithography system and polymerization process has been studied. Integration of membrane-pump system to P μ SL for extending flexibility of material choice was presented and heterogeneously integrated multiple material 3D microfabrication was demonstrated. The P μ SL system and optimized 3D fabrication process was used throughout the rest of the study.

Generation of active motion has been studied in Chapter 3. 3D fabrication system developed in Chapter 2 was used to extend the potential of soft functional materials which have been increasingly used in many fields of science and engineering. Local swelling control of 3D hydrogel devices using direct solvent delivery through embedded microfluidic network has been successfully demonstrated. This actuation is simple, reversible, and spontaneous in a sense that auxiliary devices for control and power supply

are not required. Demonstration of several active devices to show potential in many other disciplines was presented. Limitation of actuation time scale was also discussed.

There has been a perception that devices made of soft material are slow. This is perhaps true in general, but nature is full of examples of rapidly moving soft organisms. Design principle of using elastic instability to promote movement speed was borrowed from nature and successfully implemented in soft micro devices in Chapter 4. An order of magnitude improvement on swelling actuation speed of a hydrogel micro device was demonstrated by incorporating snap-buckling instability using P μ SL. Ability to rapidly respond to external stimulus will broaden the scope and create new opportunities of functional hydrogel applications in various research areas ranging from sensors and actuators to soft robotics, artificial muscle, and biomedical engineering.

Another possible application of active hydrogel device is pattern transformation. It has been demonstrated in Chapter 5 that precisely manufactured hydrogel device can transform the pattern from one to another upon wetting, or possibly by external stimulus. Demonstration of the control over spontaneous pattern formation promises new design strategy in the development of self-operating active devices with tunable properties. Moreover, realization of sophisticated pattern transformation holds great potential to study morphogenesis of various physiological entities.

Use of hydrogel and its dynamic swelling response associated with solvent migration runs throughout this thesis. More fundamental study regarding hydrogel swelling was studied in Chapter 6. Swelling mechanics of viscoelastic hydrogel and abnormal diffusional behavior of solvent molecules in glassy polymer was investigated

theoretically and experimentally. A mechanics model dedicated to capture this highly complex phenomenon was developed and various experimental techniques to quantify and characterize related parameters were presented.

7.2 FUTURE WORK

The results presented in this thesis opened new avenue towards development of autonomous and multifunctional devices and systems. With the versatile manufacturing capabilities of P μ SL in engineering soft active materials, unique properties of various classes of functional materials can be developed into unconventional devices and applications. Further possibilities can be explored in the following aspects.

7.2.1 FABRICATION

P μ SL is a strong tool to build up 3D micro structures, and MP-P μ SL has added material flexibility to it. Possible future direction of the development of P μ SL can be mass production. Recently, high throughput fabrication of functional micro particles has been reported [1-3]. *in-situ* fabrication in microfluidic environment allowed for various applications such as bioassay [4] and encapsulation of functional particles [5, 6] and living cells [7]. Furthermore, integration of a dynamic mask has been reported [8] and demonstrated mass production of customized multifunctional particles [9, 10] and assembly of micro particles [11]. Integration of microfluidic system in P μ SL is currently being developed for scalable mass production of 3D functional particles as shown in Figure 7.1.

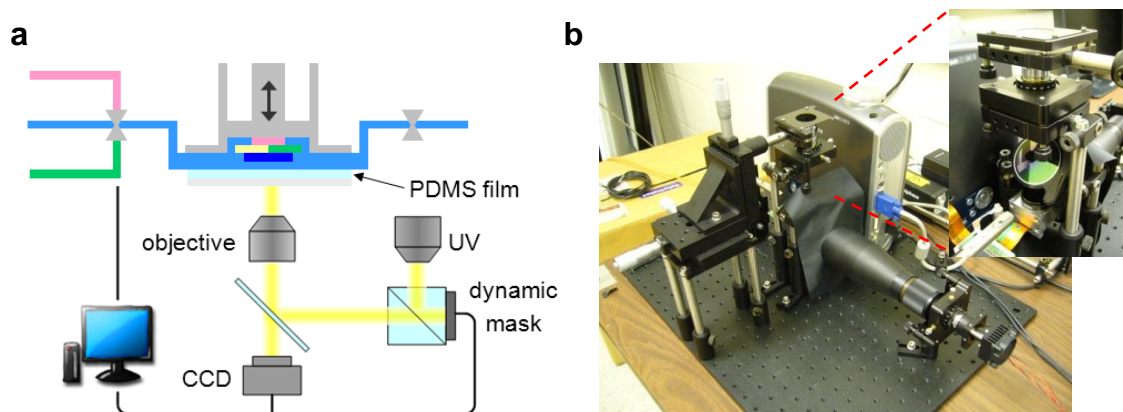


Figure 7.1 (a) schematic of microfluidic in-flow P μ SL. (b) the actual system under development.

7.2.2 MATERIALS

7.2.2.1 Responsive hydrogels

One of the unique properties of hydrogels is the responsiveness to a wide range of external stimuli such as temperature [12], pH [13], light [14], electric fields [15] and many others. With a proper choice of chemical conjugation, hydrogels can be made to swell or contract in response to the change in surrounding environmental conditions. The ability to translate external signal into mechanical response can play a pivotal role in developing autonomous devices that can adapt to ever changing dynamic environment. Using stimuli-responsive hydrogel in P μ SL will greatly contribute to development of multifunctional devices. For the first step towards this goal, pH sensitive hydrogel was synthesized and preliminary experiment to demonstrate tunable swelling behavior of hydrogel in different pH environment was carried out, as shown in Figure 7.2. The pH-responsive hydrogel contracts about 20% from the original dimension in acidic environment, whereas it swells about 20% in basic solution.

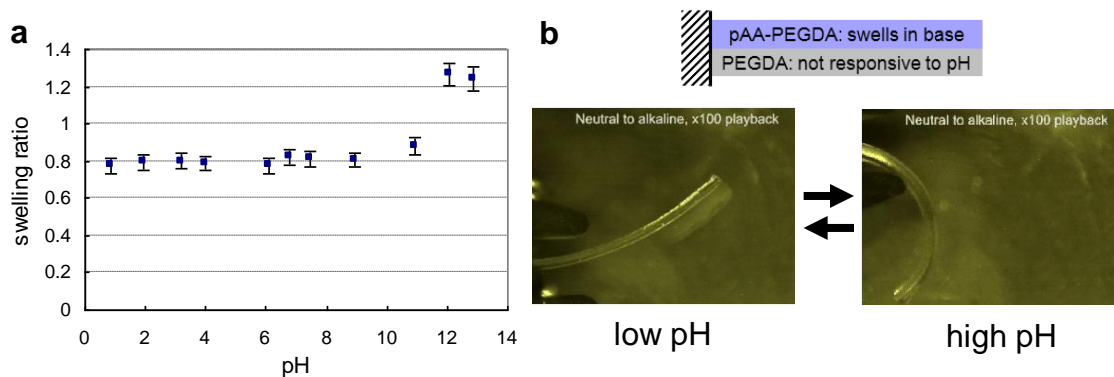


Figure 7.2 (a) measured pH-response of poly(acrylic acid) pAA hydrogel. (b) reversible pH actuation of bilayer polymer beam.

7.2.2.2 Shape memory polymer

Temperature sensitive shape memory polymer (SMP) can retain temporary deformation until the original shape is restored upon heating above the glass transition temperature (T_g). Using sharp contrast in material behaviors below and above T_g , dramatic shape change as well as large mechanical force can be obtained during the transition. Also, this transition can be remotely triggered and repeatedly actuated. Although many devices using temperature sensitive SMPs have been proposed and developed thus far, they rely on conventional manufacturing methods such as laser cut and hot-embossing. In consequence, most of them are limited to simple 2D planar shape, often in large scale, which makes them less feasible in actual use. Of critical importance in developing SMPs into practical devices, therefore, is to be able to freely construct desired structure in length scale tailored to the target application. Lack of such manufacturing technology has hampered full exploration of SMP for more advanced and practical applications. Tert-butyl acrylate - polyethylene glycol dimethacrylate (tBA-PEGDMA) SMP is photo-polymerized using P μ SL and thermally activated shape

recovery was demonstrated in Figure 7.3. 3D micro-fabrication of SMP using P μ SL will help to maximize utilization of SMP and to develop autonomous functional devices by allowing for diverse geometries and structures which would not be made possible otherwise.



Figure 7.3 Shape recovery of tBA-PEGDMA SMP at elevated temperature (70°C) from rolled shape (left) to flat shape (right).

7.3 REFERENCES

1. Dendukuri, D., et al., *Continuous-flow lithography for high-throughput microparticle synthesis*. Nature Materials, 2006. **5**(5): p. 365-369.
2. Dendukuri, D., et al., *Stop-flow lithography in a microfluidic device*. Lab on a Chip, 2007. **7**(7): p. 818.
3. Dendukuri, D., et al., *Modeling of Oxygen-Inhibited Free Radical Photopolymerization in a PDMS Microfluidic Device*. Macromolecules, 2008. **41**(22): p. 8547-8556.
4. Pregibon, D.C., M. Toner, and P.S. Doyle, *Multifunctional Encoded Particles for High-Throughput Biomolecule Analysis*. Science, 2007. **315**(5817): p. 1393-1396.
5. Hwang, D.K., D. Dendukuri, and P.S. Doyle, *Microfluidic-based synthesis of non-spherical magnetic hydrogel microparticles*. Lab on a Chip, 2008. **8**(10): p. 1640.

6. Shepherd, R.F., et al., *Stop-Flow Lithography of Colloidal, Glass, and Silicon Microcomponents*. *Advanced Materials*, 2008. **20**(24): p. 4734-4739.
7. Panda, P., et al., *Stop-flow lithography to generate cell-laden microgel particles*. *Lab on a Chip*, 2008. **8**(7): p. 1056.
8. Chung, S.E., et al., *Optofluidic maskless lithography system for real-time synthesis of photopolymerized microstructures in microfluidic channels*. *Applied Physics Letters*, 2007. **91**(4): p. 041106.
9. Lee, H., et al., *Colour-barcoded magnetic microparticles for multiplexed bioassays*. *Nature Materials*, 2010. **9**(9): p. 745-749.
10. Kim, H., et al., *Structural colour printing using a magnetically tunable and lithographically fixable photonic crystal*. *Nature Photonics*, 2009. **3**(9): p. 534-540.
11. Chung, S.E., et al., *Guided and fluidic self-assembly of microstructures using railed microfluidic channels*. *Nature Materials*, 2008. **7**(7): p. 581-587.
12. Dong, L., et al., *Adaptive liquid microlenses activated by stimuli-responsive hydrogels*. *Nature*, 2006. **442**(7102): p. 551-554.
13. Beebe, D.J., et al., *Functional hydrogel structures for autonomous flow control inside microfluidic channels*. *Nature*, 2000. **404**(6778): p. 588-590.
14. Klinger, D. and K. Landfester, *Photo-sensitive PMMA microgels: light-triggered swelling and degradation*. *Soft Matter*, 2011. **7**(4): p. 1426.

15. Punning, A., M. Kruusmaa, and A. Aabloo, *A self-sensing ion conducting polymer metal composite (IPMC) actuator*. *Sensors and Actuators A: Physical*, 2007. **136**(2): p. 656-664.

APPENDIX A. DERIVATION OF THE WAVE

AMPLITUDE

Given overall wave arclength, wave amplitude is inversely proportional to the number of waves as shown in Figure A.1. Assuming that wavy pattern follows sinusoidal function along the circumference, amplitude of sinusoidal wave for given arclength can be inversely calculated and obtained in a closed form using approximation for the elliptic integral [20]. To this end, radius on the top end of the wrinkled tube can be written as

$$r(\theta, z = h) = R + A \cos n\theta$$

where A is amplitude of the wave to be determined and n is mode number, i.e. the number of waves along the circumference. The first derivative of the radius is

$$r' = \frac{1}{R} \frac{\partial r}{\partial \theta} = -\frac{nA}{R} \sin n\theta$$

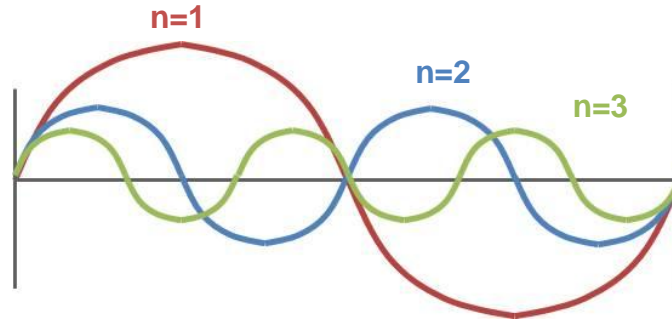


Figure A.1. Given arclength of sinusoidal wave function, wave amplitude becomes smaller as wave number increases.

Approximation for elliptic integral is given in a closed form by

$$\int_0^{\pi/2} \sqrt{1+k^2 \cos^2 x} dx \approx \frac{\pi}{2} \left(3 - \frac{2}{\sqrt{1+k^2/4}} \right) = L$$

Using this formula, arc-length of the wave can be obtained by

$$L = 4n \int_0^{\pi/2n} \sqrt{1 + \left(\frac{nA}{R} \right)^2 \sin^2 n\theta} R d\theta$$

$$= 4R \cdot \left[\frac{\pi}{2} \left(3 - \frac{2}{\sqrt{1 + (nA/R)^2/4}} \right) \right]$$

Solving for A yields

$$A = \frac{D}{n} a(\lambda)$$

$$\text{where } a(\lambda) = \sqrt{\left(\frac{2}{3-\lambda}\right)^2 - 1}.$$

Then wrinkled radius can be now expressed with given parameters as follows.

$$r(\theta, z) = R \left\{ 1 + \frac{2}{n} a(\lambda) \cos n\theta \cdot \frac{z}{h} \right\}$$

APPENDIX B. EFFECT OF MECHANICAL STRESS ON CELL-CELL INTERACTION

B.1 BACKGROUND

Cells in many organs and tissues are constantly experiencing physical force such as compressive/tensile stress due to dynamic muscular motions, viscous shear from blood stream, or hydrostatic pressure related to respiration and digestion, to name a few. Cells adapt to the dynamically changing mechanical environment and, as a result, properties of cells change in response to the applied force such as morphology and interaction with neighboring cells. Therefore, study of the effect of mechanical stress on cells can contribute to understanding of many physiological events such as morphogenesis, metabolic activities, and development of disease.

This study demonstrates controlled application of mechanical stress over large area of a cell layer and quantification of the consequence of mechanical stress on cell-cell bonding strength. There have been studies investigating the influence of mechanical stimulus on cell behavior at a single cell level. However, there is no such circumstance where a cell is isolated from other cells in *in vivo* environment. Therefore, it is important to study the mechano-sensitive behavior of cells in the presence of other neighboring cells. Our approach is to develop a device that can control the stretching of an elastic substrate on which cells are cultured and to assess the change in cell-cell interaction as a result of applied mechanical stress. Figure B.1 illustrates the schematic of this approach.

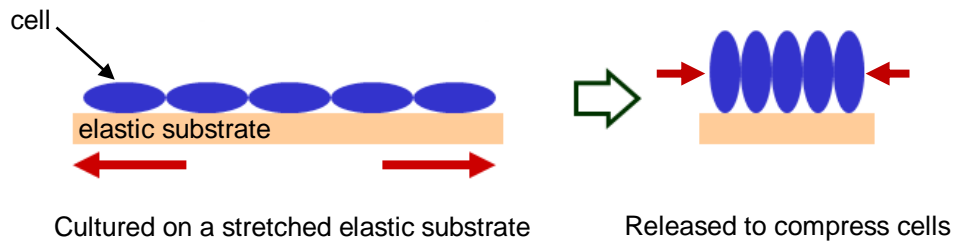


Figure B.1. Application of mechanical stress on cells via elastic deformation of the substrate.

B.2 STRETCHING DEVICE

Stretching device as shown in Figure B.2 has been developed in order to apply compressive stress on cells. The system consists of a motor, a reduction gear with 20:1 reduction ratio, a power supply, and the stretcher. The power supply can provide adjustable voltage by which the rotation speed of the motor is controlled. The motor is connected to the stretcher through the reduction gear which decreases the rotation speed and increases the torque delivered to the stretcher. Especially, it is important to maintain slow rotation speed because experiment typically lasts from hours to days during which strain has to be relaxed continuously at a constant rate. The stretching rate of the device can be varied from 1mm/hr to 80mm/hr depending on the applied voltage. The stretcher has two clamp blocks on both sides. One close to the motor is fixed in space, whereas the other is actuated by the motor and moves laterally, thereby changing the distance between two clamp blocks. The stretcher sits inside a culture dish, so that a film remains completely immersed in culture medium during the operation. As culture medium is

aqueous solution, all components of the stretcher have to be stainless steel because formation of rust results in adverse effect on cell viability.

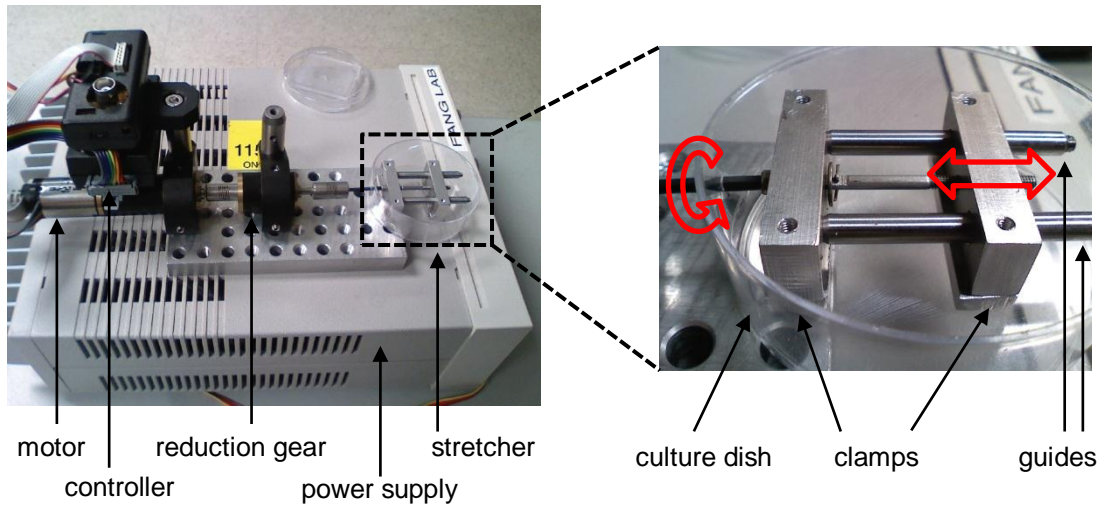


Figure B.2. Cell culture platform with controlled stretching capability

B.3 CELL CULTURE

Cells were cultured on an elastic substrates and the effect of mechanical stress on cell-cell interaction has been studied. Cell culture was carried out by Professor Bhargava group. A polydimethylsiloxane (PDMS) film of 200 μ m thick was prepared and coated with poly-L-lysine solution to promote cell adhesion. Then the coated film was clamped on the both sides of the stretching device. The film was stretched up to 1.5 times (24mm) of its original length (16mm). Typical value of the elongation at break of PDMS is 160%. LNCap (epithelial cells) were seeded on the film and allowed to proliferate. Seeding cell density in culture medium was 40,000 cells/cm³. The cells precipitated on and adhere to the PDMS film. Then it was allowed 2 days for proliferation until closely packed

monolayer of cells formed. Then strain was relaxed at a constant rate of 1mm/hr for 8 hours, resulting in restoration of the original length of the film (16mm). Assuming that the cell monolayer fully covers the film and that all cells maintain the tight adhesion to the film without slipping, this corresponds to application of 33% compressive strain to cells. For control experiment, cells were cultured on the unstretched PDMS film, so there was no mechanical stress applied to cells whatsoever. All other conditions were kept the same.

After experiment was done, cells were taken out, fixed, and stained to visualize cell-cell bonding strength. Figure B.3 shows stained cells from the control experiment and main experiment. Nuclei are stained in blue and E-Cadherin is stained in green. E-Cadherin exists inside cells and it concentrates on the spots once the cell makes binding sites to substrate or adjacent cells. Therefore, E-Cadherin expression shows apparent cell-cell boundary, revealing the shape of the cell. Since E-Cadherin is a type of protein involved in cell adhesion, E-Cadherin expression is also used here as an indicator showing the local strength of the cell-cell bonding. Figure shows that the shape of cells under compression (left) is more like an ellipse with the longer axis perpendicular to the stretching direction, whereas the shape of cells without compression (right) has no directionality. This observation implies that cells under compression have been squeezed and have undergone morphological change because of the mechanical stress.

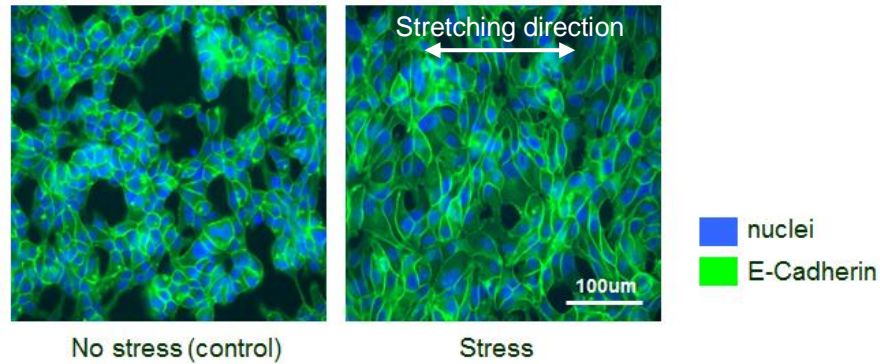


Figure B.3. Representative result. Blue indicates nuclei and green shows E-Cadherin expression.

B.4 ANALYSIS AND RESULTS

In order to quantify the effect of mechanical stress on cell-cell bonding, we measured the E-Cadherin expression on the cell-cell interface. Here we assume that the strength of cell-cell bonding increases with E-Cadherin concentration on the interface and that E-Cadherin expression after staining increases with E-Cadherin concentration. E-Cadherin is present and distributed relatively evenly when the cell has no contact. Once the cell makes contact, however, the cell generates binding sites where E-Cadherin is involved, making local E-Cadherin concentration higher on the interface. In the meantime, there exists E-Cadherin not involved in the binding in the cytoplasm as well, but in a relatively low concentration. We are not interested in this “background” E-Cadherin because we want to study how cell-cell binding is influenced by external mechanical stress. Therefore, we used image analysis to distinguish E-Cadherin involved in cell-cell bonding from the “background” E-Cad expression.

In digital images, light intensity or brightness is represented in number (intensity count) ranging from 0 to 255 with 255 being the brightest. We set an arbitrary threshold value of E-Cadherin expression below which is considered as the background E-Cadherin and thus eliminated by image processing. Then what's left behind is relatively bright E-Cadherin expression which is mostly concentrated on the cell-cell interface. Intensity count over the entire image is added up and divided by the number of cells in the image obtained by counting the number of nuclei from nuclei staining image. This value is then a quantitative representation of E-Cadherin involved in cell-cell bonding per cell. Figure B.4 shows schematic of the image analysis described above. Although the selection of the threshold value is arbitrary, the half point value 128 appears to well eliminate background E-Cadherin.

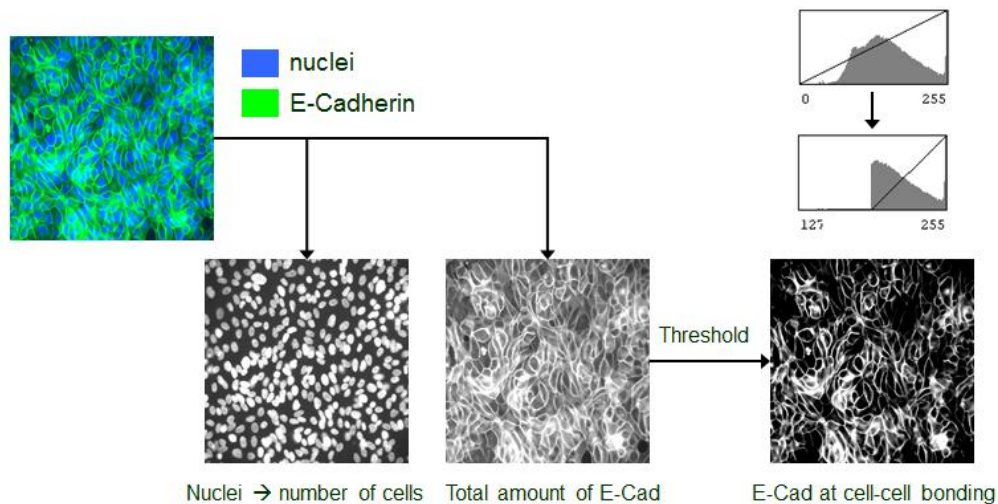


Figure B.4. Schematic of the image analysis

Figure B.5 shows the result of the analysis. “No stress” on the left is from the control experiment without stretching where there was no external mechanical stress applied to cells. “Stress” on the right is from the experiment where 33% compressive

strain was applied to cells at a rate of 4% strain per hour. Cell density (the number of cells per image) for “stress” case is almost as twice high as that for “no stress” case, which is qualitatively natural consequence of the squeeze. E-Cadherin per cell is the total intensity count per cell including background E-Cadherin expression. This value can be a reference value indicating the overall concentration level of E-Cadherin in cells in each experiment. E-Cadherin on cell boundary represents the concentrated E-Cadherin on the cell-cell interface, presumably involved in cell-cell bonding. When the threshold value of 128 is used, this value is about 45 times higher for stressed case than that of control experiment. This is significantly high contrast considering the small difference in reference values in each experiment. From this result, we can conclude that compressive stress enhances cell-cell bonding strength.

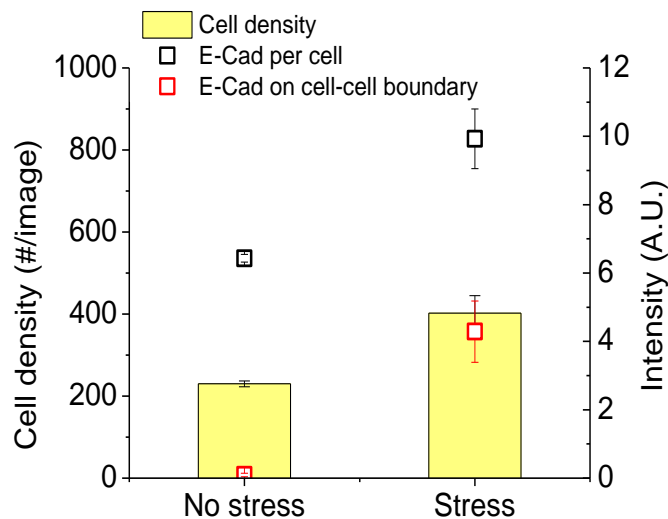


Figure B.5. Result showing significant increase (45 times) in E-Cadherin expression on cell-cell boundary after compressive mechanical stress.

B.5 FUTURE WORK

We have developed a device that can apply mechanical stress over large area of a cell layer in a controlled manner. Also the preliminary experiment demonstrated that compressive mechanical stress not only changes the shape of cells, but it enhances cell-cell bonding strength. To further improve the result, there are a few issues to be addressed.

First of all, one should be able to culture cells to a uniform monolayer which fully covers the elastic substrate without voids. In order for the cells to be squeezed effectively, cells have to proliferate enough to cover the entire surface of the elastic substrate. Otherwise, cells will most likely rearrange their position instead of being squeezed when compressed. Also, cells should be cultured as a single monolayer. Once cells stack on top of one another and form clusters, it becomes difficult to extract E-Cadherin expression on the cell-cell boundary from 2D image. Secondly, one should conduct more study to identify the proper threshold value to effectively differentiate binding E-Cadherin expression from the background E-Cadherin expression. Lastly, there is room to improve the stretching device. Current device is able to stretch the elastic film only in one direction. This induces compression of the film in the direction orthogonal to the stretching direction because of Poisson effect. A device that can biaxially stretch a film would result in better application of mechanical stress to cells. Material-wise, other elastic materials such as polyurethane can be tested. The elongation at break of PDMS is about 160% which limits the possible amplitude of applied mechanical strain. Transparent elastomers that can undergo higher strain without failure will be good

possible candidates. Surface treatment to improve cell adhesion other than poly-L-lysine can be tried such as oxygen plasma treatment or protein coating.

AUTHOR'S BIOGRAPHY

Howon Lee was born in 1978 in Seoul, Korea. He received his B.S. degree and M.S. degree from the Department of Mechanical and Aerospace Engineering at Seoul National University in Korea in 2004 and in 2006, respectively. He moved to the Department of Mechanical Science and Engineering at University of Illinois at Urbana-Champaign in 2006 for his doctoral study. In Jan 2007, he joined Professor Nicholas Fang's research group where he participated in various interdisciplinary research projects. His research interest during the course of doctoral program includes three-dimensional micro fabrication, polymer science, solid mechanics, and tissue engineering. His work was presented in 13 technical conferences and contributed to 4 peer-reviewed journal papers. He also served as a teaching assistance for two semesters, in one of which he was selected in "The Incomplete List of Teachers Ranked as Excellent by Their Students." Following the completion of his doctoral degree, he will join the Department of Mechanical Engineering at Massachusetts Institute of Technology as a postdoctoral scholar.